Effect of Topological Morphology on Optical Filtering Properties of Porous Silicon

by

Thomas Beniac

A THESIS SUBMITTED IN PARTIAL FULFILMENT OF
THE REQUIREMENTS FOR THE DEGREE OF

MASTER OF SCIENCE

in

The Faculty of Mathematics and Sciences

Department of Physics

BROCK UNIVERSITY

August 28, 2017

In presenting this thesis in partial fulfilment of the requirements for an advanced degree at the Brock University, I agree that the Library shall make it freely available for reference and study. I further agree that permission for extensive copying of this thesis for scholarly purposes may be granted by the head of my department or by his or her representatives. It is understood that copying or publication of this thesis for financial gain shall not be allowed without my written permission.

(Signature) _____

Department of Physics

Brock University
St. Catharines, Canada

Date _____

Abstract

Macroporous silicon samples of differing topological porous properties were manufactured by way of electrochemical etching. Different etching parameters (etching current, time, electrolyte concentration) were used on four different (in terms of crystal orientation and resistivity) types of samples in order to obtain a series of samples of differing pore topology.

It is known that macroporous silicon acts as a high-wavelength pass filter in the infrared regime. FTIR spectroscopy was performed on each of these samples in order to obtain an optical cutoff wavenumber for each sample. Furthermore, SEM analysis was performed in order to determine the number of pores per unit area on the surface as well as the percentage of the surface that was covered in pores for each sample. Furthermore, the average linear dimension per pore was determined using these values. Finally, the average pore-to-pore distance was also estimated on each sample. These four sets of measurements were performed in order to find a relationship between the optical and topological properties of macroporous silicon. It was found that there is a relationship between pore number density and cutoff; the cutoff wavenumber increases as the pore number density is increased. Additionally, a correlation between the pore spacing and the cutoff was also determined; the cutoff wavelength increases as the pore spacing increases. It was expected that there would be a correlation between the average linear dimension per scattering element as is seen in other types of scattering filters; however such a trend was only observed for one of the sample types. This suggests that the scattering mechanism by which porous

silicon filters operate differs between samples of significantly differing surface topology.

In addition to this, the temperature-dependence of the cutoff was investigated. Through low-temperature optical analysis using FTIR spectroscopy and liquid helium as a coolant, it was determined that the cutoff wavenumber exhibits no temperature-dependence below 100 K. For higher temperatures, the measurements performed were inconclusive. This was due to the thermal expansion at higher temperatures of the copper sample holder coupled with the inhomogeneity of the surface structure of each of the silicon filters.

Contents

List of Tables

List of Figures

Acknowledgements

I would like to acknowledge the members of my supervisory committee, Dr. M. Reedyk, Dr. F. Razavi, and Dr. D. Crandles for their guidance throughout my graduate research.

I would like to further thank Dr. Crandles for his assistance in operating the Bruker spectrometer.

Thanks also go to J. Dion and Z. Cronkwright for their assistance in performing resistivity measurements on my samples for the purposes of characterization.

Special thanks go to my direct supervisor Dr. M. Reedyk for all of her support, guidance, patience, and instruction throughout the entirety of my graduate work at Brock University.

Chapter 1

Introduction and Theory

Porous silicon was first manufactured in 1956 at Bell Laboratories by A. Uhlir. He was attempting to find a means by which silicon and germanium could be polished or shaped without using mechanical cutting techniques that can damage the sample [1]. One method that he used to try to accomplish this was a procedure called "electrochemical etching". This procedure will be described in greater detail later, but the basic essence of the method involves submerging the sample in an electrolytic solution contained within an anodization cell and running a current across it. Uhlir observed that electrochemically etching silicon did not provide the shiny surface that he was expecting, but instead caused the silicon to be covered in a dark deposit [1]. It was presumed that this deposit was a silicon dioxide product of the electrochemical reaction. Because this was not the result desired, this research was forgotten until the late 1980's [2]. It was at this time that it was determined that this "dark deposit" was not a deposit at all, but was instead small pores in the surface of the silicon.

It was not until the year 1990 that widespread research on the properties of porous silicon began in earnest [2]. It was at this time when experiments performed at the British Defence Research Agency revealed that meso- and microporous silicon exhibit strong photoluminescence [3]. However, this photoluminescence proved to be impossible to actually harness for any practical

application thus far [4]. Nevertheless, this newfound interest in porous silicon led to research into its other properties. For example, it was found that macroporous silicon acts as a high wavelength-pass filter in the infrared regime [5].

1.1 Electrochemical Etching of Silicon

In order to electrochemically etch a silicon wafer, the wafer must be placed in a solution containing fluoride ions (commonly referred to as the electrolyte) and then be anodically biased by way of an external current source [6]. Most commonly, the electrolyte is a solution of hydrofluoric acid and a solvent [7], although ammonium fluoride can be used in place of HF [6]. The solvent used is most often an organic solution such as ethanol, but water can be used in its place.

The process by which silicon can be etched is called *anodization*. In order to perform anodization, one requires what is called an anodization cell. An anodization cell is made up of five key components: an anode, a cathode, a power supply, the electrolyte, and a container in which the electrolyte can be housed [6]. When using such a cell to etch silicon, the silicon wafer itself acts as the anode. The cathode is generally made of platinum. This is done because platinum is strongly resistant to chemical attack and as such is less easily damaged by the electrolyte [6]. In addition, the container in which the electrolyte is housed must be made of a material that is resistant to the electrolyte. This is most often Teflon (polytetrafluoroethylene). In Figure 1.1, a schematic of a typical anodization cell is illustrated.

In order to cause pores to form on the surface of a silicon sample, a current must be applied across the anodization cell. If a current is not applied, it is known that silicon will not at all be dissolved by hydrofluoric acid [8]. The addition of current, however, causes an electrochemical reaction to occur as follows [2]:

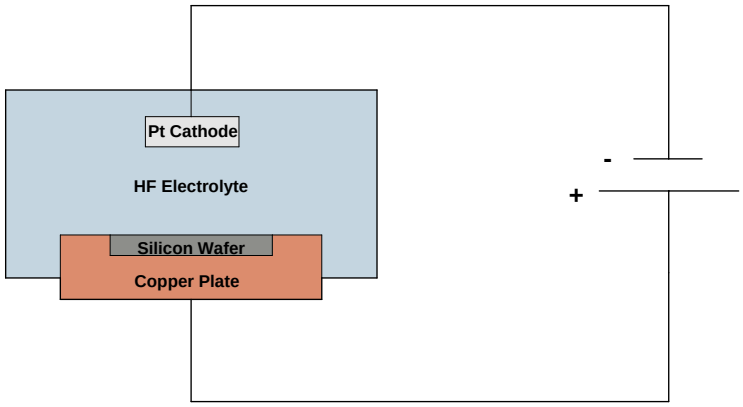

Figure 1.1: Schematic of a typical electrolytic cell. Contains a platinum cathode and a copper plate to facilitate the flow of current into the silicon wafer.

$$\mathrm{Si_{(s)}} + 6\,\mathrm{HF_{(aq)}} + 2\,\mathrm{h^+} \longrightarrow \mathrm{H_2SiF_{6(s)}} + \mathrm{H_{2(g)}} + 2\,\mathrm{H^+}$$

This reaction only occurs when the cell is anodically biased. Under cathodic bias, no reaction is observed [9]. When anodically biased, however, the silicon wafer undergoes a dissolution process. This causes the wafer's surface to become altered. Different etching conditions can cause drastically different morphologies to form on the wafer [9]. The most notable example of such a phenomenon occurs when the etching current density is increased to high values. Below a certain critical current, the dissolution causes small pores to form on the surface of the sample. Above this current, however, the wafer undergoes electropolishing and becomes mirror-like in appearance [10]. This occurs due to the fact that the electrolyte contains both fluoride (from the HF acid) and oxygen ions (from the water/solvent). When the dissolution process begins at the start of the electrochemical etching process, there are several different reactions that occur at the same time. Those of interest are three types of bond formation: Si-H, Si-O, and Si-F. It is known that Si-O bonds only form when there is a shortage of fluoride ions in comparison to the number of valence holes produced by the current [2]. When this happens, oxidized silicon atoms

appear on the wafer's surface too quickly to form bonds with the fluoride ions. As such, the Si-O bonds become dominant over any other, and a thin layer of silicon oxide builds on the surface of the wafer [10]. It is well-known that HF dissolves silicon oxide, and as such exposure to the electrolyte causes the oxide to be lifted away. This results in a wafer with a polished surface [2].

Below the critical current, however, electropolishing does not occur. This is because there is a shortage of valence holes in the sample and as such there are free fluoride ions that can attack the Si-O bonds before a thin oxide layer can form on the surface of the sample [2]. Instead, small pores are generated on the surface of the sample. This occurs due to the fact that a depletion region (i.e. a region which is depleted of charge carriers) appears at the junction between any semiconductor electrode and an electrolyte [11]. The reason for which a depletion region forms is due to the fact that there are more fluoride ions than holes, and as such the holes get completely used up. Because the depletion region is depleted of charge carriers, it prevents the dissolution reaction from occurring within this region. As such, certain regions are dissolved while others are not. This causes the pores to form [11]. However, the thickness of the depletion layer is smaller at points of larger curvature [12]. It is for this reason that, once a pore begins to form, the silicon dissolution occurs at the bottom tips of the pores. In addition to this, the current stops flowing through any region in which two depletion zones from adjacent pores meet one another [13]. This is what causes the separation between neighbouring pores. A schematic of this phenomenon is given in Figure 1.2.

The morphology of the pores formed by anodization seems to differ based on the initial etching conditions. In addition to this, it is observed that the etch rate is also highly dependent on these initial conditions. The conditions that affect the anodization process include: etching time, HF concentration in the electrolyte, anodization current, doping level and type, wafer orientation, and temperature [9]. In addition to this, the solvent used in the electrolyte can

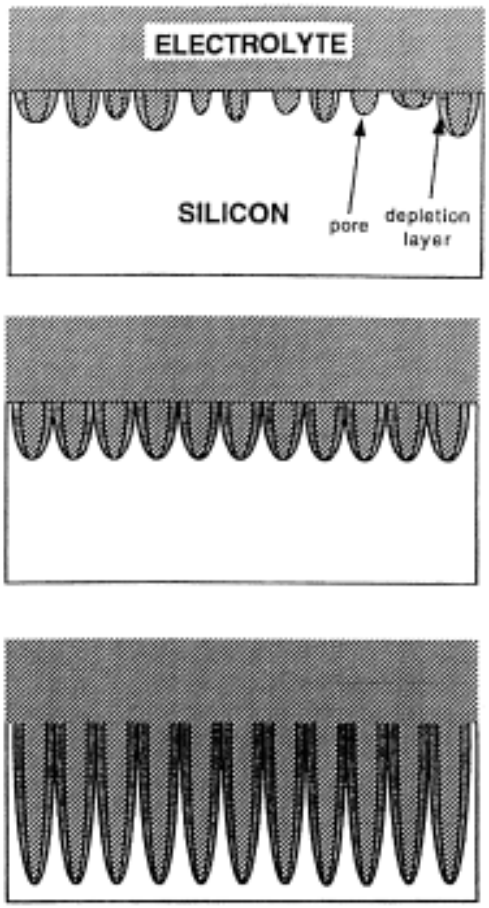

Figure 1.2: The mechanism of pore generation in silicon. The upper image shows the initial random formation of pores, the middle image shows the pores become ordered, and the third image shows that the pores preferentially grow in the direction of greatest curvature i.e. straight downward. Adapted from [13].

also affect the formation of pores [6].

The etching time is the parameter which determines the thickness of the porous layer. A longer etching time causes the porous layer to become thicker. This is because a longer period of time increases, naturally, the amount of time over which the reaction can occur [14]. This in turn causes more silicon to be dissolved. Since the pores form preferentially in the direction of the pore tips, it is obvious that an increased amount of silicon dissolution would occur here and thus increase the depth of the pores. It is observed that this effect is much more important for lightly doped wafers than it is for those which are heavily doped [15].

The concentration of the hydrofluoric acid in the electrolyte is what controls

the size of the pores that form on the surface. It has been observed that the pore diameter is decreased as the concentration of HF in the electrolyte is increased [16]. Additionally, the porosity of the porous layer is also decreased with increasing HF concentration [17].

The anodization current is the parameter that controls the thickness of the depletion zone. With an increased current, the depletion zone becomes thicker. This allows for the pores to become larger in diameter. It is observed that an increase in current density causes an increase in pore diameter. There is, however, a limiting current density beyond which the pore diameter stops increasing significantly [18].

The wafer crystal orientation also affects the geometry of the pores formed. The two different wafer orientations that are relevant to the content of this thesis are (1 0 0) and (1 1 1). This notation refers to the vector direction to which the surface of the wafer is perpendicular. For example, a wafer labelled with a (1 0 0) orientation will have its surface such that is orthogonal to the [1 0 0] direction with respect to the crystal basis of silicon. Since it is (1 0 0) and (1 1 1) silicon which are relevant, it will only be these two which are discussed. Generally, it is observed that pores preferentially form in the [1 0 0] direction during etching [19]. This is what is observed for (1 0 0) wafers. For (1 1 1) wafers, however, it is observed that pores occasionally also form in the [1 1 3] direction. This means that the pores in (1 1 1) wafers propagate in a direction that is not perpendicular to the wafer's surface [19]. An illustration of the pore formation for both types of sample is given in Figure 1.3.

The solvent used in the electrolyte has a significant effect on the result of electrochemically etching silicon. If an alcohol (commonly methanol or ethanol) is used as the solvent, it will cause chemical leaching of the porous layer. With long etching times and high alcohol content, it is observed that this causes the porous layer to form in a gradient; the resulting porosity will be higher toward the surface of the wafer than it is toward the silicon substrate. If deionized

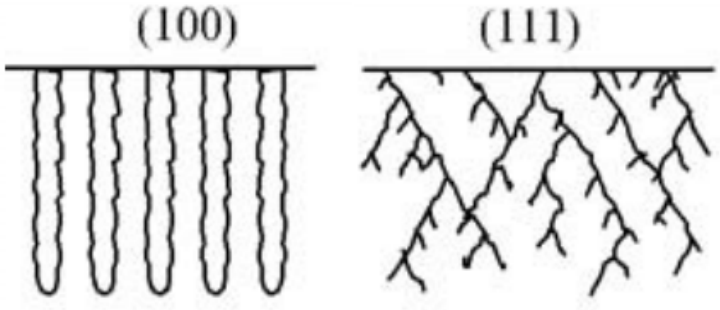

Figure 1.3: Image illustrating the direction of pore propagation for (1 0 0) samples (left) and (1 1 1) samples (right). Note the branching [1 0 0] and [1 1 3] pores on the (1 1 1) sample. These are angled at 34° and 61° with respect to the surface respectively. Reprinted from [20]

water is used as the solvent, however, this chemical leaching does not occur and the porous layer will be non-uniform in thickness. In addition to this, the porous layer often becomes very rough at the surface [6].

The doping type and level may very well have the most significant effect on pore formation. Both p- and n-type doped silicon can be electrochemically etched, although extra components (namely a light source that gives the ability to illuminate the back side of the wafer) must be added to the cell in order to etch n-type silicon. Four different types of doping are typically discussed when describing the effect of doping on the formation of porous silicon: moderately doped p-type silicon, heavily doped silicon of either type, non-heavily doped n-type silicon, and lowly doped p-type silicon. Each of these has a range of pore diameters that can be formed through etching [20]. These are summarized in Table 1.1.

Table 1.1: Summary of pore diameters formed by electrochemical etching for different doping types.

Doping Type (carrier concentration)	Typical Pore Diameter
Moderate p-type (10^{15} - 10^{18})	1-10 nm
Heavily doped ($> 10^{19}$)	10-100 nm
Non-Heavily Doped n-type ($< 10^{18}$)	10 nm - 10 μm
Lowly doped p-type ($< 10^{15}$)	varying, see below

For lowly doped p-type silicon, the pore diameters formed can be on wildly

different orders of magnitude. They can be as small as on the nanometre scale and as large as several microns. Unlike as it is for non-heavily doped p-type silicon, this is not a continuous range of possible pore diameters. It is instead divided into two possible diameter scales: those on the nanometre scale and those on the micron scale [20]. The diameter scale is highly dependent on the other etching parameters [20]. As such, use of lowly doped p-type silicon is beneficial if one wants to manufacture many samples of differing pore sizes while keeping the doping type constant.

It should also be noted that the formation of pores is not necessarily uniform over the entire surface of the sample; there may be a small difference in pore size or distribution between different locations on the sample's surface. This often comes from the type of electrochemical cell used. The type of cell described earlier is useful because it is made from relatively simple equipment and provides reasonable uniformity of pores across the sample during etching, however more complicated designs can be used to ensure higher uniformity [15]. In addition to this, samples of resistivity higher than a few ohm-millimetres can also require a conductive material to be applied to the backside of the wafer in order to ensure good electrical contact. If this is not done, the uniformity of pores may suffer (or etching may not take place at all) [15].

1.2 Pore Formation Mechanism Models

Though the chemistry behind electrochemically dissolving silicon is understood reasonably well, the mechanism by which the silicon is selectively dissolved from certain areas and not from other areas such that a porous structure is formed is not. There have, however, been some models presented on the subject.

1.2.1 Quantum Confinement Model

As described earlier, it is known that it is due to a depletion region that ordered pores form in a silicon wafer under anodic etching conditions such that the current is below the critical current. The mechanism by which this depletion region forms in such a way that walls can form between the pores (and as such, pores can even exist) is not well-understood. In 1991, Lehmann and Goesele proposed a model based on the principle of quantum confinement to explain this [8].

Lehmann and Goesele determined through experiment that the pore walls for the samples that they etched were in the range of 2.1-2.7 nm in thickness [8]. In addition to this, there is no space-charge region that can be formed in p-type silicon (due to the anodic bias of the cell) that would explain the formation of the depletion layer which causes pore growth. Because of this, it was proposed that the reason for which the depletion region forms is due to quantum confinement of charge carriers that occurs because the pore walls are very small [8].

The quantum confinement causes the effective band-gap energy to increase, which in turn causes the energy required for holes or electrons to enter the thin pore wall between dissolution regions to increase. Lehmann and Goesele approximated this energy barrier to take the form of a two-dimensional potential well, otherwise known as a quantum wire [8]. From this they proposed the following equation for the energy barrier ΔE:

$$\Delta E = \frac{h^2}{4m^* q^2} \tag{1.1}$$

where h is Planck's constant, m^* is the effective charge carrier mass, and q is diameter of the quantum wire (i.e. the thickness of the pore wall).

From this, Lehmann and Goesele estimated that there is an energy barrier of approximately 0.5 eV in the pore walls. As such, it is likely that walls will

become depleted of charge carriers and consequently the depletion region that prevents the electrochemical dissolution of the pore walls can be formed [8].

1.2.2 Surface Curvature Model

Also in 1991, Zhang proposed a model for pore formation that suggests that it is due to the curvature of the pores themselves that the depletion region is thinner at the bottom than it is at the sides [21].

Zhang proposed that the means by which charge carriers reach the surface of the silicon wafer is through interface tunneling [21]. If the electric potential across the wafer is large enough, a large electric field is induced and the depletion region becomes smaller [21]. This allows for electrons to more easily tunnel across the depletion region and to reach the wafer's surface, thus allowing silicon dissolution to occur. This tunneling effect is much stronger for larger electric fields. From this, Zhang posits that based on Poisson's Equation for a spherical surface (i.e. an approximation for the surface on the bottom of the pore) [21] that:

$$\frac{1}{r^2}\frac{d}{dr}[r^2\mathcal{E}(r)] = \frac{\sigma(r)}{\epsilon} \tag{1.2}$$

where r is radial position, ϵ is permittivity, $\mathcal{E}(r)$ is the electric field, and $\sigma(r)$ is the charge density in the depletion region. In order to better illustrate the geometric setup of this situation, a schematic of the pore tip used in this model is given in Figure 1.4. In this schematic, x_d is the width of the depletion region, r_0 is the radius of curvature of the pore, and x is simply labelling of the horizontal axis.

After applying the proper boundary conditions and the depletion approximation (a commonly used approximation that assumes that the space-charge region is completely devoid of charge carriers; it is necessary in order to solve Poisson's equation for a semiconductor [22]), Zhang showed that the electric field can be given by the following equation [21]:

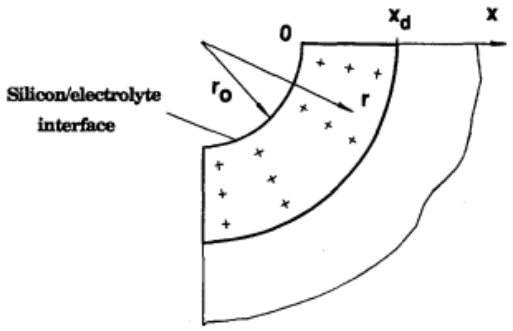

Figure 1.4: Schamatic of the pore tip used in Zhang's model. The labels on the image are defined in the main body of the thesis. Reprinted from [21].

$$\mathcal{E}(x + r_0) = \frac{qN_B}{3\epsilon}\Big[- (x + r_0) + \frac{(r_0 + x_d)^3}{(x + r_0)^2}\Big] \tag{1.3}$$

where q is the carrier charge and N_B is the donor density.

From this equation, it can be shown that the electric field is larger for smaller radii of curvature [21]. Since the radius of curvature is much smaller at the pore tip rather than at the sides, it is obvious that under this model that silicon dissolution will occur much more quickly at the pore tips due to the larger field.

A weakness of this model is that it does not well describe the formation of pores in p-type silicon, as the space-charge region required for this model to be accurate only exists in n-type silicon [8].

1.2.3 Current Burst Model

In 2000, Foell, Carstensen et al. proposed yet one more theory regarding the mechanism by which porous silicon forms. This model was based on the idea that different phenomena that occur when silicon is placed under anodic etching conditions should be related. Namely, Foell based what he called the "Current Burst Model (CBM)" on the idea that observed current and voltage oscillations of the electrolytic system under high but constant applied potential should in some way be related to the formation of pores on the surface [24].

Previous to the advent of this model, it was generally assumed that the

current density across the silicon wafer was well-defined over space and time and could only change smoothly between points [7]. However, this cannot hold true. This is because of four distinct intermediary processes that occur during silicon dissolution [7]:

- Direct Dissolution. This is a process where valence holes in the silicon are consumed and injected electrons account for the lost charge. It requires only one hole and as such is the most efficient of these processes. This reaction is given by:

$$\mathrm{Si} + \mathrm{xh}^{+} - \mathrm{ye}^{-} \longrightarrow \mathrm{Si}^{4+}$$

  where x and y are the number of holes and electrons respectively. To balance the equation, it is clear that y = 4 - x and that y and x must be greater than 0.

- Oxidation. This process always requires four holes and as such is not nearly as efficient as direct dissolution.

$$\mathrm{Si} + 4\,\mathrm{h}^{+} + 2\,\mathrm{O}^{2-} \longrightarrow \mathrm{SiO_2}$$

- Oxide Dissolution. This is a chemical process that limits the total current that the silicon can process, as the oxidation rate cannot be larger than the dissolution rate.

$$\mathrm{SiO_2} + 4\,\mathrm{F} \longrightarrow \mathrm{SiF_4} + \mathrm{O_2}$$

- Hydrogen Coverage. This causes whatever is on the surface of the silicon (given in the chemical reaction as X) to be replaced by hydrogen given enough time. The reaction is given by:

$$\mathrm{SiX} + \mathrm{H} \longrightarrow \mathrm{SiH} + \mathrm{X}$$

During the hydrogen coverage reaction, there is a hydrogen passivation process that occurs concurrently [24]. This means that some interface states in the band-gap of the silicon get removed. In this model, this process plays a major role in pore formation which will be discussed later.

It was observed that the number of carriers flowing through the external circuit for each silicon atom dissolved was about 2.7 [7]. Because of this, Foell argued that both the oxidation and the direct dissolution processes must occur simultaneously. This must be the case because if only one of these two processes were to occur at a given time, this carrier number would need to be an integer as per the chemical equations above. In addition to this, oxide dissolution must also be occurring in order to limit the current used. Furthermore, the hydrogen coverage reaction must also be occurring on account of the fact that current cannot be running through the pore walls as per Lehmann's quantum confinement theory [7]. Since these reactions cannot possibly be taking place at the same location and time, it is clear that current density cannot be homogeneous in space and time [7].

In order to remedy this, Foell developed his Current Burst Model. It relies on three major propositions [7]:

1. As described above, current flow cannot be homogeneous in space and time. At a given point in space and time, a charge transfer process has a certain probability of occurring on the surface of the sample. This probability is governed by the "state" of the surface at a given time and location. The charge transfer process is what Foell calls a "current burst" [7].

2. The current burst is made up of the chemical processes outlined above. These must occur in a logical sequence for a given surface location: first is direct dissolution, second is the oxidation reaction, third is the oxide dissolution, and fourth is the hydrogen coverage (and consequently hydrogen passivation) process. The final process only occurs if a second

current burst has not yet begun [7].

3. Current bursts can interact in space and time. This means that the probability of a current burst occurring is not only dependent on the surface state but also what has previously occurred at a given location [7].

The condition dictating pore formation is whether or not hydrogen passivation has yet occurred. Because some of the interface states are removed from the silicon band-gap when passivation occurs (the reason for which the process occurs is not well-understood [23]), it makes it far less likely for a current burst to occur due to a lack of valence holes (i.e. the direct dissolution cannot start). Because of this, it is more likely for a current burst to occur when an area is not yet passivated [24]. Because of this, current bursts tend to occur in locations where the oxidation dissolution process has not yet completed. This causes the current bursts to cluster, which in turn forms pores (i.e. many reactions are occurring in locations that are adjacent to one another) [24].

In addition to this, the CBM also explains why the pores form preferentially in the [1 0 0] direction. The reason for this is that the hydrogen passivation process occurs much more slowly in the [1 0 0] direction than it does in other directions [25]. Because the passivation process has a large effect on the probability of a current burst occurring, it follows that slower hydrogen passivation processes increase the likelihood of a current burst taking place. As such, current bursts are more likely to occur in the [1 0 0] direction and, consequently, pores are also more likely to form in this direction [25].

1.3 Infrared Optical Filters

It has been proposed that porous silicon can be used as an optical filter in the infrared regime. Originally, it was suggested that mesoporous silicon could be used as a bandpass filter if a sample made from multiple mesoporous silicon layers of different porosity were used. Such a filter would operate similarly

to a standard interference filter; it has been observed that layers of different porosities have differing refractive indices [26]. Because of this, constructive or destructive interference occurs in the light waves reflecting from adjacent layers [27]. This causes certain wavelengths to be passed through the multilayer sample and others to be filtered out.

1.3.1 Long-Wave Pass Filters

More relevant to the subject of this thesis, however, is the fact that it has been observed that macroporous silicon can be used as a long-wave pass filter [26]. Long-wave pass filters are those that pass all wavelengths that are greater than a given wavelength (called the cuton) and filters out shorter wavelengths. Commonly, multilayer interference filters are used to accomplish this; however it has been found that it is difficult to use an interference filter to pass long-wavelengths only in the mid- to far- infrared regime [27]. As such, filters for this region are often scattering-type filters.

Scattering-type filters are made up of two layers: a layer of particles (often diamond, but could be some other robust transparent material) that are the "scatterers" and a substrate layer that is transparent in the infrared range [27]. The transmissive properties are based on both the size and distribution of the scattering particles, the index of refraction of the scattering material, and the thickness of the scattering layer [28]. At wavelengths that are small in comparison to the diameter of the scattering particles, scattering occurs by way of the simple optical processes of refraction, reflection, and diffraction [28]. These wavelengths are then scattered away and do not pass through the filter. Since the substrate layer is transparent in the infrared regime, longer wavelengths are able to pass through without being scattered away. The distribution of particle sizes governs the sharpness of the cutoff i.e. the range of wavelengths over which the infrared transmission falls to zero. The index of refraction of the layer and the thickness of the scattering layer also have a comparatively

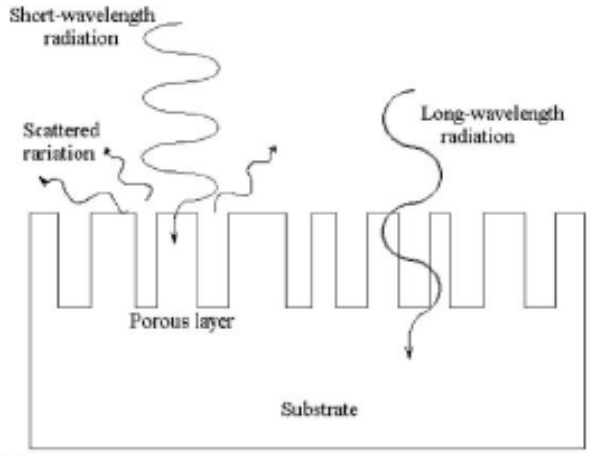

Figure 1.5: Brief schematic of a long-wave pass macroporous silicon filter. Reprinted from [4]

smaller effect on the cutoff wavelength [28].

It is expected that macroporous silicon filters operate in a similar manner as illustrated schematically in Figure 1.5. Instead of having a layer of fine particles as the scattering layer, it is replaced by the porous layer. Since the pores on the surface of a flat macroporous silicon sample are of a random distribution and of (generally) a small range of pore diameters that are on a scale of hundreds or thousands of nanometres, it stands to reason that a macroporous silicon sample should produce a filter that cuts off in the infrared regime [27]. This prediction has been confirmed experimentally; it has also been shown that adjusting the etching parameters used to create a macroporous silicon sample can change the cutoff wavelength and sharpness [4].

1.3.2 Effect of Oxide on Optical Transmission

It has been observed that porous silicon can develop an oxide layer on its surface. Silicon is known to form a native oxide layer of several angstroms when exposed to dry air for an extended period of time [29]. Because porous silicon has a high surface area to volume ratio, it is more susceptible to oxidation than a bulk sample. This oxide formation can have an effect on the transmissive properties of a macroporous silicon filter.

One such effect is that a significant oxide layer on the surface of a sample can cause a not insignificant blue-shift in the transmission spectrum of a filter [30]. This is problematic because the exact cutoff of the filter cannot be known unless it is initially measured without oxide and the oxide can be removed for later use. Fortunately, a 90-second dip in a low-concentration hydrofluoric acid solution can be used to dissolve most of the silicon dioxide layer that forms on the surface of the filter [31]. It is necessary to perform this dip before use, as a native oxide layer of thickness 2 μm forms on silicon after 15 hours of exposure to dry air [32].

In addition to this, there are several absorption lines that appear on oxidized porous silicon samples [33]. These can be useful in determining whether or not a sample has undergone any significant oxidation. Before discussing these lines, however, it should be cautioned that there are some other absorption lines that can appear which are independent of oxidation.

Because silicon is tetravalent, it can bond with hydrogen molecules that are a product of the etching process [33]. It can bond in the form of SiH, SiH_2, or SiH_3. As shown in Figure 1.6(a), there are three absorption bands that can be experimentally observed in non-oxidized silicon. One is at 2090-2150 cm^{-1}, another is at approximately 920 cm^{-1}, and the last is at 600-700 cm^{-1} [33]. Through the comparison of the optical spectra of the silicon hydrides, amorphous hydrogenated silicon, and silicon treated with hydrofluoric acid, it is possible to assign the absorption bands to various vibrations relating to the aforementioned silicon hydrides [33]. The first absorption band (i.e. that from 2090-2150 cm^{-1}) can be assigned to the molecular stretching of any of the silicon hydrides, the second can assigned to the scissors bending of SiH_2, and the last can be assigned to SiH_2 wagging and SiH bending in Si_3SiH [33]. It is important to note these absorption bands do not at all come from the oxidation of the surface, and as such are not indicative of any silicon oxides formed on the surface of a porous silicon sample.

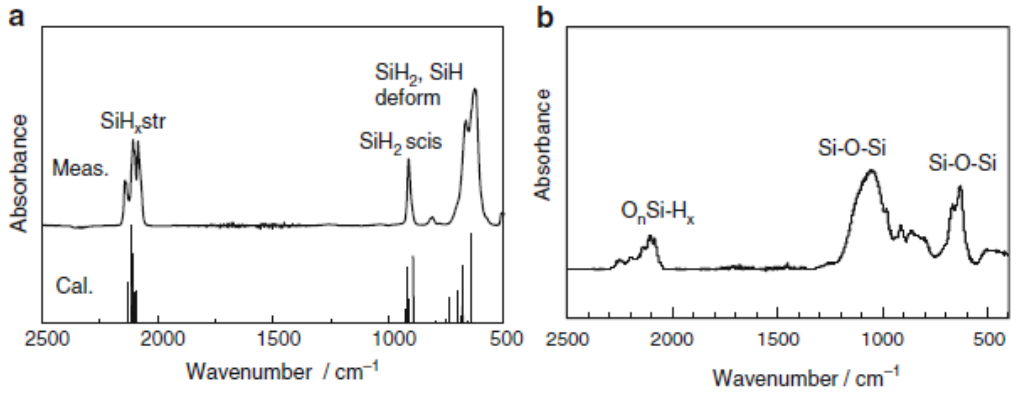

Figure 1.6: FTIR absorbence data for (a) a non-oxidized porous silicon sample and (b) an oxidized porous silicon sample. Notice the difference in absorption peaks between the two spectra. Reprinted from [33].

There are three types of absorption bands that come from the oxidation of porous silicon [33]. The first of these covers a wide range around 3600 cm^{-1} and is attributed to the stretching of O−H bonds, the second is a set of absorptions that are slightly higher than the silicon hydride stretching absorptions that occur due to the stretching of O_nSi-H_{4-n} (n=1,2,3) bonds, and the third is a set of strong absorptions that occur at or below 1200 cm^{-1} that are due to the stretching of Si−O−Si bonds (at the high end) or the deformation of O_nSiH_x [33]. These lower wavenumber absorption bands are shown in Figure 1.6(b). Using this information it is possible to determine whether or not a sample has experienced significant oxidation.

1.4 Applications, Advantages and Other Considerations of Infrared Filters

Optical filters in the infrared range are used in a variety of scientific, astronomical, and atmospheric instruments. As mentioned earlier, most current options for infrared filtering are based on multilayers. Unfortunately, there are relatively few materials (thallium bromoiodide, ZnSe, CdTe are examples) that are transparent in this regime, and those that are may be environmentally unsta-

ble. This causes these multilayer filters to fade (i.e. lose opacity) or delaminate when exposed to humidity. Silicon, however, is much more environmentally stable and as such will not suffer from such problems [34].

In addition to this, multilayer filters also suffer from their intrinsic design. Multilayer filters are, as their name suggests, made up of layers of differing materials with varying refractive indices. Different materials, however, also have variation in their coefficients of thermal expansion. As such, they expand or contract at different rates when exposed to extreme temperatures [34]. Since many research and astronomical applications require very low temperatures, this poses a challenge. Operators of such instruments are forced to control the temperature of their filters in order to ensure that they do not undergo any kind of structural failure due to one layer expanding more quickly than another. Porous silicon filters, however, are made up of only one material. This ensures that the entire filter will expand or contract by the same amount even at extreme temperatures [34].

Furthermore, multilayer filters are also limited by their lack of physical strength. This is due to the fact that multilayer filters are relatively thick; a single pair of layers can be tens of microns thick [34]. Because of this, multilayer filters are limited as to how large they can be in diameter without becoming brittle. Commonly, this limit is around 1 inch [34]. Porous silicon filters, however, have been manufactured to sizes of up 8 inches [34]. Clearly, this can be advantageous for use in larger instruments.

Multilayer filters also take a significant amount of time to manufacture. Deposition of a single layer can take up to 12 hours [34]. Porous silicon filters, however, are much simpler and far less time-consuming to create.

In addition to multilayer filters, scattering-type filters are also used in the infrared range. Though these are not fraught with as many temperature-based disadvantages, they are still inferior to silicon-based filters. This is due to the poor mechanical properties of scattering-type filters. This is because the scat-

tering layer can be easily washed or blown off of the surface of the filter [26]. This causes such filters to be unable to withstand large pressure differentials. Because of this, any vacuum pumping of such a filter would need to be performed very slowly. Conversely, porous silicon does not have a separate scattering layer. It instead has a "built-in" scattering layer that cannot be easily blown or washed away. It is clear that these filters would be more robust than their more traditional counterparts. They can also easily withstand rapid vacuum pumping without experiencing any structural failure [26].

There are, however, some shortcomings to using porous silicon as a filter. One of these comes from the previously mentioned oxide formation on the filter's surface. As discussed, an oxide layer on the surface of the sample causes both absorption lines and a blue-shift of its optical transmission region. There has however, been a proposed solution to this problem. It was found that sputtering a layer of amorphous silicon on the surface of the filter slowed the oxidation process considerably [26]. However, silicon filters sputtered in such a way still did eventually degrade. Because of this, it is necessary to both carefully store and periodically clean porous silicon filters.

In addition to this, it has been found that filters made from highly-doped silicon can fail to filter light properly. This occurs due to the high concentration of free carriers in the substrate layer [27]. These free carriers have a high absorption rate (due to the high concentration). This causes the substrate to become opaque to infrared light. As such, all of the light is filtered out as opposed to simply having the undesired region filtered away [27]. The solution to this problem was to use an electrical current strike on the sample at the end of the etching process. This separates the porous layer from the substrate, thus removing the problem of free carrier absorption [26]. Unfortunately, the porous layer on its own is far too brittle for any practical applications.

The proposed solution to this obstacle is to chemically fuse this porous layer to another silicon substrate layer of lower free carrier concentration. This new

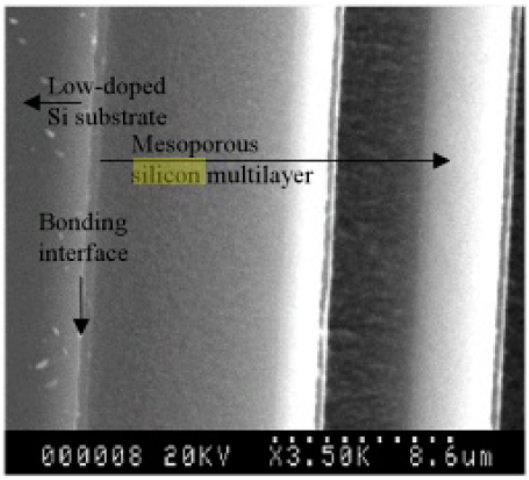

Figure 1.7: SEM Image of a Multilayer Mesoporous Silicon Filter which makes use of a porous layer fused to a lowly-doped substrate. Reprinted from [26]

substrate layer is not opaque to infrared light, which in turn means that it will filter light correctly [30]. An image of a mesoporous multilayer silicon filter that makes use of this technique is given in Figure 1.7.

1.5 Project Objectives

The goal of this thesis work is to determine a relationship between the optical cutoff values and the surface topology of an etched silicon filter. The number density of the pores on the surface of a given filter, the percentage of the area which is covered by pores, and the average linear dimension of the pores will be related to the optical cutoff in order to define any possible relationship. Any relationship established would be a step toward having the ability to reliably create porous silicon filters with any desired cutoff value.

In addition to this, low temperature optical measurements will be performed in order to determine what, if any, effect temperature has on the optical properties of these filters. This is important because the main advantage associated with porous silicon filters is in their ability to withstand large variations in temperature; any effects caused by temperature would need to be noted in advance of using such filters in any research or practical application.

Chapter 2

Methods and Instruments

2.1 Outline of Methodology

The primary goal of this work was to explore relationships between the optical cutoff and the morphological geometry of various macroporous silicon filters. Specifically, the number of pores per μm^2 was related to the optical cutoff. This value will hereafter be referred to as the "pore number density". In addition to this, the percentage of the surface of each sample that was covered by pores, as well as the average linear pore dimension, was estimated.

A total of 34 samples were manufactured for the purpose of these experiments. These were all electrochemically etched using methods similar to those outlined in Chapter 1. To determine the optical cutoff of each sample, Fourier Transform Infrared Spectroscopy was used. To determine the pore dimension, density and the percentage of the surface which was covered by pores, Scanning Electron Microscopy was used.

A secondary goal of this work was to attempt to determine a relationship between temperature of the filter and optical cutoff. This endeavour was only partially successful; there proved to be some complications with regards to achieving this goal.

2.2 Electrochemical Etching Cell

As outlined in Chapter 1, an electrochemical cell is required to etch silicon. The cell used in this procedure is made up of five primary parts: a power supply, an electrolytic solution, a well in which this solution can be housed, a lid, and a base.

The power supply used in this experiment was a Keithley Model 220 programmable source. It has a variable current which can be adjusted to any value from 2 nA to 100 mA [35]. It also has an adjustable voltage compliance that can range as high as 105 V. As such, all current values used for etching in this project were well within these ranges.

The electrolytic solution was made up of a mixture of 100 % ethanol for use as the solvent and 48-50 % hydrofluoric acid. Each electrolytic mixture was created such that it had a total volume of 250 mL. The ratio between acid and solvent was varied for different samples; however it was never lower than 1:9 and never exceeded 1:1. The exact ratio used for each sample will be outlined in Section 2.3.

The electrolytic well used in these experiments was a white Teflon container with an open top and a small (approximately 3/4 of an inch in diameter) hole in the bottom. The well had a volume slightly greater than 250 mL so that it could comfortably house the electrolyte solution. The well was made from Teflon because Teflon is known to be resistant to hydrofluoric acid [13]. As such, there is no danger of the electrolyte damaging the well. A set of eight clearance holes for screws are located on a lip around the lower exterior edge of the well. On the underside of the well's bottom surface, there is an o-ring flange around the small hole. A photograph of the well is given in Figure 2.1.

The lid of the sample was made of hard PVC plastic and contained two important components: a platinum wire electrode and a propeller controlled by a motor. The platinum wire operated as the cathode of the electrolytic cell. It was situated such that it was run through a very small hole in the top of

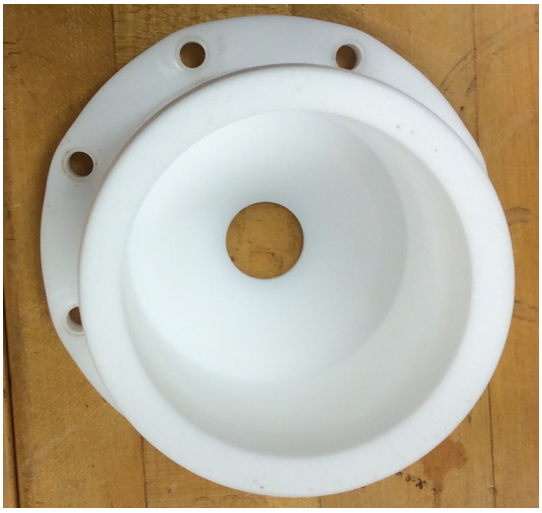

Figure 2.1: Photograph of the electrolytic well used in the etching process.

the lid. The reason for this was two-fold: it allowed for the wire to be partially inside the cell and partially outside of it and it created a small hole through which hydrogen gas created during the dissolution process could escape without being built up in the cell. The wire needed to be partially inside the cell in order for it to actually contact the electrolyte so etching can take place and it needed to be partially outside so that it could be connected to the current source. Additionally, the platinum wire was twisted such that it formed a loop. This was done because it has been shown that shaping the electrode such that it is approximately the same size and shape as the wafer helps to improve the uniformity of the pore topology after etching [6].

The purpose of the motorized propeller was to stir the electrolyte. This was done in order to prevent the buildup of hydrogen gas bubbles on the surface of the silicon sample that could stop the etching process. The propeller was determined to be consistently running at approximately 45 rpm. A photograph of the lid is given in Figure 2.2.

The base of the cell is a flat copper plate that is of the same diameter as the bottom lip of the well. It has eight threaded screw holes around the edge corresponding to the eight similar holes in the well. This is so that the base can be secured to the Teflon well. In addition to this, it also has a small hole

(a) Cell Lid: Side View (b) Cell Lid: Top View

Figure 2.2: Photographs of the lid of the electrochemical cell.

on the rounded edge into which a banana plug of a wire can be inserted. A photograph of the plate is given in Figure 2.3.

The procedure for carrying out the etching of the sample is relatively simple. First, the silicon wafer (after being dipped in HF in order to remove any native oxide) to be etched is placed on top of the copper plate such that, when the well is attached to the base, the wafer is exposed to the electrolyte through the small hole in the well's base. The wafer fits snugly into the indent around the hole on the underside of the well to allow for the o-ring to seal against the wafer and prevent the electrolyte from leaking out of the cell.

It should be noted that for wafers of sufficiently high resistivity it is necessary to add a thin layer of indium-gallium eutectic[1] between the wafer and the copper plate. This layer ensures that there is good electronic contact between the wafer and the plate.

Once the wafer is centered on the plate, the well should be secured to the base with the series of screws. Once this is done, the electrolyte can be mixed.

To create the electrolyte, the appropriate amount of ethanol is poured into

[1] a mixture of substances that melts at a single temperature that is lower than the melting points of its separate constituents

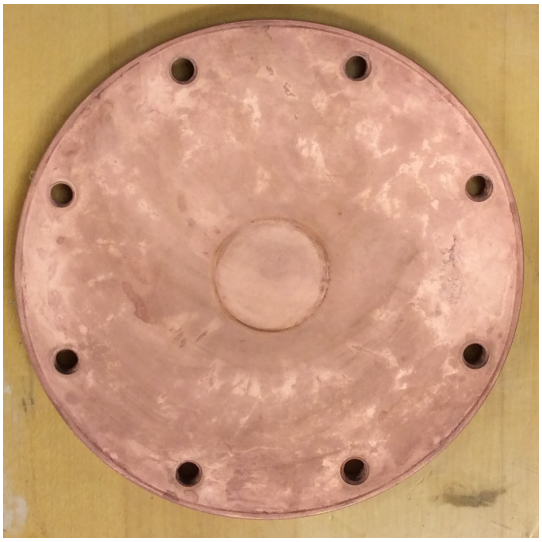

Figure 2.3: Photograph of the base of the electrochemical cell.

the cell to which is added the required amount of hydrofluoric acid. When working with hydrofluoric acid, it should be ensured that appropriate protective equipment is used in order to prevent serious injury or death.

Once the electrolyte is mixed and poured into the cell, the lid can be placed on to the top of the well. There is an o-ring on the inside of the lid to seal the cell shut. Once the lid is secured, the motor can be switched on and the propeller will begin to spin. At this point, the cell is almost entirely assembled. A photograph of the totally assembled cell is given in Figure 2.4.

Once the cell is assembled, the current source can be connected. The positive terminal of the source is connected to the copper plate. Since the copper plate is conductive, it allows the current to flow through and up to the silicon wafer. This allows the wafer to become the anode as required. The negative terminal is attached to the platinum wire at the top of the cell. This allows the wire to become the cathode of the cell.

Once connected, the current source can be set to the appropriate current value. This value is varied between different samples. In addition to this, the voltage tolerance of the source is adjusted to its maximum level. This is done to ensure that the etching procedure is not voltage-limited. Much like acid concentration and etching current, the amount of time used for etching was

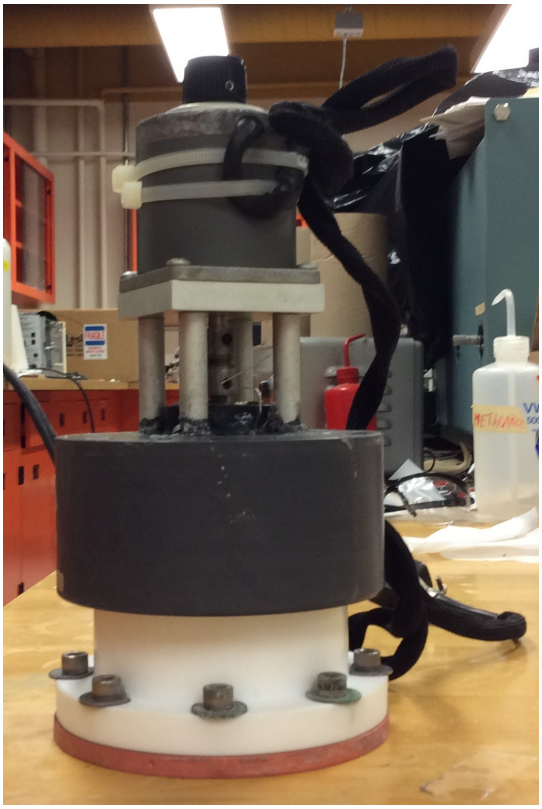

Figure 2.4: Photograph of the entirely assembled electrochemical cell.

Table 2.1: Intrinsic properties of the sample types as they came from the manufacturer.

Type	Thickness (μm)	Resistivity (Ω· cm)	Orientation	Dopant
A	500	20	(1 0 0)	Boron
B	280	8	(1 1 1)	Boron
C	300	>20	(1 0 0)	None
D	300	5	(1 0 0)	Boron

varied between different samples.

2.3 Samples

There were four different types of base samples used in this project. Three of them (referred to in this thesis as types A, B, and C) were from the supplier "Virginia Semiconductor" and the other (referred to as type D) was from the "Institute of Electronic Materials Technology". All samples were double-side polished prior to being shipped by the company and had a diameter of 1 inch. The specifics of each sample type are given in Table 2.1.

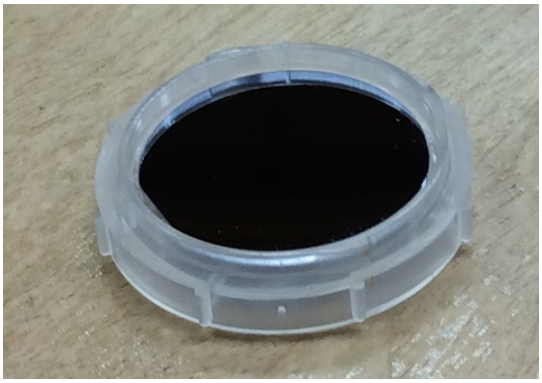

Figure 2.5: Photograph of an unetched wafer.

Types A, B, and D had their resistivity values measured by way of Van Der Pauw's method [36]. An indium-gallium eutectic was used to obtain contacts conductive enough to measure the resistivity of the wafer. Type C was labeled as undoped and had a very high resistivity, which could not be measured, and as such the value on the supplier's packaging was quoted in the table above. Before etching, all four types of wafer were similar in appearance. A sample image of a wafer is given in Figure 2.5.

Samples of all four types were etched using different etching conditions. The etching conditions that were varied included etching current, etching time, and HF concentration in the electrolyte. This was done in an attempt to obtain many samples of differing optical cutoff and pore geometry. The etching conditions used for each of the samples are given in Table 2.2.

Samples 1 and 17 have etching parameters that are identical to those of Samples 3 and 21 respectively. During these etches, a voltmeter that stores voltage data as a function of time was used in order to determine whether or not the voltage across the electrochemical cell was varying in time. It was found that this voltage did indeed stay constant over the course of the etching procedure.

After etching, it was found that some samples had developed a relatively thick black deposit of unknown origin on their surfaces. It was determined that a weak solution of hydrochloric acid placed in an ultrasonic bath was able to

Table 2.2: Etching Parameters for all 34 samples used for this project.

Sample No.	Type	Etching Current (mA)	HF:Ethanol Ratio	Time (h)
1	A	25	1:4	3
2	A	10	1:4	3
3	A	25	1:4	3
4	A	25	1:4	8
5	A	25	1:1	3
6	A	50	1:4	3
7	A	25	1:4	23
8	A	10	2:3	3
9	B	10	1:9	1
10	B	10	3:7	4.5
11	B	25	1:4	3
12	B	10	3:7	0.5
13	B	5	1:4	3
14	B	10	1:4	4.5
15	B	10	1:4	1
16	B	10	3:7	3
17	B	10	1:4	3
18	B	25	1:4	8
19	B	25	1:4	3
20	B	25	1:4	1
21	B	10	1:4	3
22	B	25	1:4	4.5
23	B	10	1:9	4.5
24	B	50	1:4	3
25	B	10	1:9	3
26	B	10	3:7	1
27	B	25	1:4	0.5
28	C	10	1:9	20
29	C	10	1:9	5
30	C	10	1:4	5
31	C	25	1:9	5
32	D	25	1:4	3
33	D	10	1:4	3
34	D	10	1:9	24

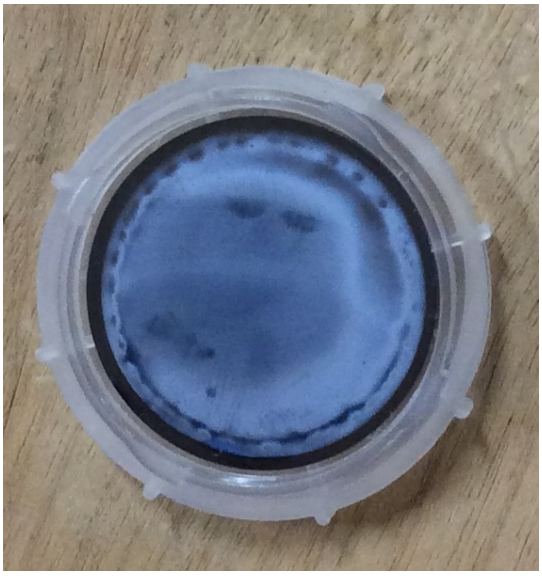

Figure 2.6: Photograph of an etched wafer.

remove the deposit. Because silicon is inert to acids under normal conditions, there is no danger of damaging the sample through this process [37]. The duration of time required to remove the film was variable; it could be as little as five minutes or as long as several hours. An image of an etched, clean wafer is given in Figure 2.6.

2.4 Scanning Electron Microscopy

2.4.1 Principles of Operation

A scanning electron microscope (SEM) is a device that is used to generate high-resolution images in order to observe fine structures that otherwise would be difficult to see under a standard light microscope.

The SEM operates by scanning the sample with a beam of electrons in a rectangular (raster) pattern. It does this by way of an electron gun. The electron gun is typically fitted with a tungsten filament, however, more expensive materials such as lanthanum hexaboride can be used to achieve higher filament lifetime and slightly higher resolution of image [38]. These materials have high melting points, and as such can be heated without being damaged to the point

at which they can release electrons. It is necessary, however, to ensure that the electron gun is kept under vacuum while in operation. Failure to do so can cause a pair of problems: a) the lifetime of the filament can be shortened if exposed to high pressure and b) the electron beam can have its path altered by gas particles. If the path of the beam is altered, it will not scan the sample properly and the image will be distorted [39]. Because the gun and the beam need to be kept under vacuum, both the sample and electron gun are enclosed in a long column.

In order for the electron beam to be released, the filament must first be heated. After this, a voltage that is typically between 1 and 30 keV is applied in the column in order to accelerate the electrons in the beam [38]. Once the electron beam is ejected from the gun, it passes through a series of condenser lenses that are located in the column. These condenser lenses are not lenses in the traditional optical sense, but rather are magnetic lenses made from wire coils. The purpose of these lenses is to collimate and focus the electron beam [40]. The beam then passes through a set of deflection coils. These coils provide the variable magnetic field required to cause the beam to scan the sample. These coils also control the magnification of the image [38]. After this, the beam passes through a final aperture that aids in focusing the beam. A basic schematic of an SEM is provided in Figure 2.7.

In order to generate the image, the electron beam must interact with the atoms on the sample's surface. This interaction causes three different phenomena:

1. Secondary Electron Emission: Secondary electrons are released from the surface of a sample when the primary electrons (i.e. those from the incoming beam) strike the surface with sufficient energy and inelastically scatter from the surface. This inelastic scattering causes surface electrons to be released from the sample [38].

2. Backscattering of the Electron Beam: Backscattered electrons consist

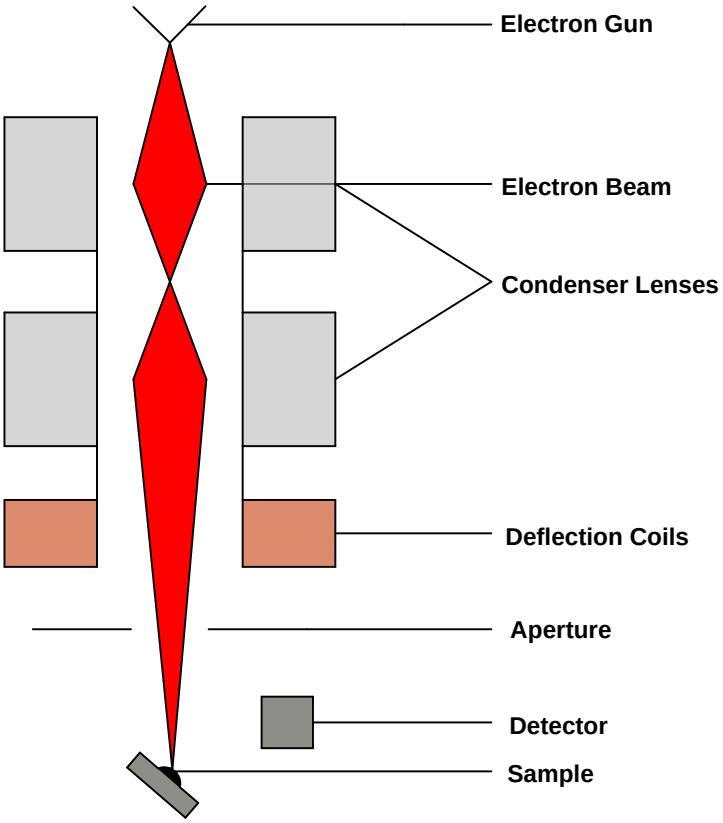

Figure 2.7: Basic Schematic of an SEM.

of those that are primary electrons that have been elastically scattered from the surface of the sample. Due to the fact that heavy (in terms of atomic number) elements backscatter more strongly than light elements, the detection of backscattered electrons can be useful in differentiating areas of samples consisting of different materials [38].

3. Emission of X-Ray Radiation: X-rays can be released due to the interaction of the electron beam with the surface. These x-rays can be used to determine the chemical composition of a sample [38].

For the purposes of this work, it is only the detection of secondary electrons that is of interest. This is due to the fact that it is only the porous geometry which is important rather than any kind of chemical composition of the samples.

In order to generate an image based on the emission of secondary electrons, it is first necessary to have a means of detecting these electrons. To do this, an Everhart-Thornley detector is used [38]. A schematic of such a detector is

given in Figure 2.8.

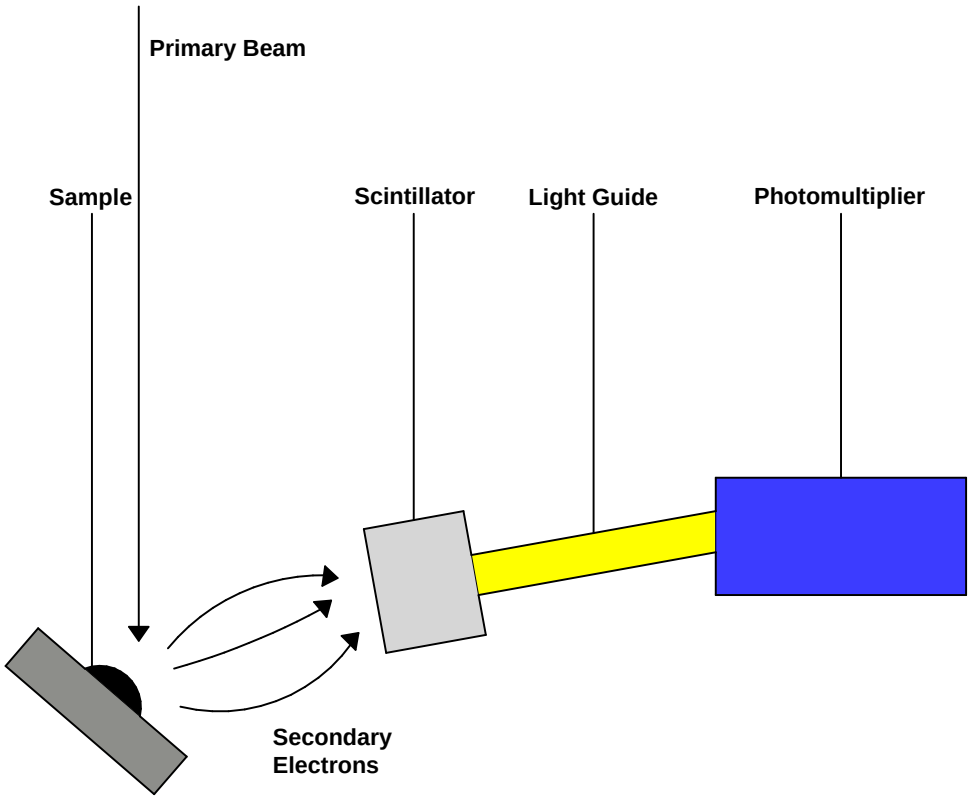

Figure 2.8: Basic Schematic of an Everhart-Thornley Detector.

The detector consists of two major parts: a scintillator and a photomultiplier. The scintillator is struck by the secondary electrons and emits light. This light travels through a light pipe and into a photomultiplier. The photomultiplier converts the light into electron pulses which are then amplified. These signals are then used to generate the image digitally [38]. Because the energy of secondary electrons is typically very low, they must be accelerated by applying a voltage to an aluminum film that is placed over the scintillator. Failure to do this would result in the scintillator not receiving enough energy to be excited by the secondary electrons, which would in turn result in no image being generated [38]. Due to this process, it is obvious that the image generated through SEM is not actually an optical image, but simply an artificially generated digital representation of the sample. Backscattered electrons are scattered at a different angle than that at which the secondary electrons are emitted. As

such, the detector can be strategically placed within the SEM so as to ensure it only detects secondary electrons [38].

Another factor to consider during SEM imaging is the fact that samples must be sufficiently conductive across their surface in order for the imaging method to work properly. If the surface is not conductive enough, the scattered electrons will leave the surface at a slower rate than the beam electrons are hitting it [38]. This causes a buildup of electrons on the surface of the sample; an effect known as charging. This charging effect causes the surface of the sample to become negatively charged, which in turn repels the primary electrons from their regular path. This causes the image to become distorted [38].

To overcome this problem, a thin layer of a heavy conductive metal (often gold, silver, or platinum) can be used to coat the surface [38]. This layer is normally of a thickness of a few nanometres. Since the surface layer is now conductive, there will be no buildup of charge on the surface and imaging can be done normally. Since the layer is thin, the topography of the sample will be maintained [38]. The disadvantage to doing this is that it permanently alters the sample; it can be difficult or impossible to remove the conductive layer.

As briefly mentioned earlier, it is the deflection coils that control the magnification of the image. The means by which they do this is simple; the coils simply scan the beam over a smaller area [38]. Since the display remains the same size, it stands to reason that scanning over a smaller area will cause this smaller area to fill the entire display. This effectively magnifies the image. Unlike magnification in a light microscope, this process involves no use of lenses.

2.4.2 Method

The SEM used for analyzing the morphological properties of the porous silicon filters was an Amray Model 1600 Scanning Electron Microscope (Figure 2.9).

Before imaging was begun, the sample needed to be mounted on an aluminum holder (see Figure 2.10 for a photograph) which had a flat face of the

Figure 2.9: Photograph of the Amray Model 1600 SEM. At left is the microscope column and pumping station and at right is the control panel.

same diameter as the silicon sample. This was done through the use of a silver conductive paint that was applied to the non-etched side of the sample. The reason for this is two-fold: it acts as an adhesive to hold the sample in place and is conductive enough to allow the primary electrons to flow away from the surface of the sample in order to prevent charging.

The C-type samples are of very high resistivity. As such, they are not conductive enough to image without risking charging. To counteract this, the four C-type samples were coated with a thin silver film before imaging. The use of a thin film ensures that the surface of the sample is conductive without altering its topology. A film too thick has the potential to completely obscure any fine features of the surface, whereas the thin film should follow any irregularities present.

After the holder was mounted within the sample chamber of the SEM, three images were gathered for each sample. These images were gathered at three

Figure 2.10: Photograph of the aluminum SEM sample holder.

very different locations on the sample: one in the center, one toward the bottom edge, and one toward the top edge. Each sample had all three images taken in the same session in order to prevent the same area from being imaged twice. This was done in an attempt to obtain a general representation of the porous structure of the entire sample rather than just at a single position.

2.4.3 Polaron SC500 Sputter Coater

As mentioned previously, the C-type samples needed to be coated with a thin metallic film in order to be properly imaged. This was done via a method known as sputter deposition.

Sputter deposition involves the ejection of atoms from a source referred to as a "target". This target and the sample to be coated both must be placed into a chamber which can be evacuated to a pressure of approximately 0.1-0.05 Torr [41]. Once the chamber is evacuated, an inert gas (typically argon) is then leaked into the chamber. This gas is then exposed to an ionizing potential which in turn causes the gas atoms to form a highly energized plasma [42]. The plasma then erodes the target material, causing the target atoms to be ejected. These atoms collide with any non-ionized gas particles left in the chamber

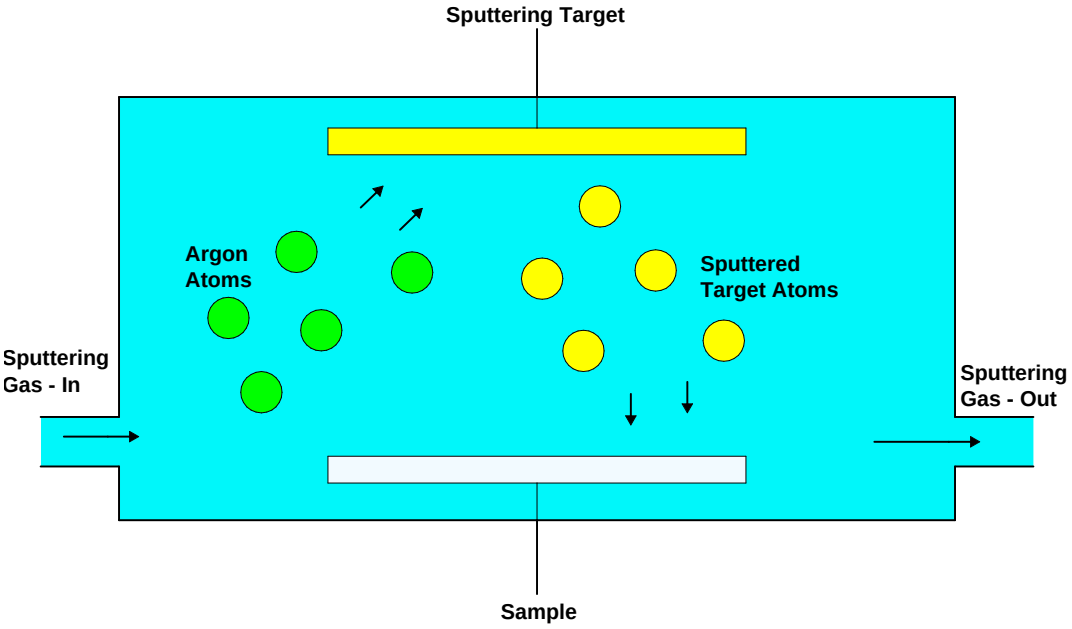

Figure 2.11: Basic Schematic of a Sputter Coater.

and with each other. They then deposit onto the sample in a multidirectional fashion [42]. This allows for a uniform and complete coverage of the sample. A schematic is provided in Figure 2.11.

The Polaron SC500 Sputter Coater operates almost entirely automatically. The automated sputtering process is typical of a sputter coater. Initially, a burst of argon gas is used to flush out any contamination from the chamber. After this, the chamber is evacuated to approximately 0.1 Torr. The chamber is then purged with argon gas until the pressure stabilizes again around 0.1 Torr. The ionization current is then applied and coating begins. Once the coating time expires, the chamber is vented to atmospheric pressure and the sample can be removed [41]. For coating the C-type samples, a sputtering time of 150 seconds was used along with an ionization current of 10 mA. A photograph of the sputter coater is given in Figure 2.12.

Figure 2.12: Photograph of the SC500 Sputter Coater.

2.5 Fourier Transform Infrared Spectroscopy

The optical spectra presented in this project were measured using a method called Fourier Transform Infrared (FTIR) spectroscopy.

2.5.1 Principles of Operation

The primary component of an FTIR spectrometer is a Michelson interferometer. This device has the purpose of splitting a beam of radiation into two parts and then recombining them. This recombination occurs after a path difference has been introduced to one of the beams [43]. A Michelson interferometer is made up of three key parts: a fixed mirror, a movable mirror, and a beamsplitter. A schematic of a simple Michelson interferometer is given in Figure 2.13.

Due to the path difference mentioned above, recombining the beams causes interference. This interference causes the intensity of the beam to be different than that of the initial beam. As such, a detector can be used to measure the

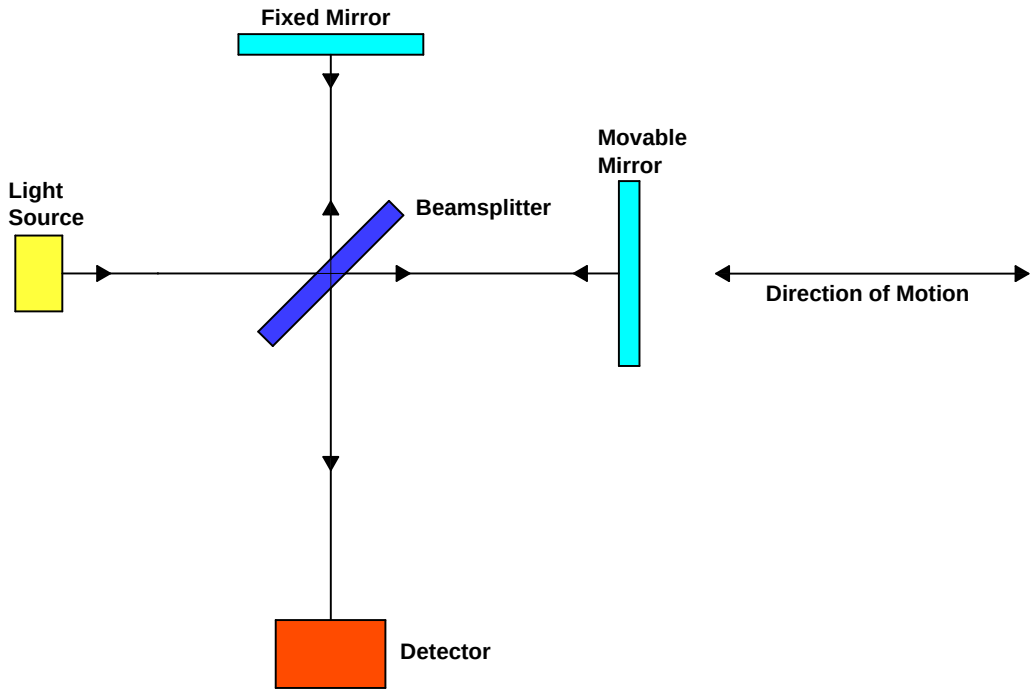

Figure 2.13: Basic Schematic of a Michelson Interferometer.

intensity as a function of path difference [43].

In order to make this function useful, it is necessary to generate an interferogram. The most basic illustration as to how an interferogram is generated is to first assume that an infinitely narrow perfectly collimated beam of monochromatic light of wavelength λ_0 travels into the interferometer. Second, assume that the beamsplitter is perfect; it splits the incoming beam of light perfectly such that 50 percent of the beam is directed toward the fixed mirror and the other 50 percent is directed toward the movable mirror [43]. Furthermore, it needs to be assumed that the beamsplitter is infinitely thin. This is to ensure that no optical path is generated within the beamsplitter itself. The optical path difference (the path difference between the two beams both travelling from the beamsplitter to the appropriate mirror and back) can then be given to be $\delta = 2(M_2 - M_1)$, where M_2 is the distance between the beamsplitter and the movable mirror and M_1 is the distance between the beamsplitter and the fixed

mirror [43].

When M_1 and M_2 are equal, $\delta = 0$. This condition is referred to as the point of zero path difference (ZPD). At ZPD, the two beams are perfectly in phase with one another and as such undergo constructive interference [43]. This ensures that all of the light that passes into the beam splitter also passes into the detector and as such gives maximum intensity.

If the movable mirror is moved to a distance from the point of ZPD to $\lambda_0/4$, the optical path difference is then equal to half of one wavelength and the two beams will be completely out of phase when they recombine at the beamsplitter [43]. Because of this, the beams will destructively interfere completely and zero intensity will reach the detector.

If the movable mirror is displaced to a point of $\lambda_0/2$ from the point of ZPD, then $\delta = \lambda_0$. This again causes the beams to be in phase at the beamsplitter, constructive interference occurs and maximum intensity reaches the detector [43].

In practice, it is seen that if the mirror is moved at constant velocity that the intensity at the detector will vary sinusoidally [43]. The intensity as a function of optical path difference can then be written as [43]:

$$I'(\delta) = 0.5I(\tilde{v_0})(1 + \cos(2\pi\tilde{v_0}\delta)) \tag{2.1}$$

where $\tilde{v_0}$ is the wavenumber $1/\lambda_0$ and $I(\tilde{v_0})$ is the intensity of the source.

For the purposes of spectroscopy, it is only the harmonic (sinusoidal) part of the $I'(\delta)$ function that is of interest. This function is what is referred to as the interferogram. Therefore, the interferogram equation for the idealized case outlined here is given by [43]:

$$I'(\delta) = 0.5I(\tilde{v_0})\cos(2\pi\tilde{v_0}\delta) \tag{2.2}$$

In reality, there are three major issues which cause this equation to be

incorrect. One of these is due to the fact that beamsplitters are generally not ideal (i.e. do not split the beam evenly), one is that infrared detectors do not respond uniformly at all wavenumbers, and the last is that the amplifier used with the detector does not respond uniformly across all wavenumbers [43]. Because of this, two correction terms need to be added to Equation 2.2. $H(\tilde{v_0})$ is the correction term for beamsplitter efficiency and $G(\tilde{v_0})$ is the correction term for the response of the amplifier and beamsplitter. This gives an interferogram equation of [43]:

$$S(\delta) = 0.5H(\tilde{v_0})G(\tilde{v_0})I(\tilde{v_0})\cos(2\pi\tilde{v_0}\delta) \tag{2.3}$$

Commonly, this equation is simplified to:

$$S(\delta) = B(\tilde{v_0})\cos(2\pi\tilde{v_0}\delta) \tag{2.4}$$

where $B(\tilde{v_0})$ is the intensity as altered by the characteristics of the interferometer.

This equation is the cosine Fourier transform of $B(\tilde{v_0})$. Because of this, calculating the Fourier transform of $S(\delta)$ will allow for a spectrum of the intensity at the detector as a function of wavenumber to be determined [43].

In the idealized case laid out above, it was assumed that the light source was monochromatic and coherent. In practice, however, light sources used for FTIR are not monochromatic. If a light source of multiple wavelengths is used, then the resulting interferogram is the sum of the interferograms given by every wavelength emitted [43]. Because of this, the interferogram is incredibly complicated and a computer must be used to carry out the Fourier transform.

For a source that emits a continuous range of wavelengths, it can be shown that the interferogram can be given by [43]:

$$S(\delta) = \int_{-\infty}^{\infty} B(\tilde{v})\cos(2\pi\tilde{v}\delta)d\tilde{v} \tag{2.5}$$

and its resulting Fourier transform can be given by (since $S(\delta)$ is an even function):

$$B(\tilde{v}) = 2\int_0^\infty S(\delta)\cos(2\pi\tilde{v}\delta)d\delta \tag{2.6}$$

From this equation, it appears that the interferogram could be measured with infinitely small resolution [43]. However, the only means by which one could do this is by allowing the optical path difference to vary between 0 and ∞. Since this is very clearly impossible, it is obvious that the resolution of the measurement must be finite. The resolution is determined by the maximum value of δ [43]. Specifically, the resolution is given by the relationship $\delta_{max} = \frac{1}{\Delta\nu}$, where $\Delta\nu$ is the resolution [43].

The type of measurements that were performed for this project were transmission measurements. These measurements are relatively simple. First, a spectrum must be taken for the Michelson interferometer operating under baseline conditions. This spectrum is referred to as the "background power spectrum". Once this is done, a power spectrum will be taken with the sample to be analyzed located between the recombined beam and the detector (i.e. so the beam passes through the sample). This should give a spectrum that is different in comparison to the background; the medium through which the recombined beam passes will alter the intensity of the beam at a given wavenumber. Once these two power spectra are gathered, the sample spectrum is divided by the background spectrum. This allows for the intensity of light for a given wavenumber that is passed through the sample to be given as a percentage of the initial beam.

Though beamsplitters have been mentioned as critical to the operation of a Michelson interferometer, they have not yet in this work been discussed in much detail. The purpose of a beamsplitter is, as outlined, to split the beam from the light source into two beams of equal intensity. In order for this to occur, a perfect beamsplitter should be 50 percent transmissive and 50 per-

cent reflective. In practice, most beamsplitters are not perfect (especially over all wavenumbers). For different spectral ranges, different materials are used to make beamsplitters. There were three types of beamsplitters used in this project.

One of the beamsplitters used in this project was a potassium bromide (KBr) beamsplitter. These beamsplitters use KBr as a substrate material. Because this material is highly transmissive in the infrared range, this substrate material serves to filter out any non-infrared light before it reaches a germanium coating that is wedged between two pieces of the substrate material. This coating acts as a partially silvered mirror which is partially transmissive and partially reflective [44]. It is this coating which splits the beam. These beamsplitters are effective in the range from 400-6500 wavenumbers.

A second beamsplitter that is used in this project was a cesium iodide (CsI) beamsplitter. These are similar to KBr beamsplitters; the main differences include a different operating range (200-4000 wavenumbers) and the fact that they are softer and more hygroscopic than KBr beamsplitters [44].

The third beamsplitter used Mylar (of thickness 6 microns) as a substrate material. It again used a germanium coating to split the beam. This beamsplitter, however, had a much lower useful range: it operates between 50 and 700 wavenumbers. This is because the Mylar is transmissive in this range rather than the higher ranges given by the salt-based substrates [45].

The detectors used to perform infrared spectroscopy fall into two main categories: thermal detectors and quantum detectors. Both were used during experimental work in this project.

Thermal detectors operate by sensing changing temperature of an absorbent material. This temperature change can be detected via thermocouples, a resistance change of a conductor, or by the movement of a diaphragm due to an expanding gas [43]. These types of detectors can be used for mid-infrared measurements. However, they are “slow” detectors; they have a response time

that is on the order of several milliseconds [43]. As such, use of these detectors requires the scanning speed of the movable mirror to be quite slow. The only type of thermal detector that is "fast" enough to practically used for FTIR spectroscopy is a pyroelectric bolometer.

Pyroelectric detectors use ferroelectric materials to sense temperature change. These materials experience a large electrical polarization below their Curie point [43]. If the temperature is changed, the polarization changes. If, however, the temperature increases to above the Curie temperature, the response of the detector becomes zero. As such, it is important to ensure that these detectors remain cold enough to operate without losing the signal.

Quantum detectors, however, operate by measuring the effects of the interaction between infrared radiation and the electrons in a semiconductor [43]. This interaction causes the electrons to be excited from the valence band to the conduction band of the semiconductor. Because the energy of the infrared photons is inversely proportional to its wavelength, the number of electrons excited can be measured as a function of wavelength. These electrons can be measured as a current, and the measurement of the current gives the response of the detector for a given wavelength [43]. Unlike thermal detectors, quantum detectors have a much faster response time, and as such gathering spectra from such detectors can be done at relatively high speed.

A drawback of these detectors come from the fact that, in the mid-infrared range, the photons have low energy. Since electrons can be excited by random thermal agitation of the detector, it is possible that this agitation could produce a signal that is comparable in size to the signal generated by the photons [43]. This can introduce a significant amount of noise to the output of the detector. To remedy this, quantum detectors must be cooled to low temperatures [43]. This reduces the probability that thermal agitation can occur, which in turn reduces electronic noise in the output.

2.5.2 Bomem Model MB102

There were two spectrometers that were used to measure the cutoff values for the porous silicon samples. The one that was used for the majority of the samples was the Bomem Model MB102 FTIR spectrometer. This spectrometer includes a standard Michelson interferometer that is enclosed within the device such that it is not easily accessible. This is because the interferometer is permanently aligned; it is used for measurements with only one type of light source and one beamsplitter. The beamsplitter used in this device is a CsI beamsplitter. The light source used is a Globar. A Globar is a silicon carbide rod which is heated to 1650 degrees Celsius and acts as a blackbody. It produces light in the mid-infrared regime.

The detector used by the Bomem is a mercury cadmium telluride (MCT) detector. This is a quantum detector that must be cooled with liquid nitrogen before use in order to return a signal with low electronic noise.

Though the Michelson interferometer is inaccessible, there is some setup that needs to be carried out in order to perform measurements. A photograph of the setup is given in Figure 2.14 and a schematic is given in Figure 2.15.

The sample holder is placed in between the detector and the recombined beam (labelled as the "light source" in Figure 2.15) in a holder screwed into a kinematic mount. On this mount, there are several locations into which the holder can be screwed. For the purposes of measuring the optical cutoff, the holder was screwed into the location that was nearest to the beam source. This was because it was in this position where the sample was overfilled[2] by the recombined beam. This overfilling ensured that the spectrum that was gathered was an average over the entire sample rather than the spectrum of one specific location.

To gather the data, a computer software called Win-Bomem Easy was used. This Windows-based software allows for the easy control of experiment pa-

[2] "Overfilling" refers to using a beam which has a larger diameter than the sample.

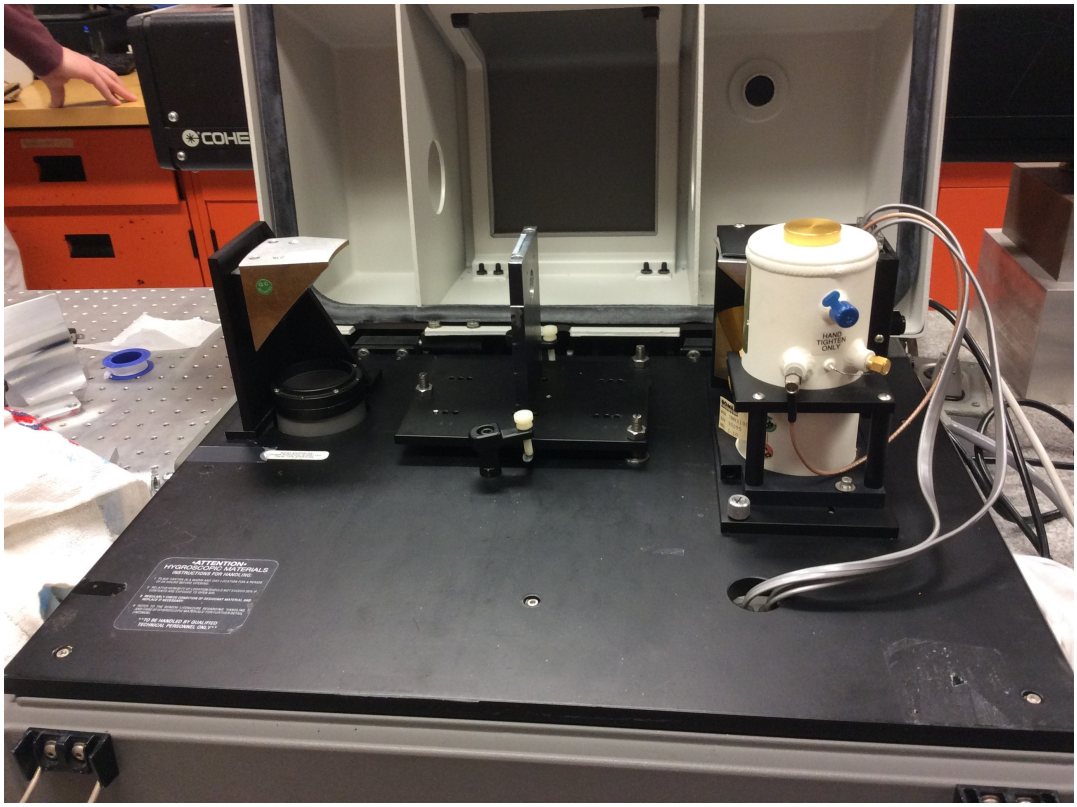

Figure 2.14: Photograph of the Bomem Model MB102 FTIR Spectrometer.

rameters. The important parameter for this experiment is the spectrometer resolution. The resolution was set to 4 cm^{-1}. This was the highest resolution that could be used without seeing any optical fringing effects in the spectrum. To determine the cutoff, a smooth-as-possible curve was desired. As such, it was necessary to avoid any fringing effects. In addition to this, the software can be used to gather spectra as both a raw interferogram or as a percent transmission spectrum. The number of scans of the interferometer for a single experiment can also be set via the software; this allows for a spectrum to be made up of an average of many scans. The range of scanning can also be set: the scan range for these experiments was set to 0-5000 cm^{-1}.

Before a transmission spectrum can be gathered, a background spectrum must be obtained. This was done by recording a spectrum with the holder empty (i.e. allowing the beam to pass through an empty hole). After this was done, the holder was then filled with a sample. A sample spectrum was then gathered. All spectra obtained were averaged over 64 complete scans of

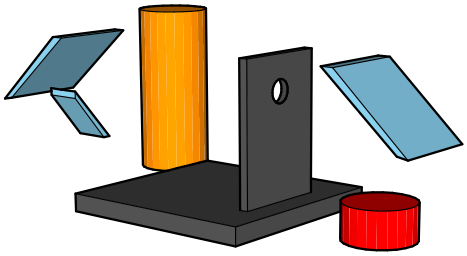

(a) Bomem: Diagonal View

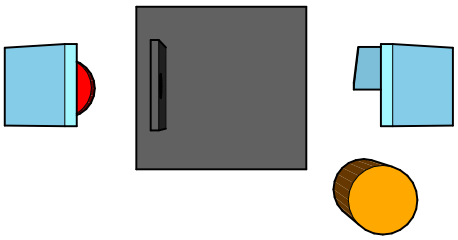

(b) Bomem: Top View

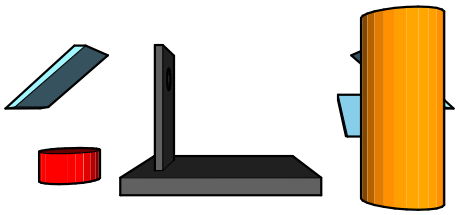

(c) Bomem: Side View

Figure 2.15: Experimental Setup for the Bomem. The mirrors are blue, the sample holder is grey, the detector + cooling flask is orange, and the light source is red.

the interferometer. This was done for all but one of the samples. The one sample that was not analyzed with this spectrometer was determined to have a cutoff much lower than 400 wavenumbers, and as such a different beamsplitter would be required to obtain any useful data. For each sample, five spectra were obtained. This was done in order to have multiple measurements for the cutoff wavenumber, thus reducing the odds of obtaining erroneous results. The sample spectrum is automatically divided by the background spectrum by the software, and as such the optical transmission as a function of wavenumber is given in the output.

A second experiment that was performed using this apparatus was to determine whether or not the cutoff wavelength varied over different locations on the sample. In order to do this, a mask was used to ensure that only a small spot on the sample was exposed to the incoming beam. A photograph of the mask is given in Figure 2.16. This was done for three different spots on the sample. Obtaining the spectra was performed similarly to as outlined above; the only difference is that the mask needed to be secured to the side of the holder facing the beam during the background scan. Three spectra were gathered for each spot, again each averaged over 64 scans. After each spot was analyzed, a marker was used to circle the area which had been analyzed. The reason for this was two-fold; it ensured that there was no overlap between the spots being measured and it allowed for later topological analysis using the SEM. A photograph of the sample complete with marked analysis locations is given in Figure 2.17.

2.5.3 Bruker IFS 66v/S

The second spectrometer used to perform optical analysis was a Bruker IFS 66v/S FTIR spectrometer. Conceptually, this device operates on the same principles as the Bomem; it is a Michelson FTIR interferometer. However, unlike the Bomem, there is considerable freedom in setting the device up for use.

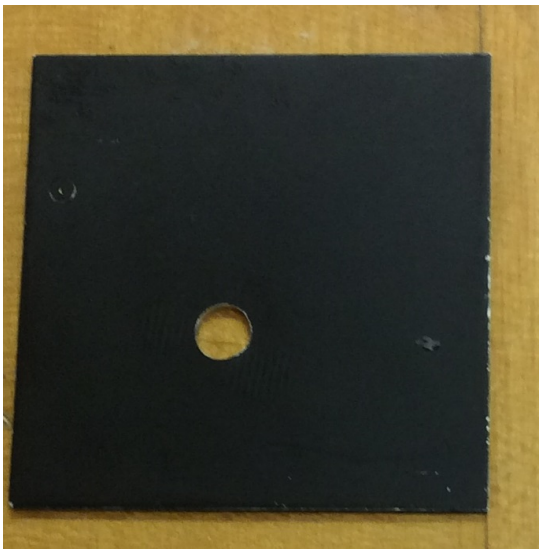

Figure 2.16: Photograph of the mask used to obtain location-dependence of the cutoff over one sample.

Figure 2.17: Photograph of Sample 10 complete with markings designating the three spots for which different spectra were gathered.

The Bruker is not permanently aligned, can be fitted with different detectors, can be fitted with different beamsplitters, has multiple different light sources that can be used, and uses a computer software that allows for many other experimental parameters to be changed. This allows for more control of the experiment; however it also makes use of the device more complicated than use of the Bomem.

This spectrometer was used to measure the optical spectra of several samples which were found to have cutoff values that were out of the range which could be measured using the Bomem. This included samples with high-wavenumber cutoffs (i.e. out of the range of the Globar source) and those with low-wavenumber cutoffs (i.e. out of the range of the MCT detector). The setup procedures for the low-wavenumber analysis and the high-wavenumber analysis were slightly different.

Before discussing the differences between the procedure, however, the parameters that were held the same for both procedures should be outlined. A photograph of the instrument is given in Figure 2.18. The spectrometer itself can be oversimplified into four compartments; one that contains the upper half of the device and three that make up the three thirds of the lower half. In the upper half is the Michelson interferometer itself. The mirrors inside are attached to motors and can be adjusted by computer for two reasons. The first of these is so that the outgoing beam can be directed to a different location (the reason for which one would want to do this will be illustrated shortly) and the second is so that the ZPD can be found.

The compartment at the bottom right contains a pair of mirrors, various light sources, and an aperture wheel. A photograph of the compartment is given in Figure 2.19. The mirrors are used to direct the light into the appropriate location such that measurements can be performed. The aperture wheel is used to limit the diameter of the beam which strikes the sample. There are three light sources that are fitted in the device: a tungsten lamp (for near-IR

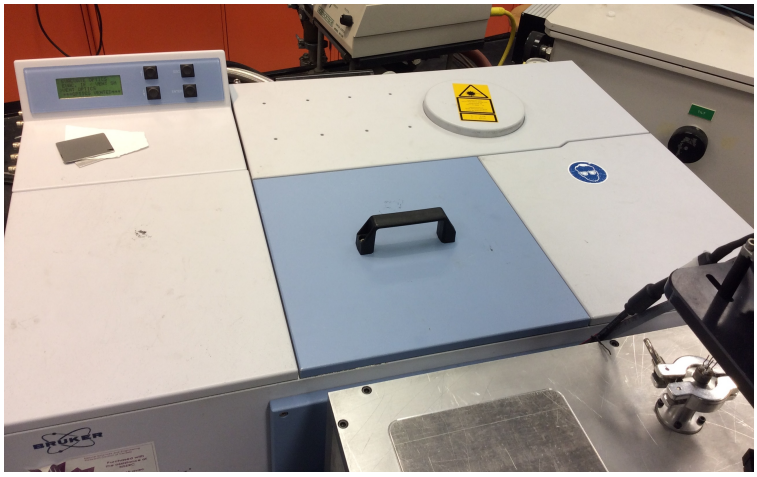

Figure 2.18: Photograph of the Bruker IFS 66v/S FTIR Spectrometer.

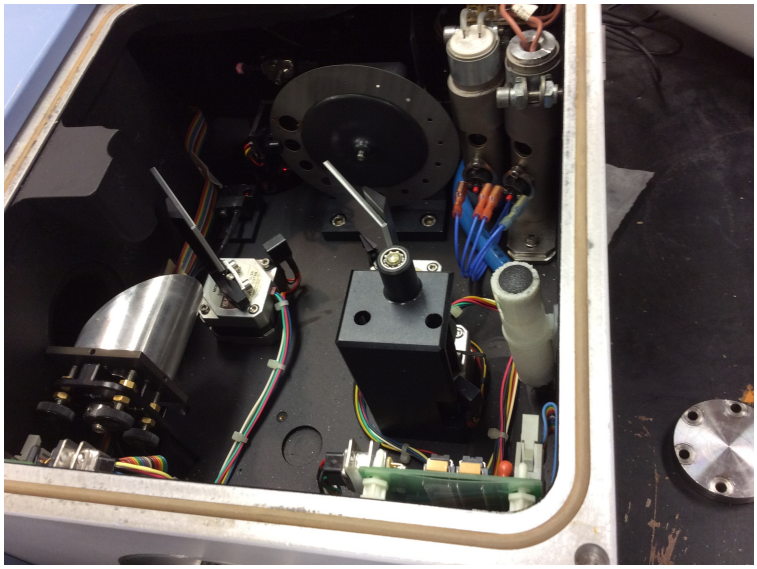

Figure 2.19: Photograph of the lower right compartment of the Bruker IFS 66v/S FTIR Spectrometer.

measurements), a Globar (for mid-IR measurements), and a mercury-arc lamp (for far-IR measurements).

For all of the measurements performed using this device, the parameters were set with a computer software called OPUS. This software allows for the setup of many parameters. These include but are not limited to: aperture size, scanning velocity, measurement range, phase resolution, apodization function, and phase correction. The parameters that were common to all measurements performed with the Bruker are displayed in Table 2.3.

The setup for measuring spectra of the samples with the low-wavenumber

Table 2.3: Parameters used for Bruker measurements.

Resolution	4 cm^{-1}
Number of Scans	128
Phase Correction Method	Mertz
Apodization Function	Blackman-Harris 3-Term
Zerofilling Factor	2
Range	0-9000 cm^{-1}
Aperture Size	9 mm

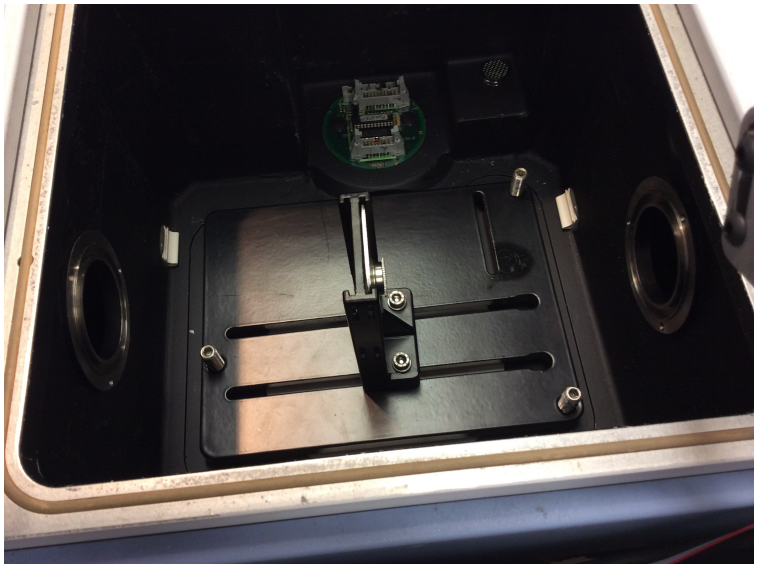

Figure 2.20: Photograph of the lower middle compartment of the Bruker IFS 66v/S FTIR Spectrometer.

cutoff was relatively simple. In the middle lower compartment (Figure 2.20), there is a sample holder that is similar in appearance to the one in the Bomem. Unlike the holder in the Bomem, however, this holder does not have a small slot into which the sample can slide. Instead, the sample needed to be fixed to the holder with a small amount of vacuum grease. This sample was overfilled with light during measurement in order to ensure that an average value of the spectrum over the entire sample was obtained.

The detector used to carry out these measurements was located in the bottom left compartment (Figure 2.21). This detector was a deuterated triglycine sulfate (DTGS) detector. This is a thermal detector with a Curie temperature of 49°C, which ensures that it can be operated at room temperature without being cooled. Because it is a thermal detector (and therefore "slow"), however,

Figure 2.21: Photograph of the lower left compartment of the Bruker IFS 66v/S FTIR Spectrometer.

it is necessary to reduce the scanning velocity using OPUS to 1.6 kHz (the minimum allowed by the device). This ensures that the detector gives accurate results for the spectra.

In order to perform the low-wavenumber measurements, the Globar light source was used. This source provides enough light in the required range to be used for these cutoff measurements. Also used was a 6 micron Mylar beamsplitter. This beamsplitter is useful in the low-wavenumber range and as such was ideal for these measurements.

Similarly to how measurements were performed using the Bomem, the background spectrum was taken using the empty hole and the sample spectrum was taken with the sample fixed in place. The two spectra were then divided in the appropriate manner by the software, and a transmission spectrum was generated.

The setup for performing the high-wavenumber measurements was more complex. Unlike the setup for the low-wavenumber measurements, the two leftmost lower compartments were not used at all. Instead, an optical box (Figure 2.22) that is attached to the lower right compartment was used. The interior of this box contains a series of mirrors and an aperture that allow for

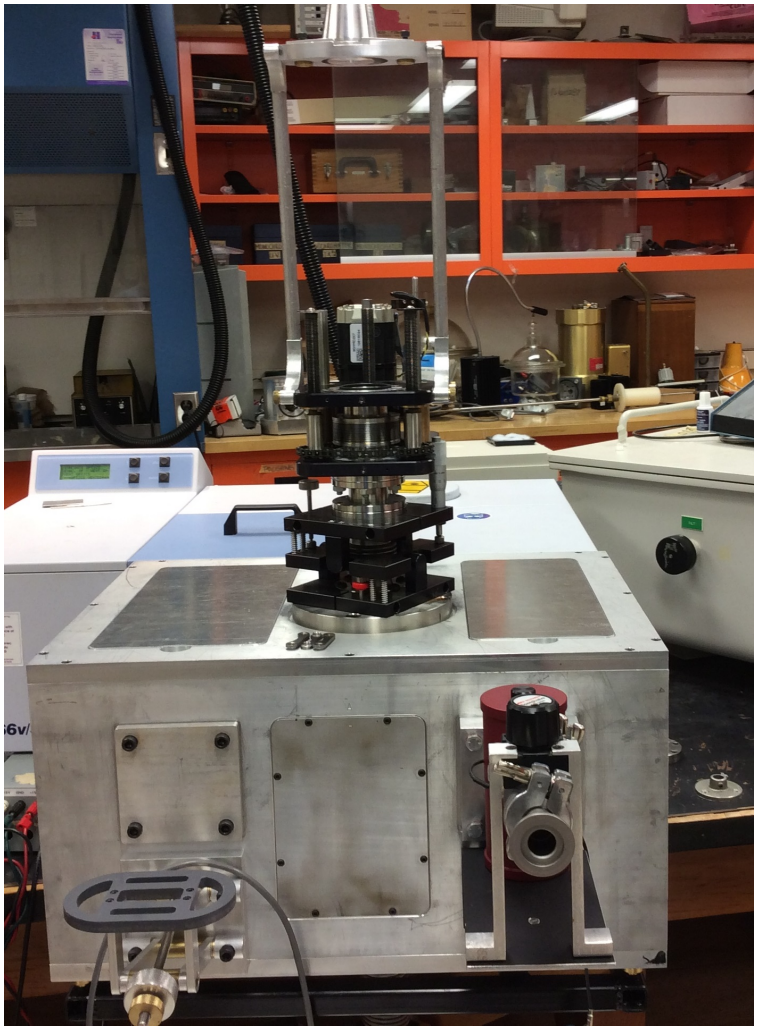

Figure 2.22: Photograph of the outside of the optical box for the Bruker IFS 66v/S FTIR Spectrometer.

the outgoing beam to be focused onto the sample and then through to an MCT detector. Because an MCT (i.e. a "fast") detector was used, it was possible to increase the scanning velocity to 20.0 kHz. The alignment procedure for the optical box is described in Appendix C.

Because the optical box had the original purpose of being used for low-temperature optical measurements, it followed that the most convenient method for mounting the samples for measurement involved mounting them onto a cryostat (Figure 2.23).

On the tip of the cryostat can be attached a copper sample holder (Figure 2.24). This holder has two holes in it; this allows for two samples to be mounted at once. In order to perform the high-wavenumber measurements, the samples

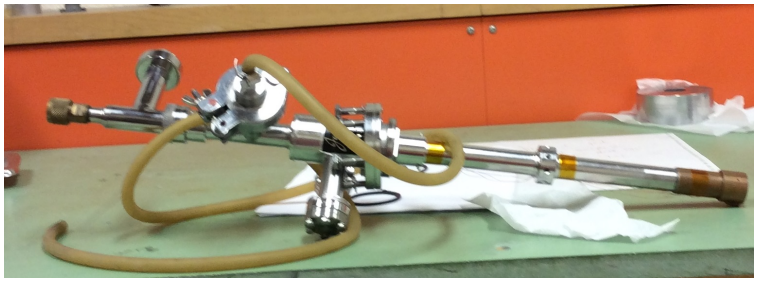

Figure 2.23: Photograph of the cryostat used for the Bruker-based optical measurements.

Figure 2.24: Photograph of the copper sample holder that attaches to the cryostat tip.

were fixed to the holder using a small quantity of vacuum grease.

In order to actually perform measurements, the cryostat must be placed into a sample chamber within the optical box by fixing it to a linear translator. The sample chamber is isolated from the interior of the box by way of a KBr window. The linear translator is a device which allows for the cryostat to be moved vertically by way of a motor connected to a computer. It is by way of this device that two samples can be measured in rapid succession; the cryostat can be moved such that one sample is located in the beam path for one set of trials and then, by way of the translator, moved to another location such that the second sample is located in the beam path.

To collect a background spectrum, the translator moved the cryostat such

that the beam path passed unimpeded underneath it to the detector. The sample spectra were gathered by translating the cryostat to positions where the beam passed through one of the two samples. A consequence of this method is that the samples could not be overfilled with light. Overfilling would cause some of the beam to be blocked by the sample holder rather than passing through the sample, which would in turn cause the background spectrum to not be the true baseline for the measurement. As such, the samples were slightly underfilled. This was a compromise that allowed for as much of the sample as possible to be used in order to obtain a true average spectrum over the entire surface of the sample while still allowing this method for obtaining the background spectrum to be accurate.

Identically to the Bomem optical measurements, the sample spectrum was divided by the background spectrum in order to obtain a transmission spectrum for the sample under investigation.

The high-wavenumber measurements were performed using the tungsten lamp as a light source and a KBr beamsplitter. The Globar does not produce enough light in the high-wavenumber range, and as such it was necessary to switch to a light source that does.

Like the measurements performed using the Bomem, the resolution used in all Bruker experiments was set to 4 cm^{-1} in order to avoid any fringing effects in the spectrum. Five spectra were taken of each sample in order to determine an averaged value for cutoff. Each of these spectra were an average of 64 scans of the interferometer. Because the MCT is a quantum (and therefore "fast") detector, a much higher scanner velocity of 20.0 kHz was used in order to gather data quickly. The OPUS software was used to both set these parameters as well as gather the spectra for these samples.

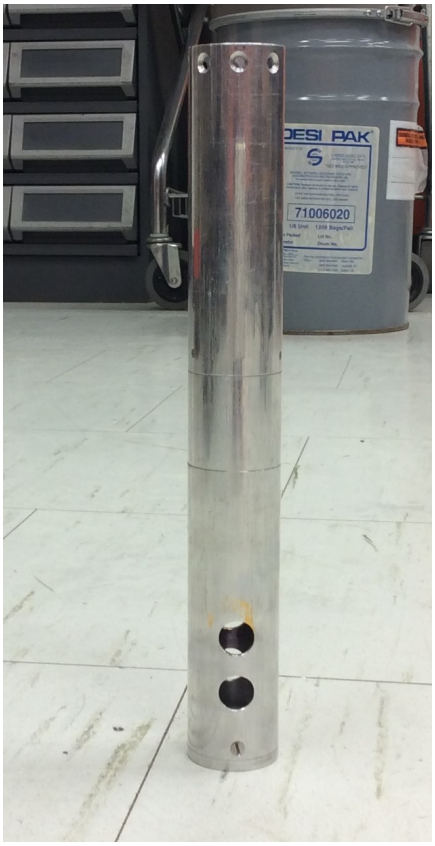

Figure 2.25: Photograph of the radiation shield for the cryostat.

2.5.4 Low-Temperature Measurement

The Bruker spectrometer was also used to perform temperature-dependent measurements of the optical cutoff for seven different samples. The optical setup was nearly identical to that used to perform the high-wavenumber measurements as outlined in the previous section. The only notable difference is the light source: instead of the tungsten lamp the Globar was used. This was because the samples measured had cutoff values in the mid-infrared range at room temperature.

In order to perform optical measurements as a function of temperature, the sample needed to be secured to the holder with a thermally conductive adhesive. The holder was then attached to the cryostat and a radiation shield (Figure 2.25) was placed over the cold finger of the cryostat. The cryostat was then inserted into the sample chamber in the optical box and secured to the linear translator.

The sample chamber was evacuated overnight to a pressure of approximately 9×10^{-7} Torr. This ensured that there was no air within the sample chamber. This is important because the presence of air within would cause a significant amount of condensation to occur which would in turn cause the spectra obtained to contain absorption lines. In addition to this, air in the sample chamber would also prevent the cryostat from being isolated from room temperature. This would ensure that a significant quantity of liquid helium would evaporate incredibly quickly. Since liquid helium is rather expensive, it is desirable to not unnecessarily lose any to this evaporation.

After the chamber was evacuated, liquid helium was used to bring the temperature to 4 K. This was done by inserting a transfer tube into the top of the cryostat at one end and a liquid helium dewar at the other. The temperature of the cryostat was monitored by way of a silicon diode temperature sensor. Once the temperature reached 4 K, twenty minutes were allowed to elapse in order to allow the entire sample to equilibrate at this temperature. At this point, optical measurements were carried out identically as outlined in the previous section for the high-wavenumber measurements. As before, five spectra were obtained.

The cryostat is attached to a temperature controller. The temperature controller has two functions relevant to the measurements in this section: it is connected to the temperature sensor which allows for the current temperature of the cryostat to be monitored and it is connected to an electronic heater which allows for the temperature of the cryostat to be adjusted. Once the measurements at 4 K were finished, this temperature controller was used to increase the temperature of the sample to 50 K. Again, twenty minutes were allowed to elapse in order to allow the temperature of the sample to reach equilibrium. Once this was done, the optical transmission spectra were taken. This procedure was repeated for several different interim temperatures between 4 K and 300 K. This allowed for the observation of optical cutoff as a function

of temperature.

Initially, Wakefield Thermal Paste was used to secure the samples to the holder. This was done to ensure that there was sufficient thermal contact between the holder (i.e. the cryostat) and the sample. Use of this paste, however, led to complications (that will be discussed in further detail in the next chapter) that adversely affected the measured optical spectra. As such, the affected samples were completely cleaned of thermal paste by submerging them in a beaker of acetone and placing the beaker in an ultrasonic cleaner for three minutes.

As a substitute for the thermal paste, GE varnish was used to secure the samples to the holder. This adhesive did not adversely affect the optical measurements.

2.6 Methods of Analysis

2.6.1 Optical

In order to determine the optical cutoff wavenumber for a given sample, a short Java program was written. This program was used to read in a .dat file that was obtained from the appropriate spectroscopy software (depending on the spectrometer used) that contained the wavenumber and the transmission percentage as a coordinate pair. The program then read each pair line by line starting from the low wavenumber end until it found the first transmission value that was below 5 percent. The associated wavenumber was then stored as a variable. The program then continued to read line by line to ensure that the transmission stayed below 5 percent within a tolerance of 0.5 percent. If this was not the case, the program then searched for the next wavenumber that fit the criteria. If it was, then this wavenumber was taken to be the cutoff value. The reason that the program was made to check all values after the first detected “cutoff” was so that any random drops in the data were not incorrectly

taken to be the cutoff value.

There is no universally accepted definition for what constitutes the optical cutoff wavenumber; it is generally defined as the wavenumber at which the absolute transmission drops below a given value. For the purposes of this research, the cutoff wavenumber was taken to be the value at which the absolute transmission drops below 5 percent. This value was chosen because it is relatively close to zero and is generally observed to be above the electronic noise threshold of the spectrometers. Some experiments take the cutoff transmission percentage to be a much higher value (as much as 50 percent in some cases), but this is generally done with filters that cut off rather sharply. Since it was observed that the porous silicon filters manufactured for this project did not universally cut off sharply, it was decided to take a relatively low transmission percentage to be the cutoff threshold.

2.6.2 Topological

The topological analysis of the SEM images was performed using a program developed by the National Institutes of Health called ImageJ [46]. Though primarily used for biological study, this program has some features that proved incredibly useful for analyzing the SEM images.

There were two major topological parameters that were analyzed using this software. The first of these was the pore number density. To illustrate the method by which the pore number density was obtained, the SEM image for Sample 6 will be used. One of the SEM images for this sample is given in Figure 2.26.

ImageJ contains a built-in "Particle Analysis" tool. This tool allows for, among other functions, the number of particles within a given region to be determined. Before this could be done, however, there are two important processes that needed to be carried out. The first of these was the determination of the size of the region in which the analysis would be performed. Conve-

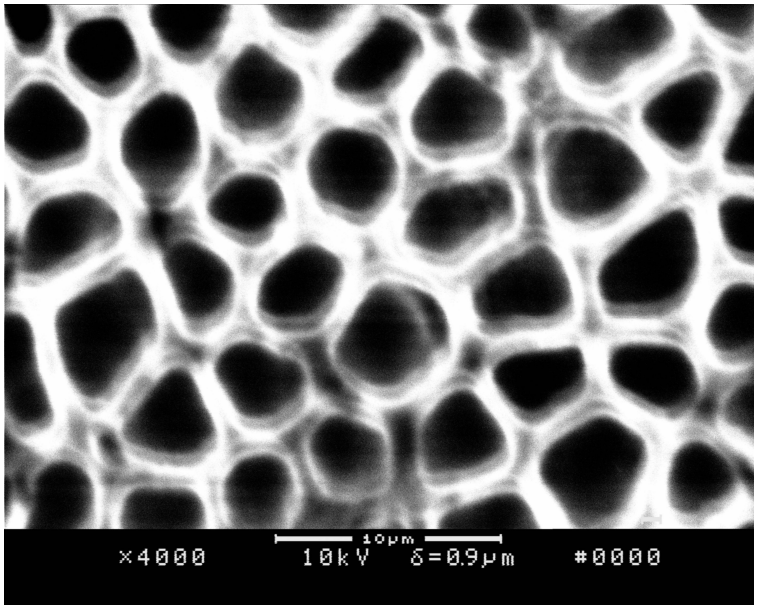

Figure 2.26: SEM image of Sample 6.

niently, ImageJ contains a measuring tool that returns the length in the form of a number of pixels between two points. This tool was used to determine the length of the scale bar in pixels. The measuring tool also returns the angle that the measurement line makes with the bottom edge of the image. This ensures that the measurement of the scale bar is accurate; the measuring line is straight across the bar and not at an off-angle. For the sake of convenience, each measured region had an area of 100 (i.e. 10 μm by 10 μm) μm^2. Though this region may seem small, it allowed for the regions measured to be selected by eye. This ensured that any aberrations in the image due to high shadowing could be avoided.

The other process which needed to be carried out is the thresholding of the image. The particle analysis tool only works on binary (i.e. black and white) images. ImageJ has a thresholding tool which allows for the image to be converted to binary. This tool was used to convert the image such that each of the pores appeared to be separate from one another. For this part of the analysis, any reduced area of the pores was unimportant; only a number density was required. The image from Figure 2.26 after thresholding is given in Figure 2.27. The thresholding was simply performed by eye.

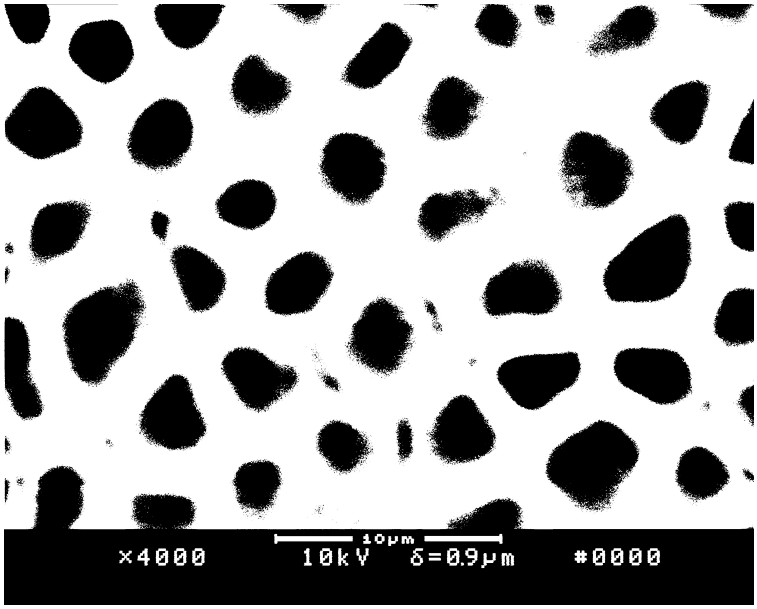

Figure 2.27: Thresholded SEM image of Sample 6 for pore number density analysis.

Once the image was thresholded, the particle analysis tool could be used. This tool analyzes the number of black spots in an area. Before use, the tool can be set so no analysis on black spots that are below a certain size is performed. This ensures that no random single dark pixels are analyzed as porous structure. Once this was done, the tool can be used. It gives many different parameters (including percent coverage, average size, etc.), but the parameter of interest here was the number of dark spots within the region. This allowed for a value for the number of pores in a given area to be obtained, thus giving the pore number density value. On each image, this was performed on two different spots. Since there were 3 images for each sample, 6 values for pore number density for each sample were obtained. This allowed for an average value for pore number density to be taken in order to give a representative pore number density value for the entire sample.

The second topological property of each sample that was measured was the area of the sample's surface that was covered by pores as a percentage (hereafter referred to as the "percent coverage"). These measurements were performed nearly identically to the pore number density measurements. The

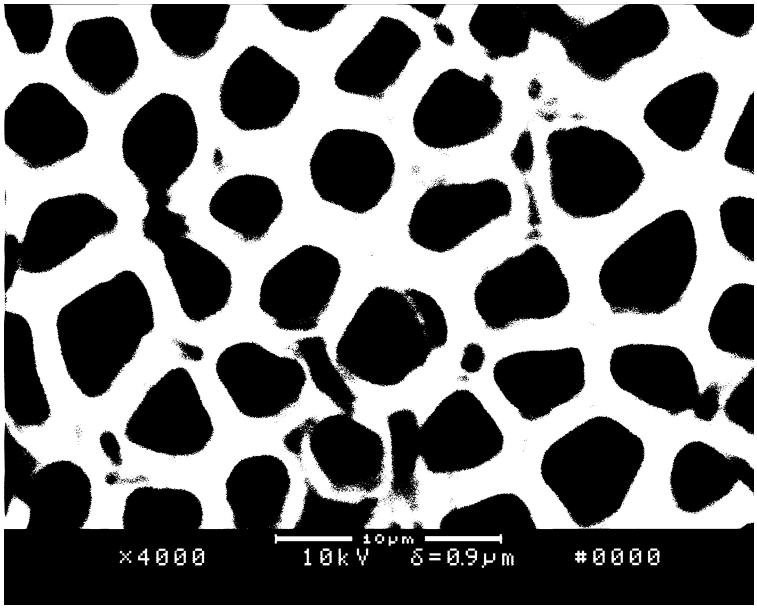

Figure 2.28: Thresholded SEM image of Sample 6 for percent coverage analysis.

only difference was the level of thresholding used. For the percent coverage measurements, the thresholding used was much smaller than was used for the pore number density measurements. This prevented the percent coverage from being grossly underestimated. Unfortunately, this causes shadows and other dark spots to be counted in the percent coverage measurements. As such, these measurements are likely an overestimate of the true value. The particle analysis tool returns the number of dark pixels in an area as a percentage. This was done over the entire image for three different images in order to determine a representative value for the average percent coverage over the entire surface. The thresholded image of Sample 6 for percent coverage measurements is given in Figure 2.28.

Chapter 3

Results

3.1 Room Temperature

The room temperature measurements of optical cutoff, pore number density, and pore coverage will be discussed here. Table 3.1 contains the results of these measurements as determined by the methods outlined in the previous chapter. The corresponding optical spectra and SEM images are given in Appendix A.

Samples 9, 32, and 33 could not be imaged using the SEM in such a way that any porous structure could be well-resolved. The reason for this is likely that the surface of the wafer did not contain deep pores. This would explain why no optical cutoff could be determined for these samples; the surface was more akin to a rough, bumpy silicon surface rather than a surface containing true scattering centers. Because the surface was rough, it is likely that some scattering occurs (thus explaining why the transmission spectra were not identical to that of unetched silicon as given in Appendix A). However, scattering from surfaces of differing degrees of roughness does not have identical effects [47]. As such, it is likely that a slightly rough silicon sample does not have the same scattering effect as does scattering from a surface containing true scattering centers. This explains why the resulting spectra from these samples appears to more closely resemble a unetched silicon spectrum rather than the spectra from the other

Table 3.1: Table of optical and topological results for the room temperature measurements. In this table are the cutoff ω, the pore number density n, and the pore coverage c. The cutoff values labelled as ">7000" have a cutoff that is of a higher wavenumber than the measurable range of the detectors used.

Sample No.	ω (cm^{-1})	n (pores/100 μm^2)	c (%)
1	1406 ± 1.0	7.3 ± 1.6	64.9 ± 2.0
2	1089.3 ± 1.0	7.8 ± 0.8	47.6 ± 2.3
3	1163.3 ± 1.0	6.5 ± 0.8	58.2 ± 2.5
4	1292.2 ± 1.0	9.2 ± 1.5	45.2 ± 1.1
5	1868.8 ± 1.0	15.7 ± 1.4	46.9 ± 2.0
6	1165.3 ± 1.0	6.7 ± 1.4	44.2 ± 3.6
7	1492.7 ± 1.0	8.3 ± 0.8	47.8 ± 2.9
8	1209.2 ± 1.0	11.3 ± 1.2	46.7 ± 4.1
9	>7000	-	-
10	2399.2 ± 1.4	14.0 ± 1.5	52.5 ± 1.1
11	3017.3 ± 1.0	16.0 ± 1.5	58.0 ± 4.7
12	>7000	14.2 ± 1.7	50.4 ± 3.3
13	2067.5 ± 1.0	19.5 ± 1.0	65.0 ± 4.1
14	2487.6 ± 2.5	18.2 ± 0.4	65.3 ± 3.7
15	2138.5 ± 1.0	15.5 ± 1.0	37.9 ± 4.2
16	3230.1 ± 14.8	16.5 ± 0.5	51.0 ± 4.5
17	2347.9 ± 3.2	14.8 ± 1.2	49.6 ± 6.9
18	>7000	16.8 ± 1.5	72.6 ± 3.2
19	2948.9 ± 1.0	15.2 ± 0.8	60.7 ± 5.7
20	3186.5 ± 7.8	13.3 ± 1.0	65.2 ± 0.3
21	2283.5 ± 5.3	14.5 ± 1.2	45.7 ± 0.4
22	4730.1 ± 10.6	15.3 ± 1.6	55.1 ± 5.0
23	6224.1 ± 10.1	9.8 ± 1.0	84.5 ± 3.3
24	>7000	14.3 ± 1.2	69.1 ± 2.4
25	6777.0 ± 13.0	9.7 ± 1.0	77.2 ± 5.9
26	2223.3 ± 1.0	12.2 ± 1.3	36.6 ± 3.4
27	2598.7 ± 1.0	16.0 ± 1.7	58.9 ± 2.2
28	114.9 ± 1.1	0.30 ± 0.04	7.7 ± 1.6
29	677.7 ± 3.2	1.6 ± 0.4	7.3 ± 3.0
30	791.8 ± 1.7	0.18 ± 0.04	0.42 ± 0.20
31	995.9 ± 7.5	0.23 ± 0.04	0.25 ± 0.10
32	>7000	-	-
33	>7000	-	-
34	6263.7 ± 5.8	25.8 ± 5.3	39.8 ± 3.5

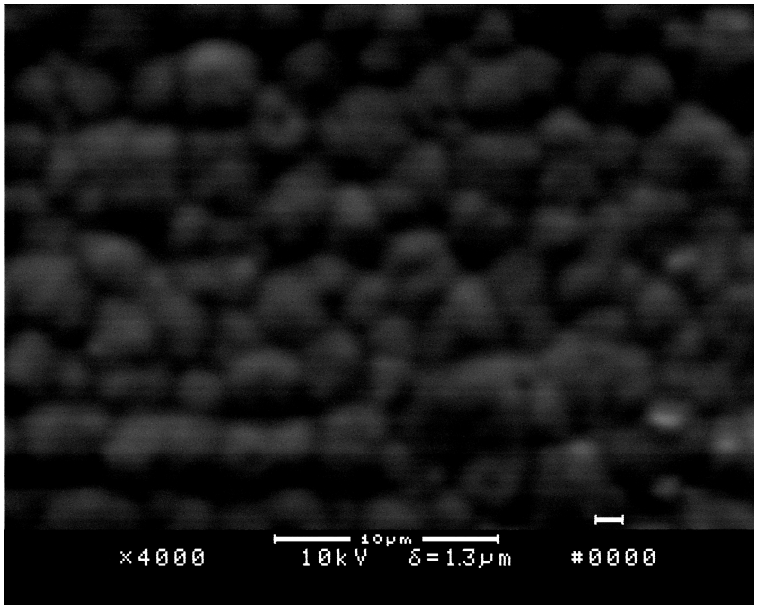

Figure 3.1: SEM image of the center region of Sample 34.

porous samples.

Sample 34 also exhibited strange results. Upon imaging this sample, it was found that the surface of this sample could be divided into three distinct parts: a center region, a ring outside the center region (hereafter referred to as "Ring 1"), and a ring outside Ring 1 (hereafter referred to as "Ring 2"). Rings 1 and 2 appeared as expected; they were porous samples similar to the other samples. However, they were of very different pore densities. As such, the error bar for pore number density for this sample is very large. The center region, however, was both very strange in appearance and difficult to image. It was not porous but instead appeared to be rough and bumpy. An image of the center region of Sample 34 is given in Figure 3.1. Because of the large discrepancy between the three regions of this sample, its data point was not included in any of the further analysis.

Figure 3.2 shows the transmission spectra along with an SEM image for four samples: 1, 16, 26, and 28. Each of these is a different colour. Figure 3.3 gives the cutoff as a function of pore number density for all of the samples unless already mentioned as excluded from the data set. The coloured points that match the coloured lines in Figure 3.2 correspond to one another (i.e. the

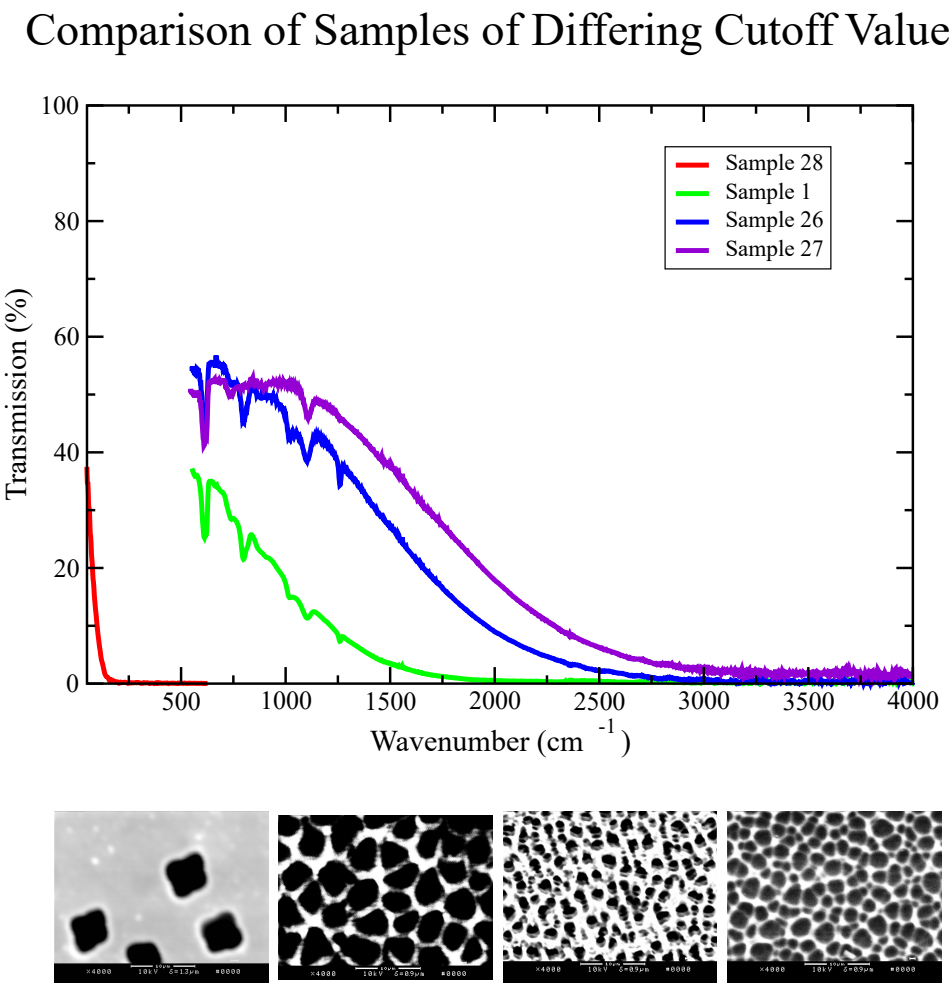

Figure 3.2: Comparison of transmission spectra for four select samples. The SEM images at the bottom are the images for these samples. From left to right these are: Sample 28, Sample 1, Sample 26, and Sample 27. All images were taken at 4000X magnification.

red line and red point both match to Sample 28).

In general, there does appear to be a trend between cutoff wavenumber and pore number density; an increasing pore number density corresponds to an increasing cutoff. There are however several points that do not appear to follow this trend. These points are represented by brown points and are labelled as "higher outliers". Additionally, there are other anomalous points that are represented by orange points and are labelled as "lower anomalies". These anomalies will be further discussed later in this section.

Before discussing the outliers and anomalies, however, it is illustrative to look at the dependence of the cutoff on the pore coverage. A plot of this is given

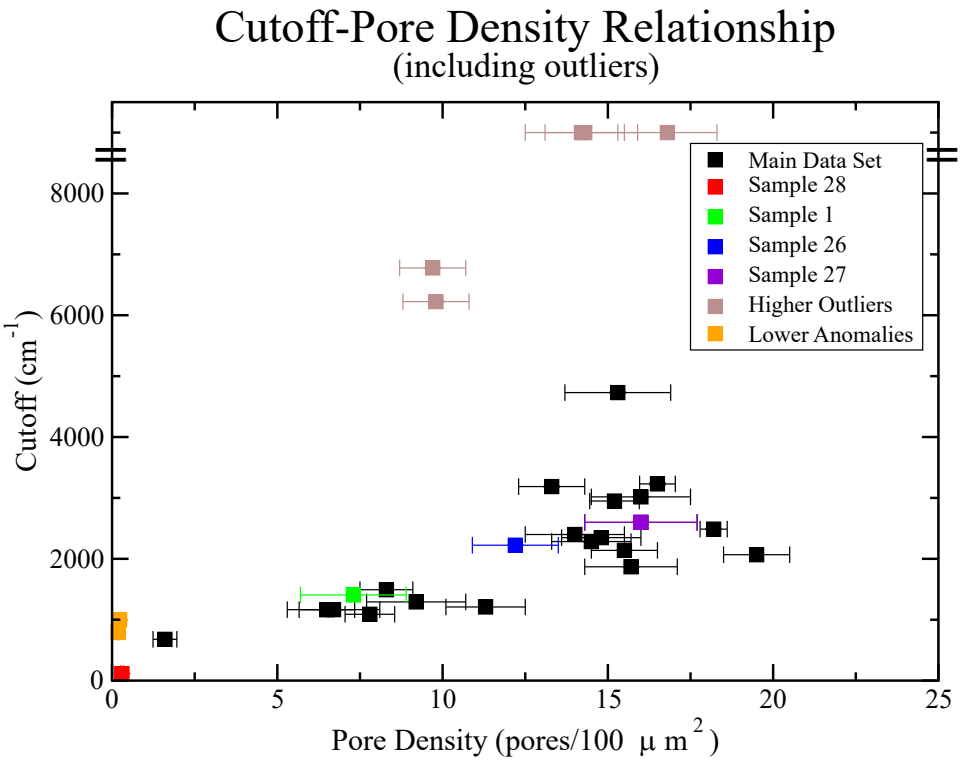

Figure 3.3: Plot of cutoff wavenumber as a function of pore number density (including outliers). The higher outliers (Samples 12, 18, 23, 24, and 25) are marked by brown points and the lower anomalies (Samples 30 and 31) are marked by orange points. The points above the break in the y-axis are those that had a cutoff that was higher than was measurable by the detectors used.

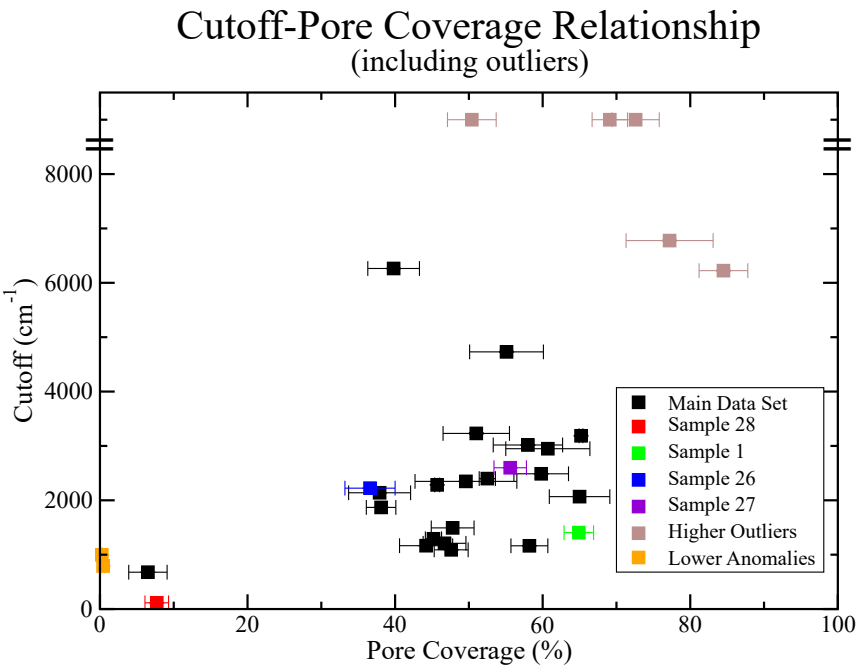

Figure 3.4: Plot of cutoff wavenumber as a function of pore coverage (including outliers). The points above the break in the y-axis are those that had a cutoff that was higher than was measurable by the detectors used.

in Figure 3.4. The coloured points match those of Figure 3.3. From this plot, it is obvious that the majority of the points fall between about 35-65% pore coverage and that these points do not follow any general trend when comparing cutoff and pore coverage. The outliers, however, have pore coverage values that are outside of this range. The higher outliers have high pore coverage values (>69%) and the lower anomalies have low pore coverage values (<1%).

The explanation for the higher outliers is similar to that of Samples 9, 32, and 33 as discussed previously. An image of one of the higher outliers (Sample 25) is given in Figure 3.5. From this image, it is obvious that there is very little space between pores. Furthermore, it appears that some of the pores are merging together. This may be due to the pore walls becoming very thin and collapsing. Because the walls are so thin, it is possible that the pores are not acting as proper scattering centers and instead are giving the same effect as would a highly rough surface. This explanation holds true for the other higher

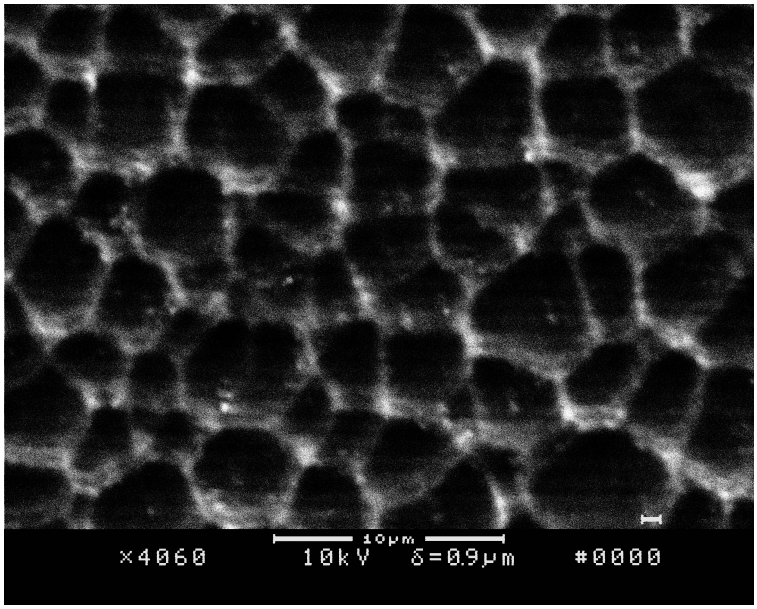

Figure 3.5: SEM image of Sample 25, a higher outlier.

outlier points as well. Because of this, the transmission properties for the higher outliers are not the same as those of the other samples.

The lower anomalies, however, must be explained in a different manner. Figure 3.6 shows an SEM image of Sample 30. In this image, it can be seen that there are large regions that do not contain any pores. As such, it is likely that there are regions of the sample that act, in terms of transmissive properties, as polished silicon. If this were true, the average transmission spectrum over the entire sample would not cutoff perfectly to zero but instead to some slightly higher value. Since the cutoff is taken to be the point at which transmission drops below 5 percent, it follows that this value is higher in wavenumber than the value that would be given purely by scattering. The transmission spectrum for Sample 30 is given in Figure 3.7. From this image, it can be seen that there is indeed a non-zero background to the transmission. For Sample 31, a similar effect can be seen. As such, it can be reasonably concluded that this explanation for the lower anomalies may have some merit.

Once the outliers and anomalies are removed from the plot in Figure 3.3, it can be seen that there is a trend between pore number density and optical cutoff. As the pore number density of a sample is increased, the optical cutoff

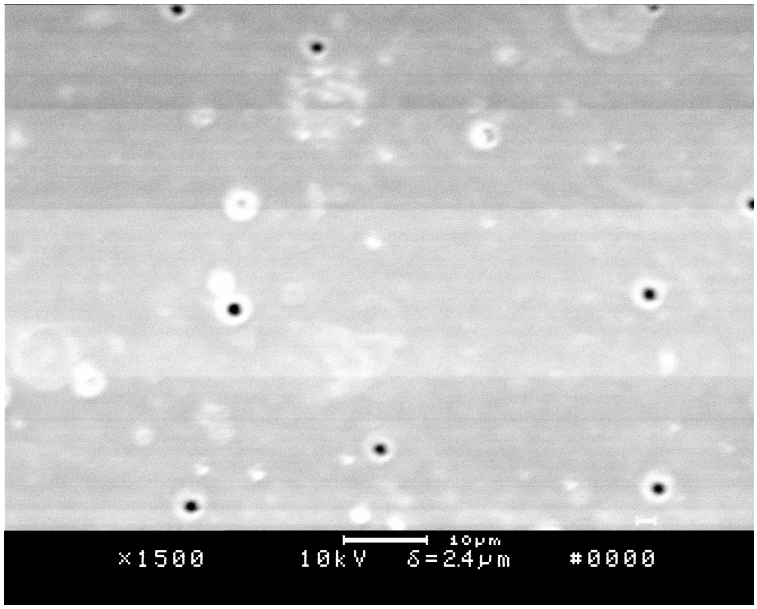

Figure 3.6: SEM image of Sample 30, a lower anomaly. Note the smaller magnification scale of 1500x rather than 4000x.

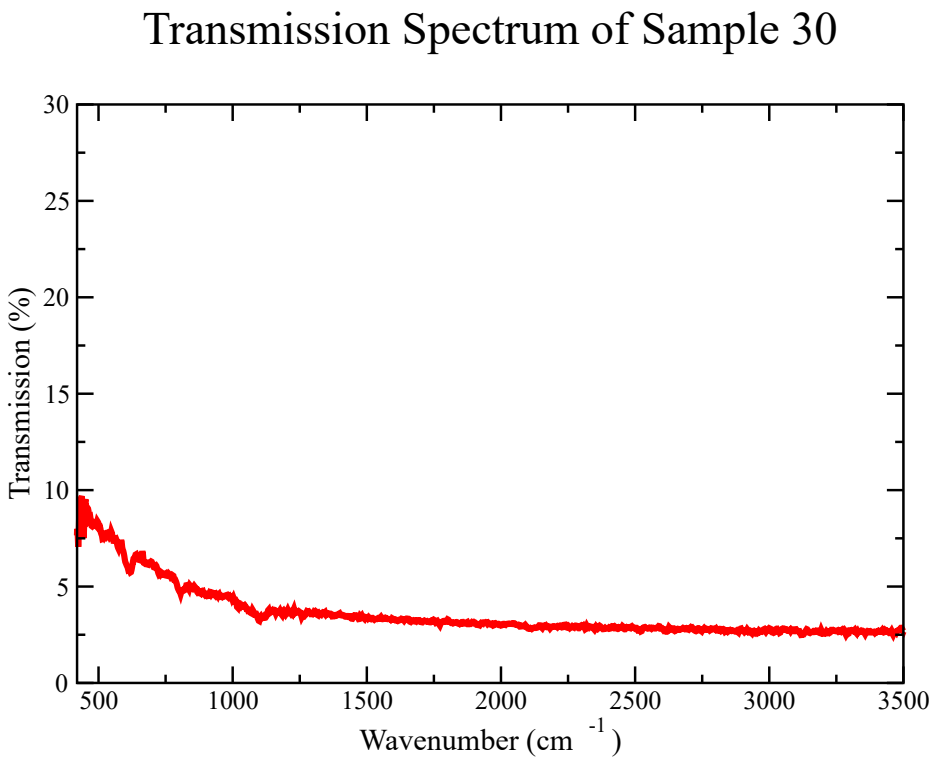

Figure 3.7: Plot of the transmission spectrum for Sample 30, a lower outlier. Note that the % transmission does not drop to 0%.

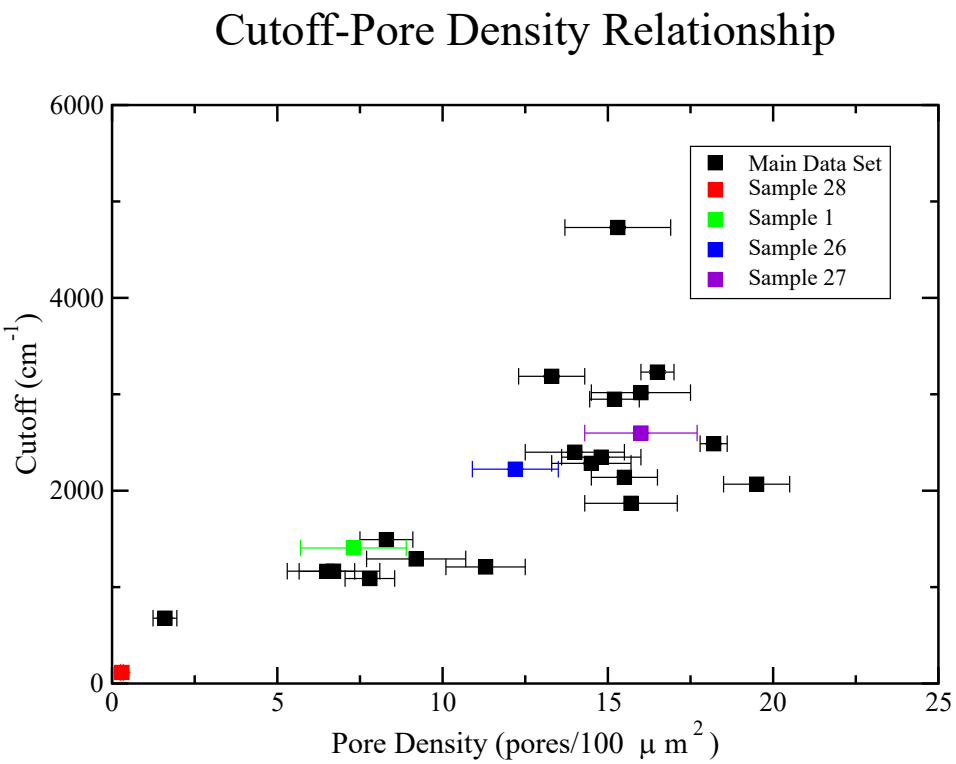

Figure 3.8: Plot of the relationship between pore number density and cutoff wavenumber (excluding outliers).

increases in wavenumber (i.e. moves toward the near-infrared range). This final result is shown in Figure 3.8.

This result implies that the optical cutoff of macroporous silicon is governed by the spacing between the pores. This is because, for a regular distribution, that the spacing between pores should be proportional to $d^{-1/2}$, where d is the number density [48]. To confirm this, an ImageJ plugin [49] that was designed to find the nearest-neighbour distance (NND) between particles on a binary image. It does this by measuring the distance in pixels between the centroids of each particle. The NND for each particle is the shortest of these distances. Using this plugin, it was possible to determine the NND between pores. Figure 3.9 shows the relationship between the NND and the optical cutoff.

Unlike previous plots, the cutoff value was plotted in terms of wavelength rather than wavenumber. This was done in an effort to compare the actual wavelength of the light being filtered out with the pore spacing for a given

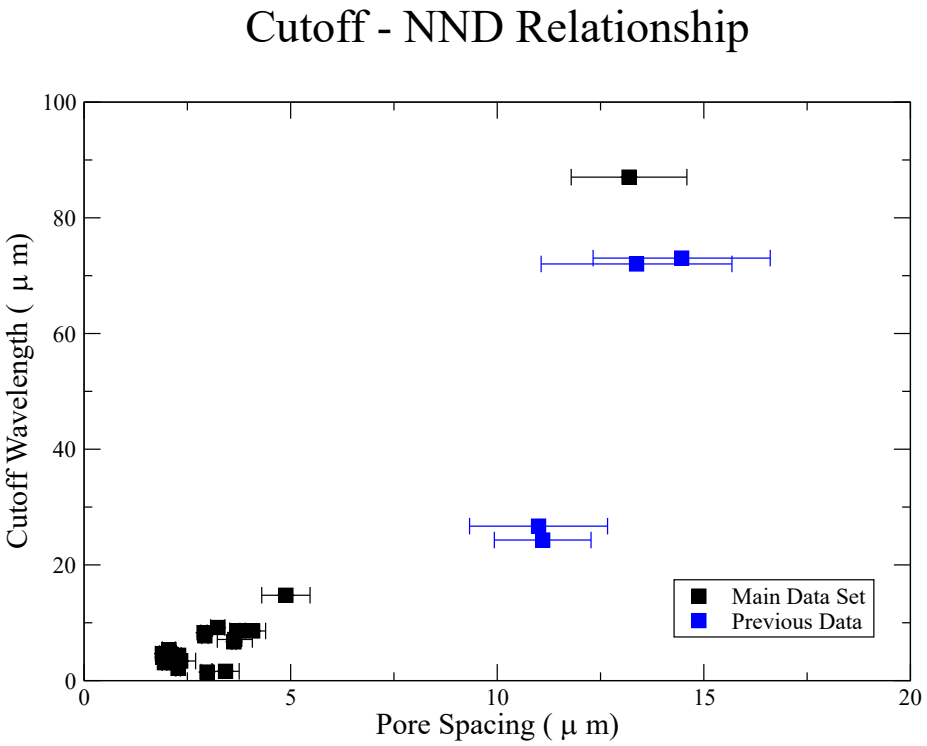

Figure 3.9: Plot of the relationship between NND and cutoff wavelength. To further illustrate the relationship further, results from previous work [50] were included. The axes on the inset graph map the same property as do the main graph. The points for the lower anomalies and the higher outliers were not included.

sample rather than simply observing a trend. Figure 3.9 shows that not only is there a clear trend linking the NND and the cutoff wavelength, but also that the average NND and the cutoff are on a similar order of magnitude. This suggests that the scattering mechanism governing the filtration properties of the filters is determined by the average pore spacing. For the NND values and associated error bars, see Appendix B.

It is also worth noting that the lower anomalies have relatively large average pore spacing values. In Figure 3.7, it can be seen that the transmission spectrum reaches a constant transmission percentage at approximately 2500 cm^{-1}, or 4 μm. This value is much smaller than the average pore spacing. This may provide some insight into any limiting factors to macroporous silicon filters; it is possible that the scattering mechanism does not operate as expected if a) the coverage value is small and b) if the spacing between pores is very large in comparison to the cutoff wavelength.

An estimate of the average pore diameter was also obtained using the topological values determined via the SEM images. This was done in an effort to determine whether or not the linear dimension of the pores themselves were in any way related to the optical cutoff. To do this, first the average area of a single pore was determined. This was done by using the following equation:

$$\langle A \rangle = \frac{\text{pore coverage}}{\text{pore number density}} \tag{3.1}$$

Once the area of a single pore was obtained, it was possible to determine the radius of a given pore. To do this, each pore was modelled to be circular. Though it is clear by simply observing the SEM images that each pore is not circular, this model should still provide some insight as to any relationship between the linear dimension of each pore and the optical cutoff. Because each pore is assumed to be circular, the average pore radius is given by:

$$r = \sqrt{\frac{A}{\pi}} \tag{3.2}$$

This value was determined for each of the samples that have viable SEM images. The results of these calculations are given in Table 3.2. Since the pore coverage value is likely an over-estimate of the true value as mentioned in Chapter 2, it follows that the area for a single pore and as such the pore radius are also upper bounds.

Similarly to the plot in Figure 3.9, the cutoff value was plotted in Figure 3.10 in terms of wavelength rather than wavenumber. This was done in an effort to compare the actual wavelength of the light being filtered out with the average linear dimension of the pores for a given sample rather than simply observing a trend. As before, the outlier values were excluded from this plot. Unfortunately, there was no clear trend that held for all samples between the cutoff and the pore radius for all of the samples as a single set.

The data of Figure 3.10 was plotted as a function of estimated pore radius as three different sample sets: those of the A-Type, those of the B-Type, and those of the C-Type. For the A- and B-Type samples, there was not any obvious consistent trend linking the cutoff wavelength and the pore radius; the data points were more clustered for each set rather than following a distinct correlation. For the C-Type samples, however, it did appear that there was indeed a possible trend: an increased pore dimension causes an increased cutoff wavelength.

In an attempt to confirm or refute this possible trend, data points from previously analyzed samples of the same type were added to the data set (as can be seen in Figure 3.10) [50]. These data points do seem to support the observation that filters of the C-Type exhibit the aforementioned correlation between the pore radius and the cutoff wavelength.

It should be noted that all of the C-Type samples have relatively low pore number density values. Because of this, it is possible that the scattering mechanism that governs the optical properties of macroporous silicon filters is different for pores that are spread further apart rather than those that are tightly

Table 3.2: Results of the average pore radius calculations.

Sample	Pore Area (μm^2)	Pore Radius (μm)
1	8.89 ± 1.97	1.68 ± 0.19
2	6.10 ± 0.69	1.39 ± 0.08
3	8.95 ± 1.17	1.69 ± 0.11
4	4.91 ± 0.81	1.25 ± 0.10
5	2.99 ± 0.30	0.98 ± 0.05
6	6.60 ± 1.48	1.45 ± 0.16
7	5.76 ± 0.66	1.35 ± 0.08
8	4.13 ± 0.57	1.15 ± 0.08
9	-	-
10	3.75 ± 0.41	1.09 ± 0.06
11	3.63 ± 0.45	1.07 ± 0.07
12	3.55 ± 0.48	1.06 ± 0.07
13	3.33 ± 0.27	1.03 ± 0.04
14	3.59 ± 0.22	1.07 ± 0.03
15	2.45 ± 0.31	0.88 ± 0.06
16	3.09 ± 0.29	0.99 ± 0.05
17	3.35 ± 0.54	1.03 ± 0.08
18	4.32 ± 0.43	1.17 ± 0.06
19	3.99 ± 0.43	1.13 ± 0.06
20	4.90 ± 0.37	1.25 ± 0.05
21	3.15 ± 0.26	1.00 ± 0.04
22	3.60 ± 0.50	1.07 ± 0.07
23	8.62 ± 0.94	1.66 ± 0.09
24	4.83 ± 0.44	1.24 ± 0.06
25	7.96 ± 1.02	1.59 ± 0.10
26	3.00 ± 0.42	0.98 ± 0.07
27	3.68 ± 0.41	1.08 ± 0.06
28	25.67 ± 6.34	2.86 ± 0.35
29	4.56 ± 2.14	1.21 ± 0.28
30	2.33 ± 1.23	0.86 ± 0.22
31	1.09 ± 0.47	0.59 ± 0.13
32	-	-
33	-	-
34	Not Reliable	Not Reliable

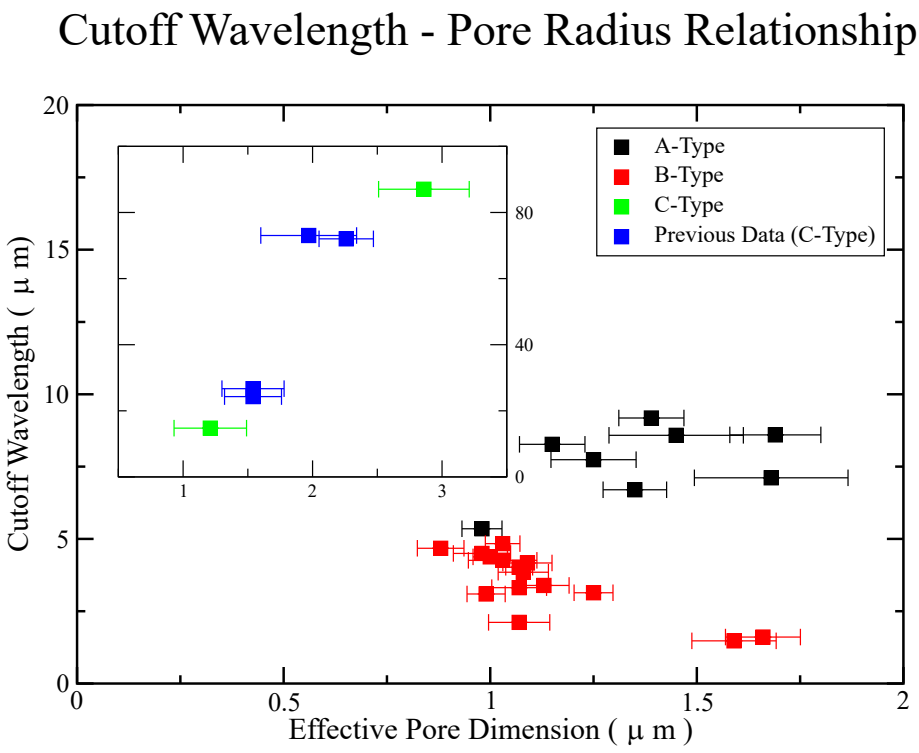

Figure 3.10: Plot of cutoff wavenumber as a function of pore radius. The axes on the graph of the inset map the same property as do the main graph.

packed.

A second definition of the cutoff wavenumber was also considered in attempting to define any correlation between the optical and topological properties of the filters. This definition was taken to be the value at which the transmission dropped below 50% of that of an unetched wafer at a wavenumber of 2000 cm^{-1}. This wavenumber was chosen because it is a value which should be in a region unaffected by absorption lines. Furthermore, inspection of the spectrum of the unetched samples of the different sample types showed that the transmission percentage was identical (to the nearest percent) for all types. Since this value was determined to be 54%, it follows that the point used for determining the cutoff under this second definition is 27%.

In Figures 3.11-3.14, the plots of the relationship between the second definition of the cutoff and the four topological measurements are given. The filters with cutoff values that were too high to be measured were excluded. From

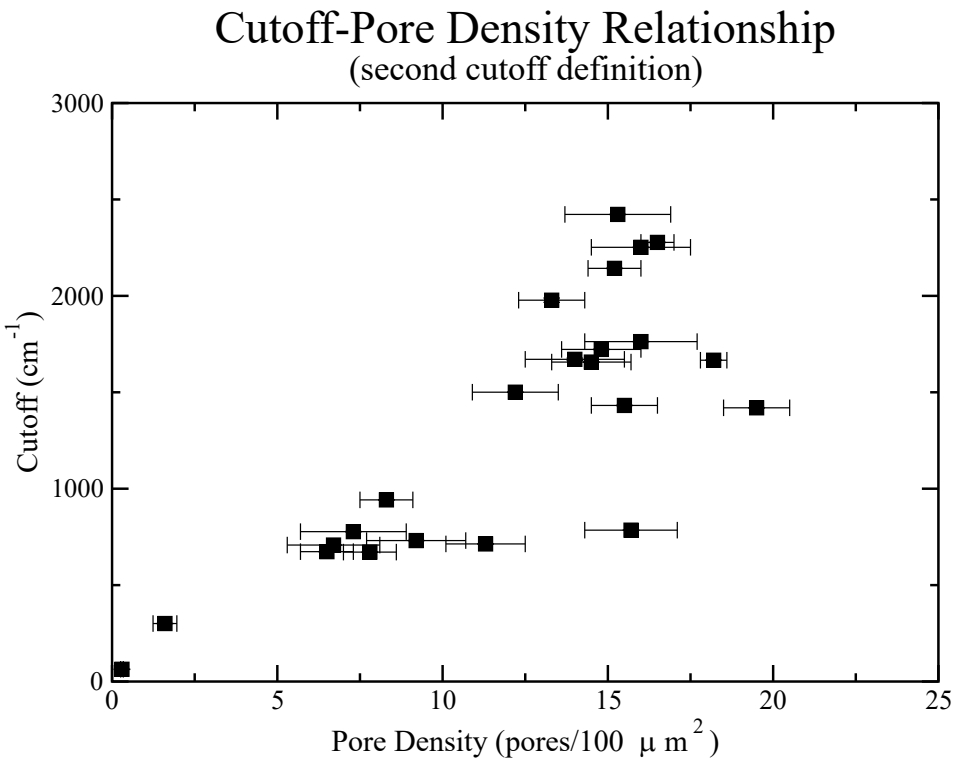

Figure 3.11: Plot of the relationship between pore number density and cutoff wavenumber using the second cutoff definition.

these plots, it is clear that there is no major deviation from the trends observed with the initial definition of the cutoff; there is a possible trend linking the cutoff and the pore number density whereas there appears to be no obvious correlation between the cutoff and the pore coverage.

As before, it can be seen in Figure 3.13 that the cutoff and the pore radius are not linked with the exception of the case of the C-Type samples. The results of previous measurements [50] are once again included to provide further evidence for this claim. Figure 3.14 shows that the relationship between the NND and the cutoff wavelength is also identical to as discussed previously.

From these results along with the results presented in Figures 3.11 and 3.12, it can be seen that the choice of cutoff definition does not significantly affect the trend between the optical and topological properties analyzed in this thesis. As such, it can be said that these trends are not simply an effect of selectively choosing a certain cutoff definition but are indeed a real property exhibited by

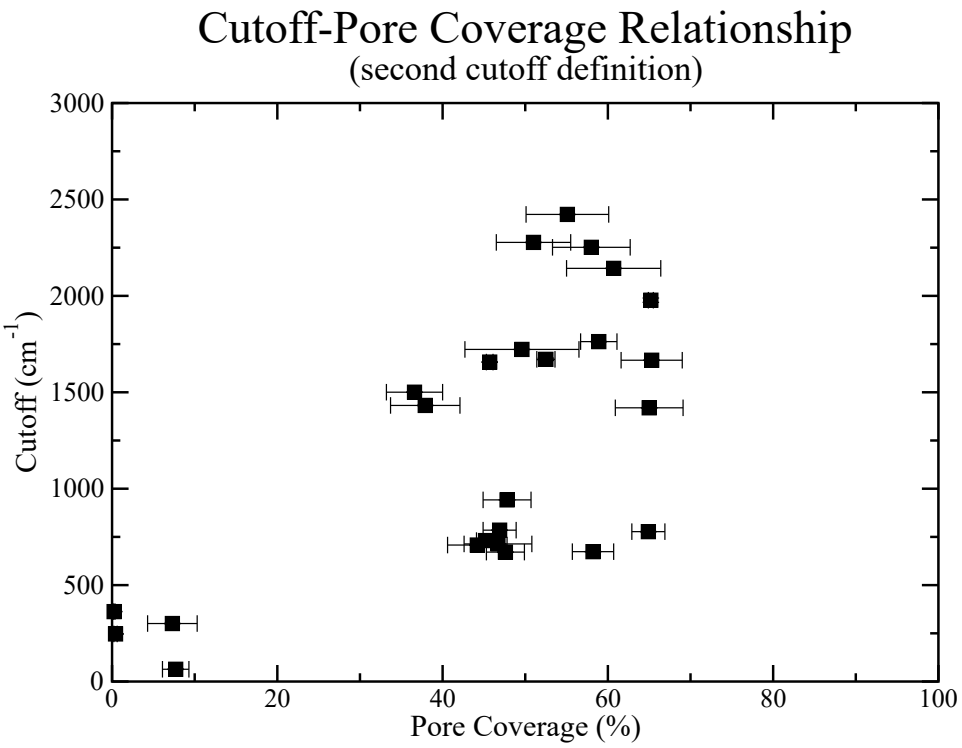

Figure 3.12: Plot of cutoff wavenumber as a function of pore coverage using the second cutoff definition.

the filters.

Lastly, the dependence of the optical cutoff on the pore wall thickness was explored. This was done only for the A- and B-type samples, as the pores on the C-type samples were much more scattered (see images in Appendix A) and it is not reasonable to suggest that there are "walls" separating them. To calculate the average wall thickness, the pore number density n as well as the pore radius r was used. The equation used was:

$$\langle t \rangle = n^{-1/2} - 2r \tag{3.3}$$

This equation gives the minimum average wall thickness, as it simply determines the total average area dedicated to each pore and then subtracts the diameter to determine the remainder of the linear distance for each square unit of area. A plot of the relationship between wall thickness and cutoff wavelength

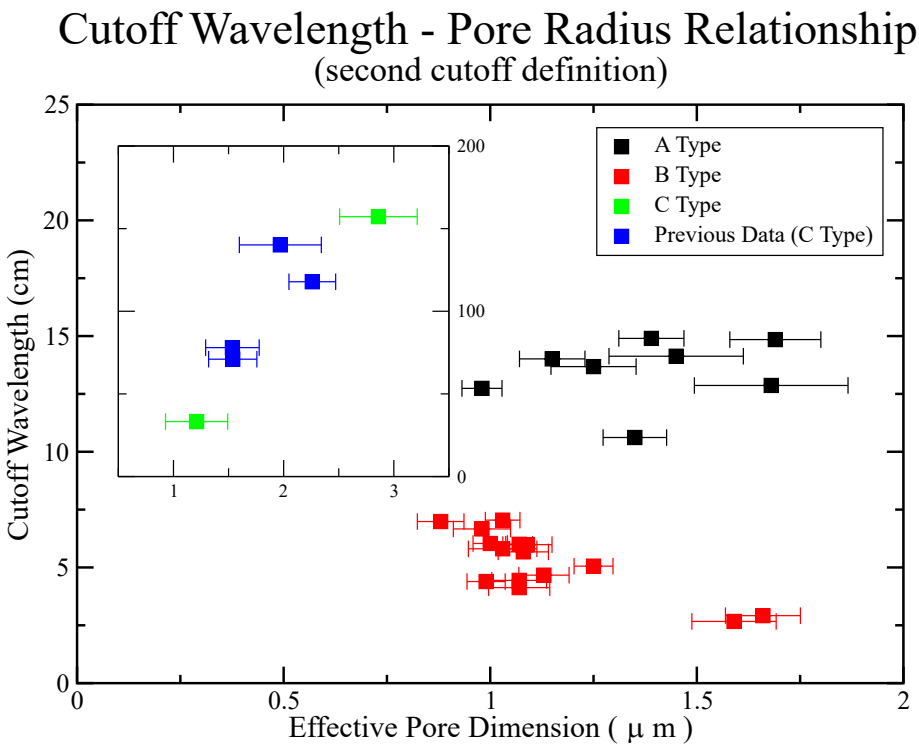

Figure 3.13: Plot of cutoff wavenumber as a function of pore radius using the second cutoff definition. The axes on the inset graph map the same property as do the main graph.

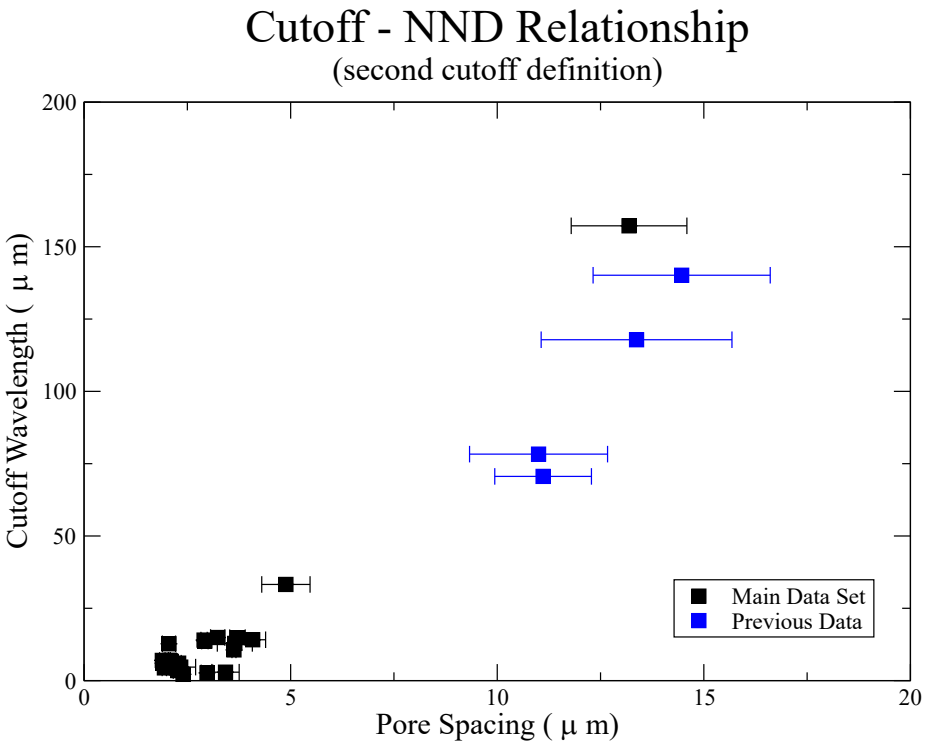

Figure 3.14: Plot of the relationship between NND and cutoff wavelength using the second cutoff definition. To further illustrate the relationship further, results from previous work [50] were included. The axes on the inset graph map the same property as do the main graph. The points for the lower anomalies and the higher outliers were not included.

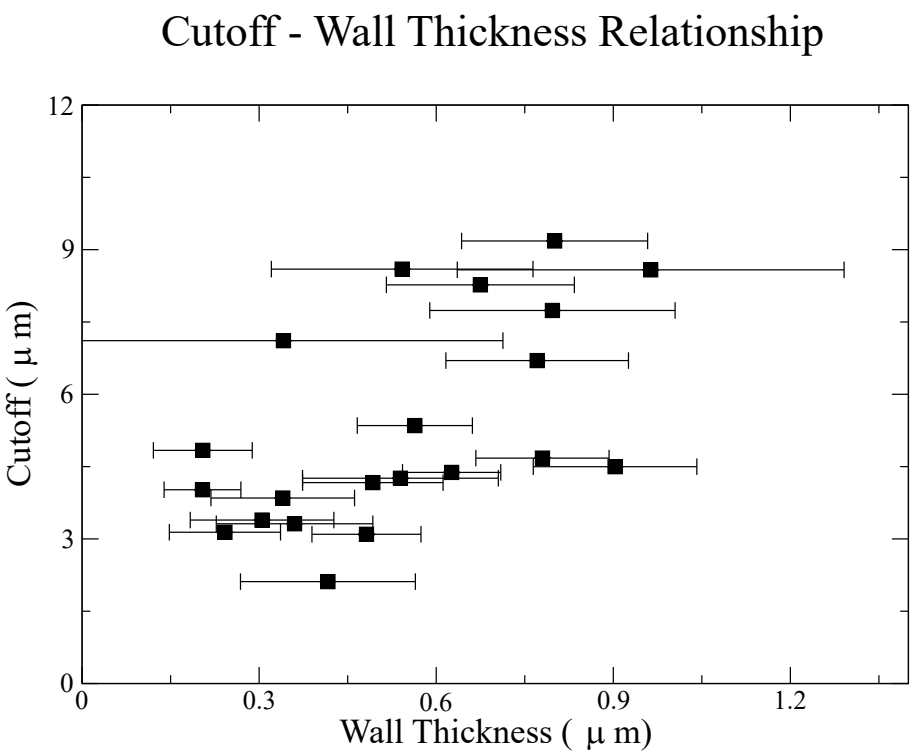

Figure 3.15: Plot of the relationship between pore number density and average minimum wall thickness.

is given in Figure 3.15.

This plot shows that there may indeed be a loose correlation between the wall thickness and the cutoff wavelength. However, the non-uniformity of the surface topology of a given sample causes a wide discrepancy of wall thickness values on a given sample, and as such this relationship cannot be considered conclusive.

Even though all of these trends exist, it should be noted that the trends are not perfect. This is likely due to the polydispersity of light scattering due to the non-uniformity of pore sizes on a given sample. Sample 27 is an example of a filter which, at a glance[1], appears to have a high degree of non-uniformity in pore sizes. Figure 3.16 gives a histogram of the pore areas as given by ImageJ over the surface of the sample for one of its SEM images.

From this histogram, it can be seen that there is considerable variance in

[1]see Appendix A

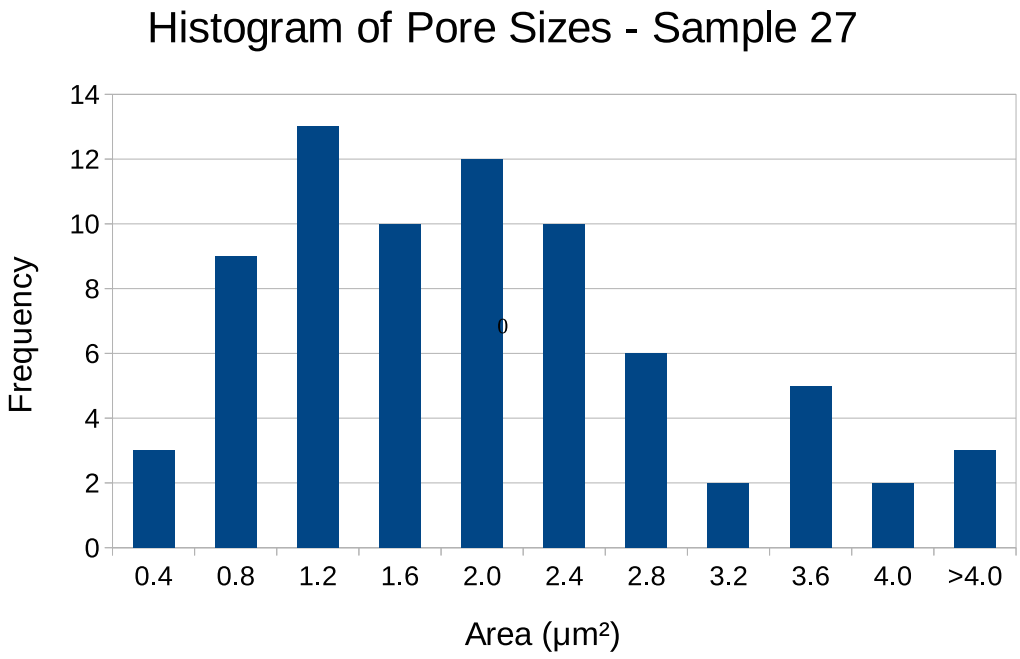

Figure 3.16: Histogram of pore sizes for Sample 27.

pore size even over a relatively small area. Since the scattering of light is known to be dependent on the size of scattering centres, it is likely that the polydispersity of pore sizes causes some variance in the optical cutoff. This, however, is not necessarily a negative property; it is shown that in traditional scattering filters that the optical cutoff is sharper for filters with a large distribution of scattering centre sizes [28].

3.2 Temperature-Dependence

The first attempts at performing measurements of the cutoff wavenumber dependence on temperature were unsuccessful. This was due to the use of the Wakefield Thermal Paste as a thermally conductive adhesive as previously mentioned in Chapter 2. Upon measuring the transmission spectra at lower temperatures, there were some additional absorption features that appeared in the transmission as shown in Figure 3.17.

There are four strong dips in the transmission. These features can be ex-

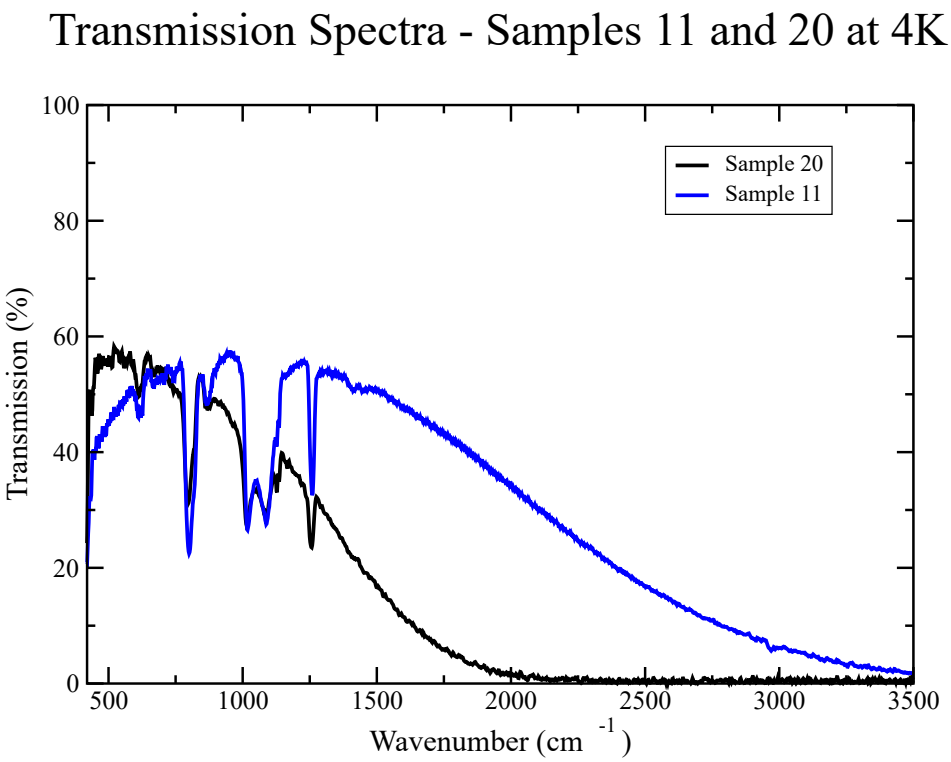

Figure 3.17: Plot showing unexpected strong absorption features at low temperature for Samples 11 and 20.

plained one of two ways. One of these is that the thermal paste causes a reaction with the silicon wafer that causes it to oxidize. The fact that the thermal paste needed to contact the wafer for a significant period of time (due to overnight evacuation of the sample chamber) means that there is plenty of time for such a reaction to take place. The other option is that the degassing of the sample chamber deposited a small amount (i.e. not visible to the naked eye) of the thermal paste onto the surface of the sample. In this situation, the absorption is indicative of the transmissive properties of the paste rather than any silicon oxide on the sample's surface. In addition to these features, subsequent room temperature analysis of samples that had been contacted by the thermal paste seemed to show a significant blue-shift in optical cutoff wavenumber.

The absorption features were numbered 1-4 from left to right and their positions for the two example spectra of Figure 3.17 are given in Table 3.3.

From this table, it can be seen that the four positions of the features are

Table 3.3: Positions of the absorption features A_n for two example low-temperature transmission spectra affected by Wakefield Thermal Compound.

Sample	A_1 (cm^{-1})	A_2 (cm^{-1})	A_3 (cm^{-1})	A_4 (cm^{-1})
11	800.3	1018.2	1087.7	1259.3
20	796.5	1014.4	1081.9	1257.4

consistent between the two samples, which in turn confirms the hypothesis that there is a common cause. At a glance, it does seem that Peak 1 could be explained by O_nSiH_x deformation and that Peaks 2 and 3 may be explainable by $Si-O-Si$ stretching as described in Chapter 1. However, the known FTIR data for oxidized porous silicon does not have any explanation for Peak 4. Because this is a very prominent peak, it is unlikely that this is a feature that has been previously overlooked. Thus, it is highly probable that the cause of these features in the affected spectra is due to the deposition of a very thin layer of the thermal paste (a mixture of zinc oxide and silicone oil) onto the surface of the sample during chamber evacuation.

The Wakefield Thermal Paste was then replaced by GE varnish. The use of this adhesive did not cause any unexpected features to appear in the transmission spectra. Figures D.1-D.7 and Tables D.1-D.7 of Appendix D contain the transmission spectra and temperature dependence of the optical cutoff values for the seven samples (Samples 2, 4, 6, 14, 19, 20 and 21). The data set in each of these tables is plotted on the same set of axes in Figure 3.18. From this graph, one can see that the optical cutoff does not depend strongly on temperature.

Figures 3.19, 3.20, and 3.21 show the data over smaller ranges of wavenumbers. In all three of these plots, it can be seen that the cutoff values are the same (within error bars of some samples) at temperatures up to 100 K for all seven samples. Above this temperature, however, the cutoff values showed temperature variation. Samples 6 and 14 experienced an increase in cutoff above 100 K, Samples 4, 20, and 21 experienced a decrease in cutoff above 100 K, and Samples 2 and 19 remained relatively constant above 100 K. This variation

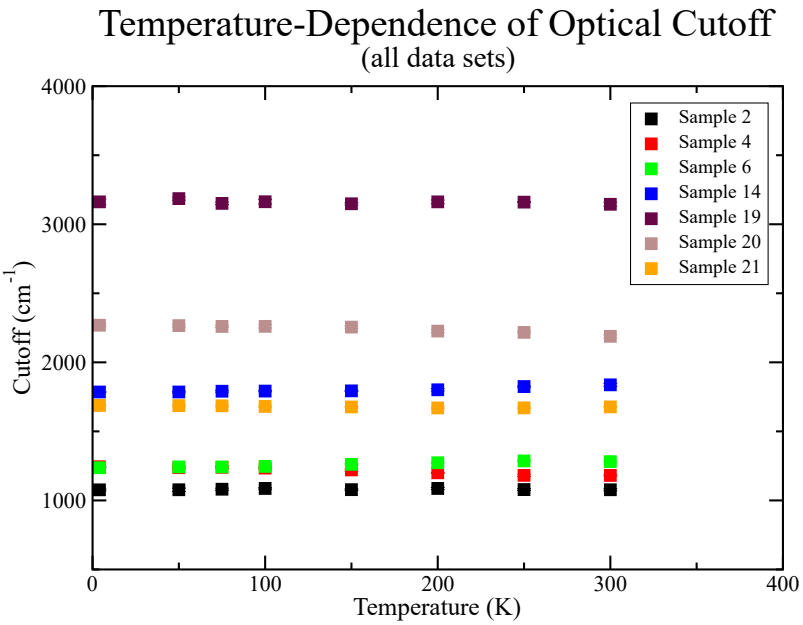

Figure 3.18: Plot of the dependence of cutoff wavenumber on temperature for the seven samples analyzed.

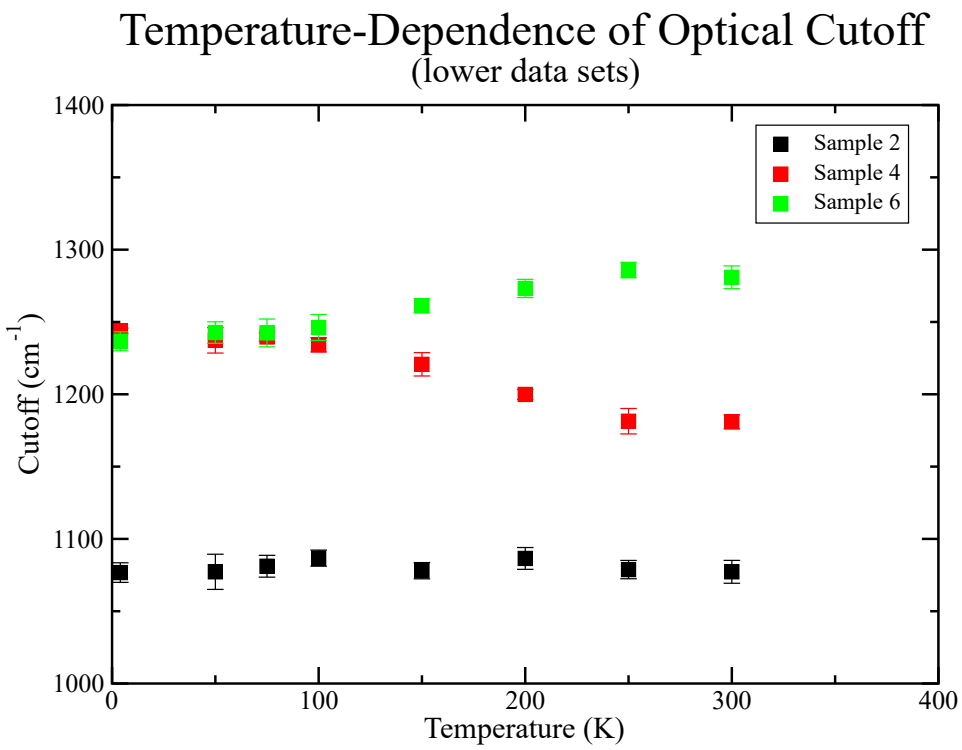

Figure 3.19: Plot of the dependence of cutoff wavenumber on temperature for the lower cutoff samples.

in trend was unexpected; there did not appear any common cause in terms of sample type, large scale properties of the porous structure, or even etching conditions that could explain this result.

It was at this juncture at which the position-dependent measurements of the optical cutoff were taken. Initially, some non-specific measurements of different locations on a series of samples were taken as to determine whether or not the optical cutoff was consistent across the entire surface of the sample. The locations were not marked so as to not damage the surface of the sample. The results of these basic measurements are given in Table 3.4.

From these measurements, it was confirmed that there is some spatial dependence on the optical cutoff of a given sample. This was investigated further using Sample 8 as outlined in Chapter 2. The results of the cutoff values and pore densities for the three spots analyzed are given in Table 3.5. From this table, it can be seen that higher cutoff values correspond to higher pore number

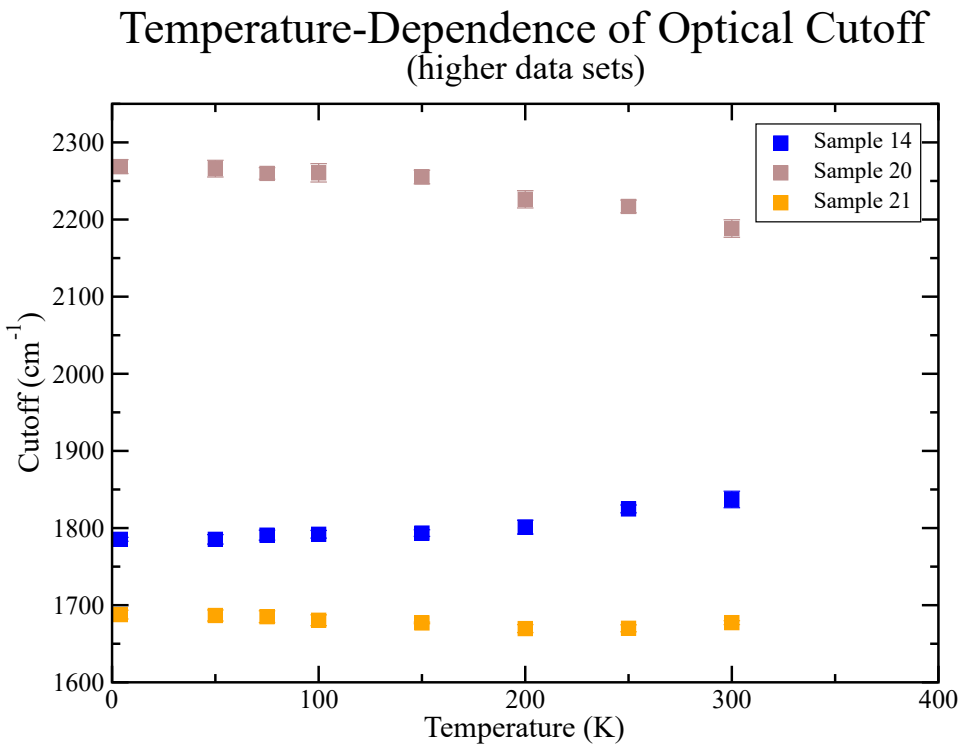

Figure 3.20: Plot of the dependence of cutoff wavenumber on temperature for the higher cutoff samples.

Table 3.4: Results of basic position-dependent cutoff measurements.

Sample	Spot 1 Cutoff (cm^{-1})	Spot 2 Cutoff (cm^{-1})	Spot 3 Cutoff (cm^{-1})
2	1093.5	1195.1	1097.4
3	1095.4	1188.0	1216.9
5	1417.5	2169.7	2204.4
10	2279.6	2331.7	2504.7
15	2225.6	2234.6	1866.9
17	2353.6	2260.4	2217.9

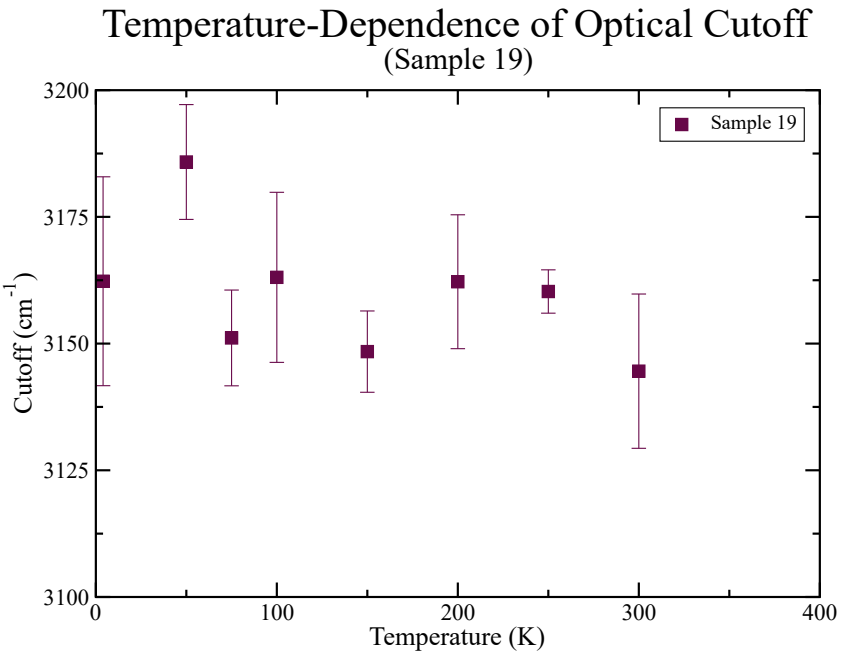

Figure 3.21: Plot of the dependence of cutoff wavenumber on temperature for Sample 19.

Table 3.5: Results of the position-dependent optical and topological measurements on Sample 8.

Position	Cutoff (cm^{-1})	Pore Number Density (pores/100μm^2)
Low	1161.6	11.0
Middle	1314.0	11.8
High	1236.2	11.2

density values consistent with the conclusions of Section 3.1. It is notable that the data points in Table 3.5 fit into the trend exhibited by the data displayed in Figure 3.8. Figure 3.22 gives the optical spectra along with SEM images for the different surface locations analyzed on Sample 8.

From these position-based measurements, it is clear that samples are not uniformly etched. Because the method used to determine the temperature-dependent optical properties required underfilling of the sample with light, it was possible that the spot could move slightly on the sample without moving off of the sample entirely.

The illuminated location moves because the copper sample holder contracts when the temperature is reduced to 4 K. Then, as the temperature is increased for each new measurement, the copper holder changes in size which slightly alters the position of illumination on the sample. As such, the inconsistent deviations of the optical cutoff above 100 K are likely due to a combination of two factors: the inconsistency of the cutoff over the surface of the sample and the thermal expansion of the copper sample holder with increasing temperature.

Figure 3.23 gives the relative thermal expansivity of copper as a function of temperature [51]. From this, it can be seen that there is comparatively little change in the size of a copper sample for temperatures lower than 100 K. Thus the temperature-dependent optical measurements up to 100 K are reliable due to the sample maintaining a consistent position. As such, it can be concluded that the optical cutoff has virtually no temperature-dependence for temperatures below 100 K. This is evidenced by the data given in Figures 3.19-3.21.

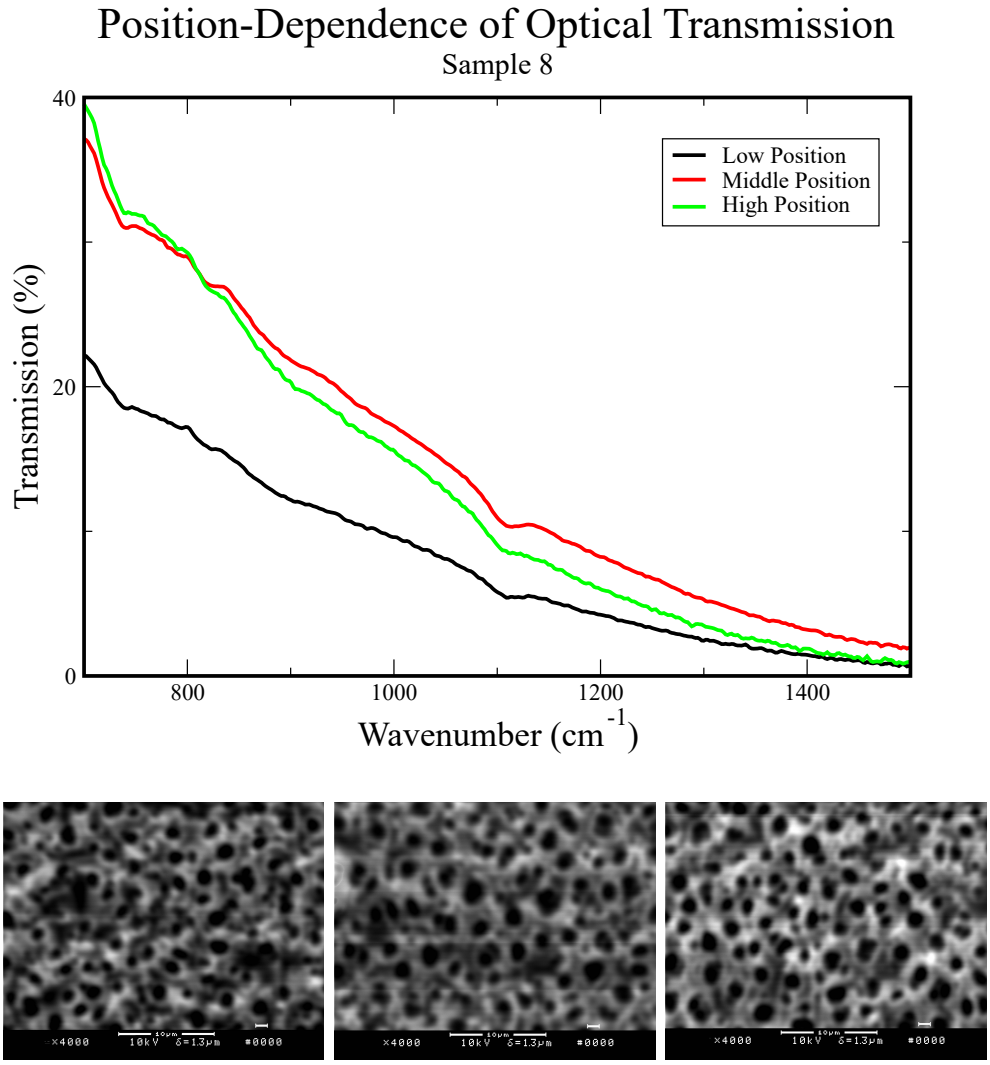

Figure 3.22: Position-dependence on the transmission spectrum for Sample 8. The SEM images at the bottom are the images for the three positions analyzed. From left to right these are: Low Position, Middle Position, and High Position. All images were taken at 4000X magnification.

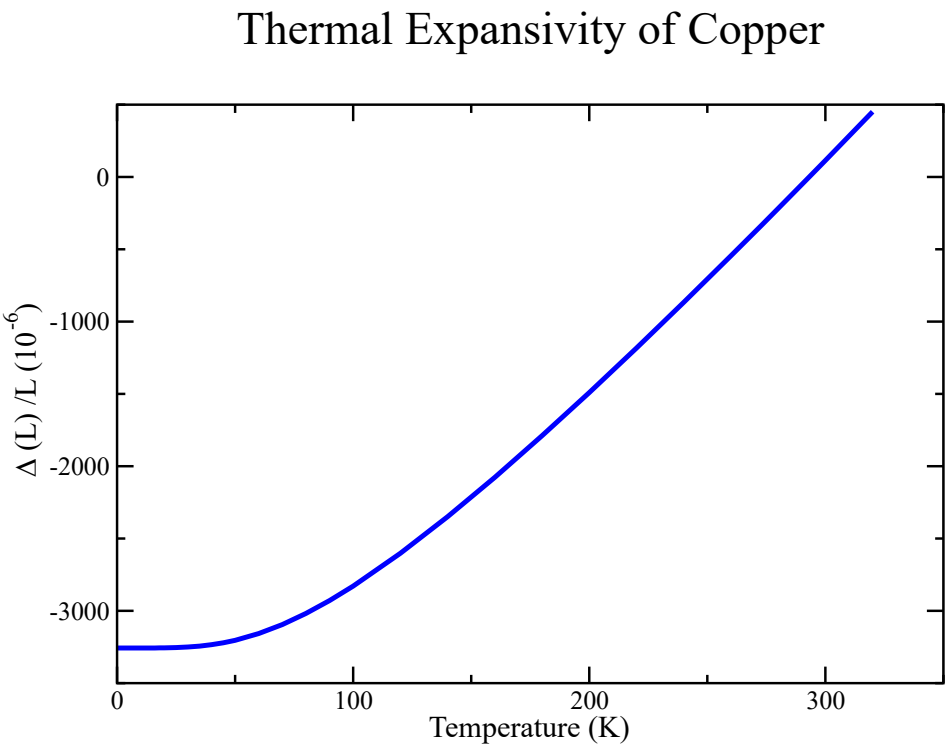

Figure 3.23: Thermal Expansivity of Copper. L is the length of the copper at 293.15 K and Δ(L) is the change in length between the temperature in question and the length at 293.15 K. Data is from [51].

Chapter 4

Conclusions

4.1 Discussion

The main conclusion from this work is that there is indeed a displayed trend connecting pore number density and optical cutoff wavenumber. In general, it was found that samples with a larger pore number density had a higher (i.e. further into the infrared regime) cutoff wavenumber. Pore coverage, however, had no predictable effect on the cutoff as long as it did not become too high nor too low. For the pore coverage values at either extreme, it was found that the cutoff value did not follow the same trend with respect to pore number density as did the other samples. The higher outliers did not follow the trend due to the collapse of pore walls and the fact that the surface acted more as a rough surface of a silicon wafer rather than as a series of scattering centers. The lower outliers did not follow the trend due to the fact that there appeared to be a vast amount of space between pores. This space caused areas of the filter to simply act as polished silicon rather than as a porous surface. Furthermore, it was determined that the average linear dimension of the pores also did not relate predictably to the optical cutoff.

Because the pore number density of a given sample is adjustable by changing the etching parameters (specifically by adjusting etching current, HF concen-

tration, and doping concentration as outlined in Section 1.1), it should follow that the cutoff of a sample is also adjustable. The advantages of porous silicon filters over more traditional infrared filters in combination with the fact that such filters are not limited to a narrow scope of cutoff values is advantageous for use in low-temperature applications.

The low-doped (1 0 0) samples showed some unusual results. Unlike for the other sample types, the etching procedure, when performed on the C-Type samples, produced pores that had a significant amount of spacing between them. Furthermore, these pores tended to be have a different morphology; the C-Type samples produced "cross-shaped" pores whereas the other types produced much more circular pores. Despite the great spacing between pores, however, these samples provided low optical cutoff values. As such, it is these samples which would be of the most interest when manufacturing filters for the very far infrared range.

In order to determine the exact effects of the etching parameters on the pore number density of a given sample, a more reliable electrochemical cell would need to be used. The cell utilized in the experiments discussed in this work used a copper plate that had a tendency to degrade with time and form a layer of unknown deposit on its surface. Though this deposit could easily be removed through the use of hydrochloric acid, it is possible that the use of this acid also damaged the plate itself. This would explain the fact that some samples that underwent identical etching conditions (for example, Samples 1 and 3) did not provide identical results.

An alternative to electrochemical etching that has been to shown to create a similar porous structure is the use of laser-etching [52]. Though this method may be more expensive than anodization, it may also provide more controllable and reliable porous structure. This would ensure that the pores are both of the correct density and that this density is consistent across the surface. This consistency would allow for the characterization of porous silicon samples at

low temperature.

The correlation between the pore number density and the optical cutoff implies that the scattering mechanism governing the optical properties of porous silicon is a result of the spacing between the pores. Analysis of the nearest-neighbour distance (NND) between pores confirmed this. As the NND was increased the cutoff wavelength also increased.

This result coincides with what has been observed elsewhere. It has been proposed [27] and later experimentally observed that random arrays of macropores in silicon scatter light at wavelengths which are below the average interpore spacing [26]. In general, the pore number density is directly related to the average pore-to-pore distance (by the relationship NND = $d^{-1/2}$ as mentioned in Chapter 3). Because of this, the resulting trend of a higher pore number density resulting in a lower cutoff wavelength coincides with that which has already been observed. It should be noted, however, that the results displayed in Figure 3.9 suggest that there are some wavelengths that are greater than (but on the same order of magnitude as) the pore-to-pore distance which are passed through the filter and not scattered away.

The average effective linear dimension for the pores on a given sample was also estimated using the pore number density and pore coverage measurements. Though there did not seem to be a correlation between the pore dimension and the cutoff for the majority of the samples; it was found that there was a correlation between the cutoff wavelength and the effective pore dimension for the low-doped (1 0 0) C-Type samples. Since the C-Type samples have a much greater pore spacing than do the other types, it is possible that this trend is a result of the considerable amount of space between pores on the surface of these filters. In this case, the filters are acting exactly like traditional scattering-based filters; the size of the scattering centres (e.g. diamond dust) is the parameter which dictates the cutoff [28]. Traditional scattering-type filters for the far-infrared range do have a large amount of space between scattering

particles [28]; thus implying that the C-Type samples operate by a similar scattering mechanism.

It also should be noted that there is some polydispersity in pore sizes for a given sample. Because the scattering of light should be dependent on the surface geometry of a given sample [27], it is highly likely that this non-uniformity in pore size has an effect on the cutoff position as well as its sharpness.

Another important result determined from these experiments is the fact that there is not any significant temperature-dependence of the optical cutoff for temperatures below 100 K. The nature of the measurements performed did not allow for reliable analysis for temperatures higher than this value. This implies that the characterization of porous silicon filters is not necessary for temperatures below this value; determining the optical cutoff at 100 K should be sufficient to determine the cutoff to within 10 cm^{-1} for temperatures up to and including this value. This ensures that any temperature-based characterization of porous silicon filters can be performed using liquid nitrogen rather than the more expensive liquid helium whose cost has been consistently increasing in recent years [53].

Though it was shown that there is no temperature-dependence of the optical cutoff up to 100 K, it cannot be reliably predicted that this would hold true for higher temperatures. Temperature-dependence of the cutoff could be caused by thermal expansion or contraction of the sample itself. The resulting change in linear dimension could cause the number of scattering centers per area to change which, in turn as predicted by the correlation between pore number density and optical cutoff established at room temperature, would cause the cutoff value to change.

In Figure 4.1 it can be seen that silicon begins to undergo significant thermal expansion for temperatures greater than 100 K. Because of this, it is possible that, for higher temperatures, the cutoff will have a temperature-dependence. Furthermore, if thermal expansion of silicon does affect the cutoff value, it would

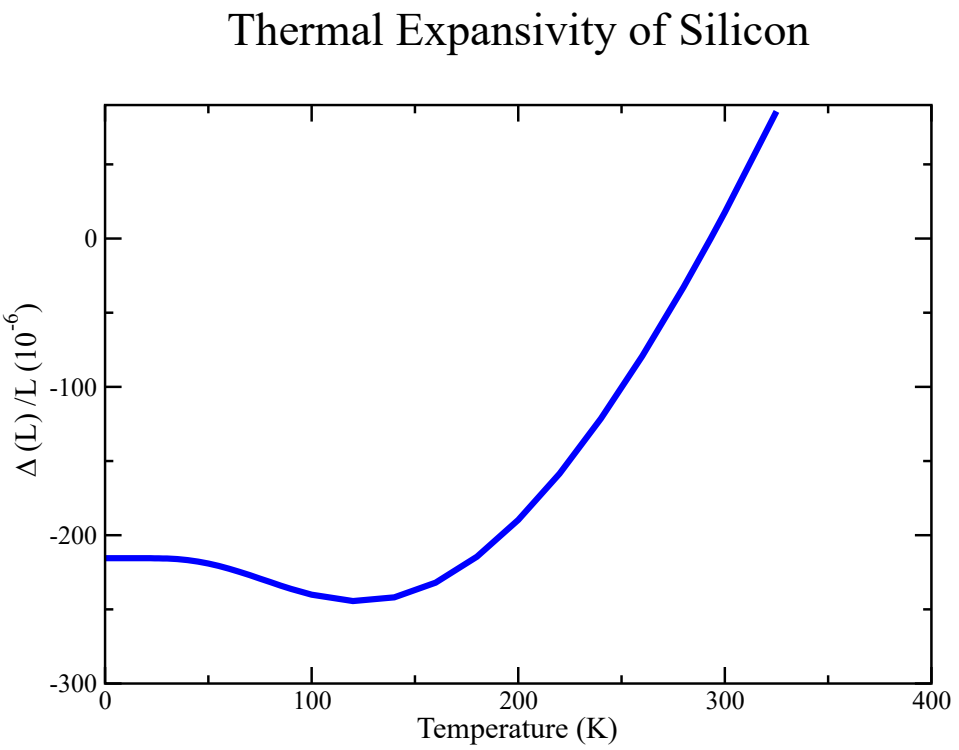

Figure 4.1: Thermal Expansivity of Silicon. L is the length of the silicon at 293.15 K and Δ(L) is the change in length between the temperature in question and the length at 293.15 K. Data is from [54].

not have affected significantly the regime in which the measurements described in Chapter 3 can be considered reliable. Further measurements using a method differing from that used here would be required to determine the significance of this dependence.

4.2 Future Work

The most obvious extension of this research on porous silicon filters that could be performed is a further investigation of the temperature-dependence of the optical cutoff. To determine the temperature-dependence of the cutoff for temperatures greater than 100 K, it is clear that the current method cannot be used. A similar setup, however, may still be useful.

A possible method by which only minor modifications to the current appa-

ratus would be necessary. For both methods, a laser that can be switched on and off must be set up in such a way that it follows a path along that followed by the light from the Globar source. Using this laser, it would be possible to ensure that the infrared beam strikes the exact same position on the sample for each temperature. This would ensure that any differences observed in the spectral transmission are indeed due to changing temperature rather than changing location on the surface. There does, however, need to be a means by which the laser calibration location can be identified for each measurement. One way is to simply mark the location with, for example, a permanent marker similar to how it was done for the measurements that indicated spatial dependence.

If the infrared beam were small enough one could selectively etch several smaller portions of the sample. The advantage of this is that it could allow for a single sample to be etched in multiple different ways on different areas of the sample. Though this may not be useful for any practical applications, it does allow for experimental analysis to occur on the same sample for different etching parameters. This has the potential to save resources and allow for more etching parameters to be analyzed using the same number of virgin silicon wafers. In Figures 2.5 and 2.6 respectively, an image of both an unetched and an etched sample were given. From these images, it can be seen that there is a significant difference in appearance between etched and unetched samples. As such, the various etched areas could be easily identified. To selectively etch the sample, one of two methods can be used. One is to completely redesign the electrochemical cell such that the hole at the bottom of the well is smaller (i.e. leaving a smaller area of the sample exposed to the hydrofluoric acid). The other is to mask the sample using a mask that is chemically resistant to the acid that would allow for a smaller area to be exposed to the acid.

Another aspect of porous silicon that could be explored is the exact effect of the etching parameters on the formation of the porous scattering centers. In order to do this, an etching cell of higher quality would need to be used. An

example of such a cell is a “double cell” as described in [55]. These cells allow for the removal of the ohmic contact on the backside of the wafer and replace it with an electrolytic contact [55]. This would remove any effect of the degrading copper plate from the etching process.

Using such a cell, the etching parameters could be systematically adjusted and it would therefore be possible to determine the exact effect of each parameter on the pore number density (and possibly other parameters) of a given sample.

Appendix A

Spectra and SEM Images

This appendix includes the optical transmission spectra and SEM images for the samples used in this project. Unless otherwise indicated, all SEM images included here were taken at 4000x magnification. The bar centered at the bottom of each image scales to an equivalent length of 10 μm.

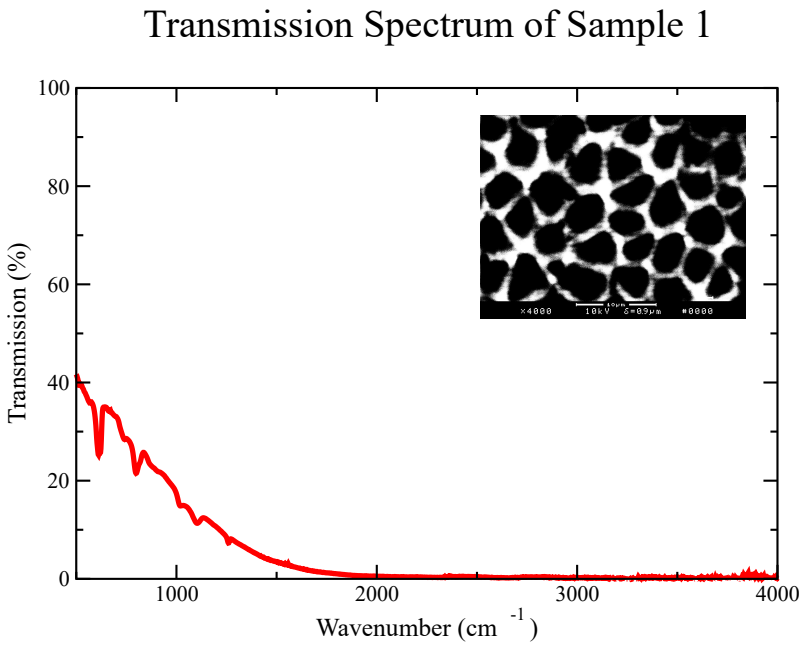

Figure A.1: Transmission Spectrum for Sample 1. Inset is the corresponding SEM image.

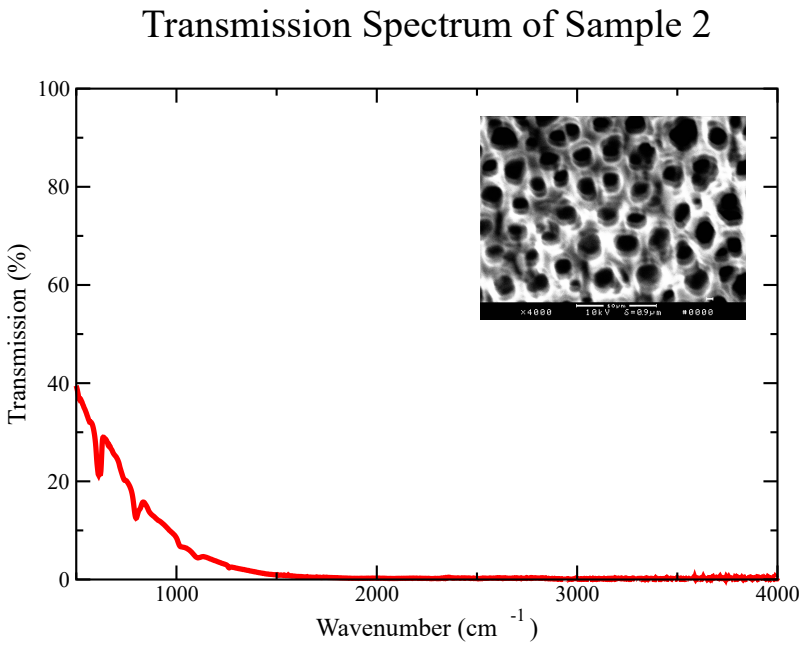

Figure A.2: Transmission Spectrum for Sample 2. Inset is the corresponding SEM image.

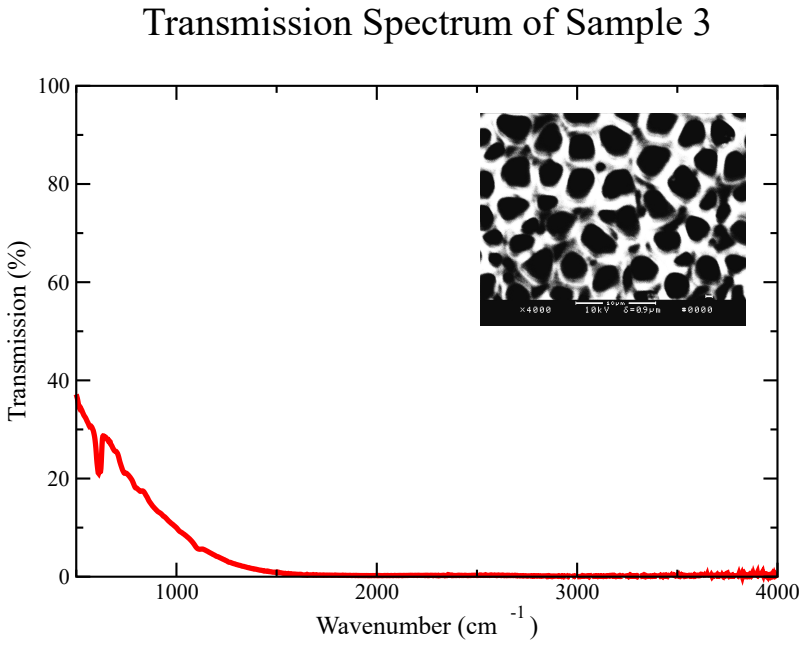

Figure A.3: Transmission Spectrum for Sample 3. Inset is the corresponding SEM image.

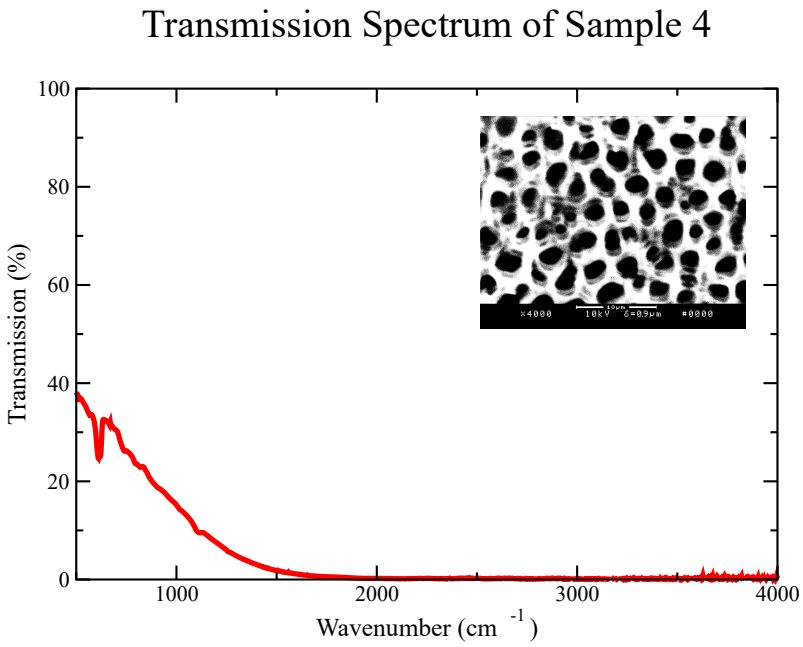

Figure A.4: Transmission Spectrum for Sample 4. Inset is the corresponding SEM image.

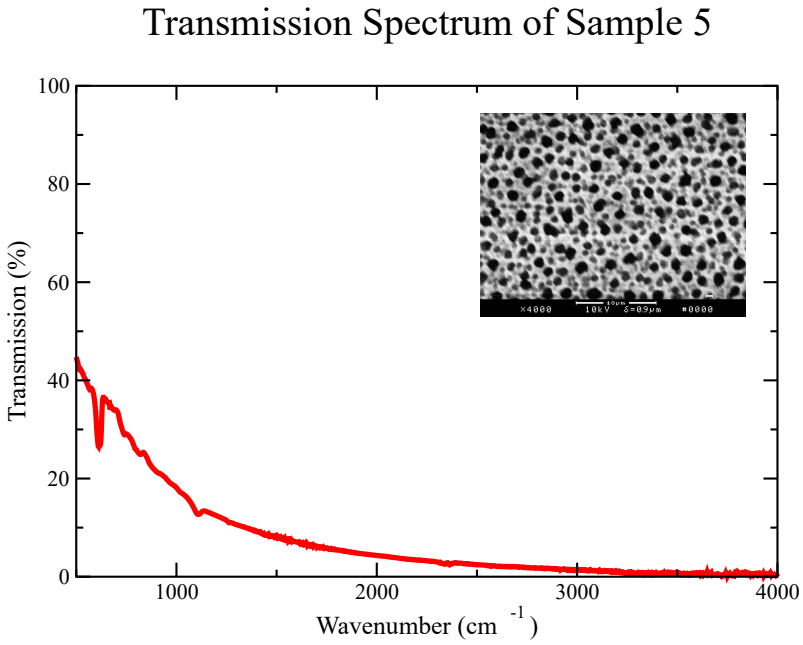

Figure A.5: Transmission Spectrum for Sample 5. Inset is the corresponding SEM image.

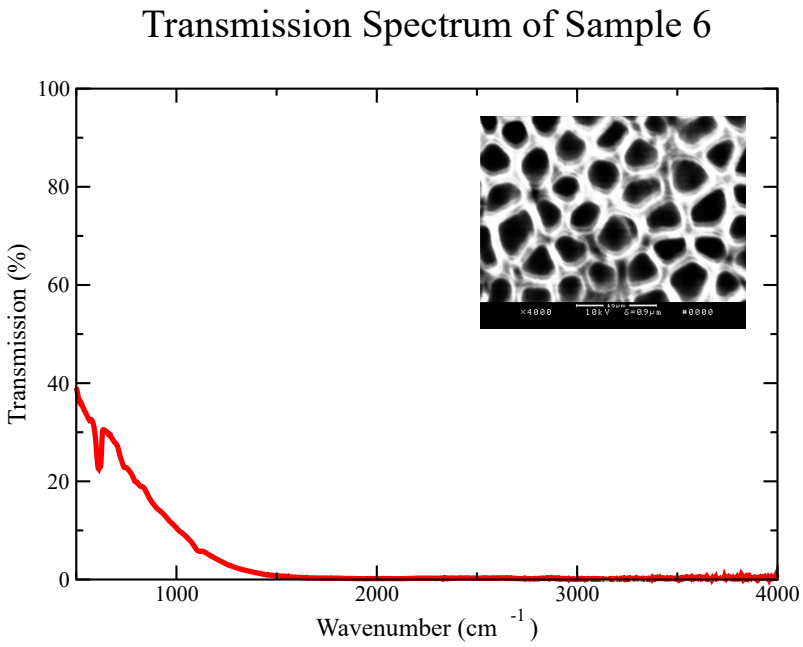

Figure A.6: Transmission Spectrum for Sample 6. Inset is the corresponding SEM image.

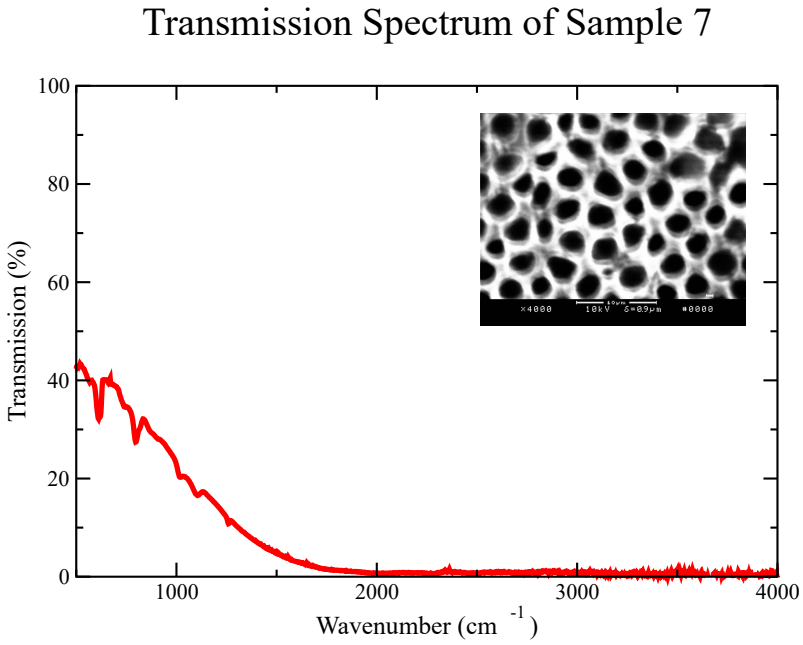

Figure A.7: Transmission Spectrum for Sample 7. Inset is the corresponding SEM image.

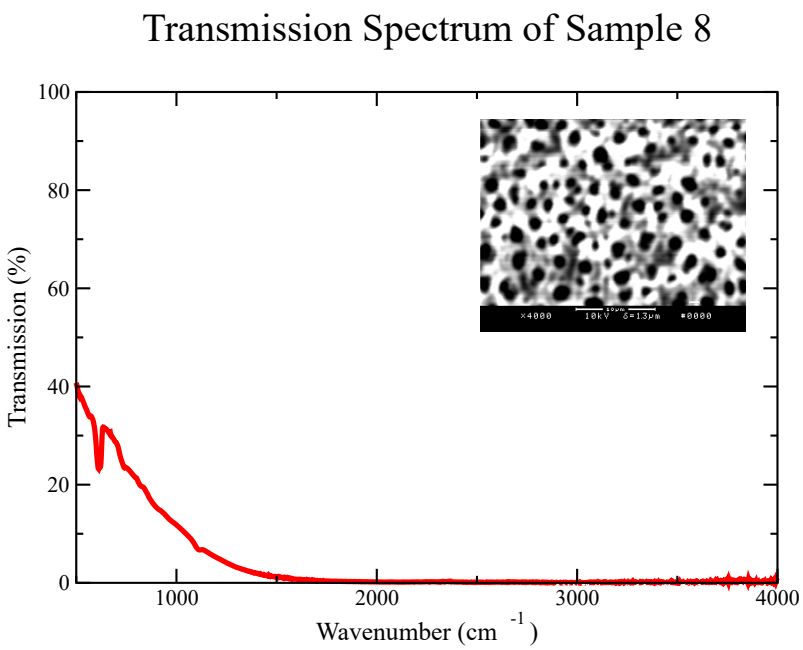

Figure A.8: Transmission Spectrum for Sample 8. Inset is the corresponding SEM image.

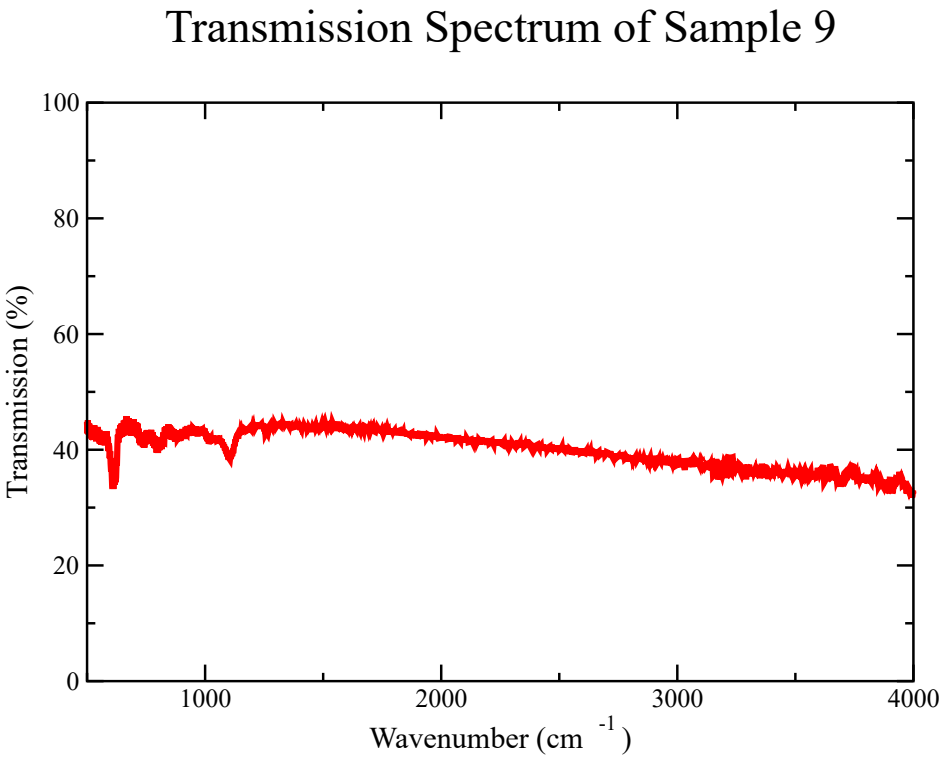

Figure A.9: Transmission Spectrum for Sample 9.

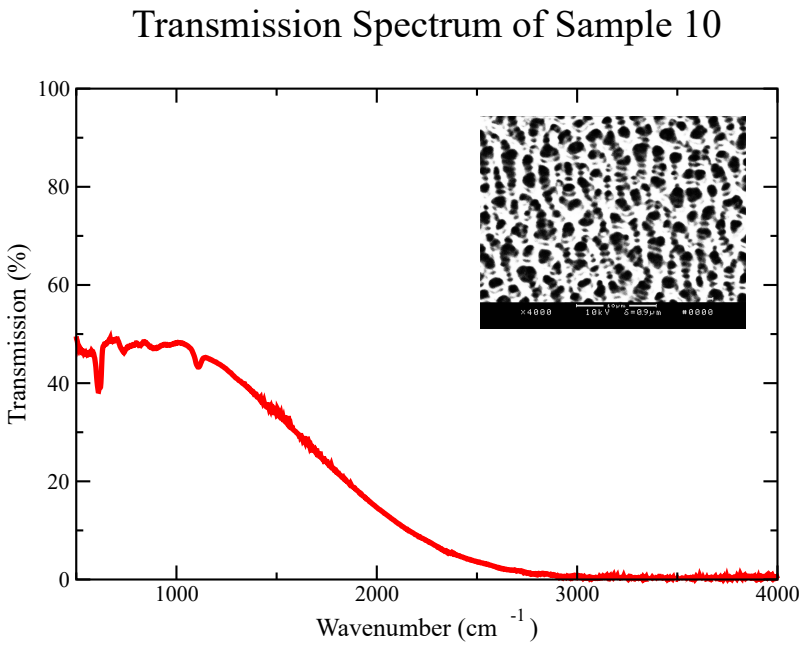

Figure A.10: Transmission Spectrum for Sample 10. Inset is the corresponding SEM image.

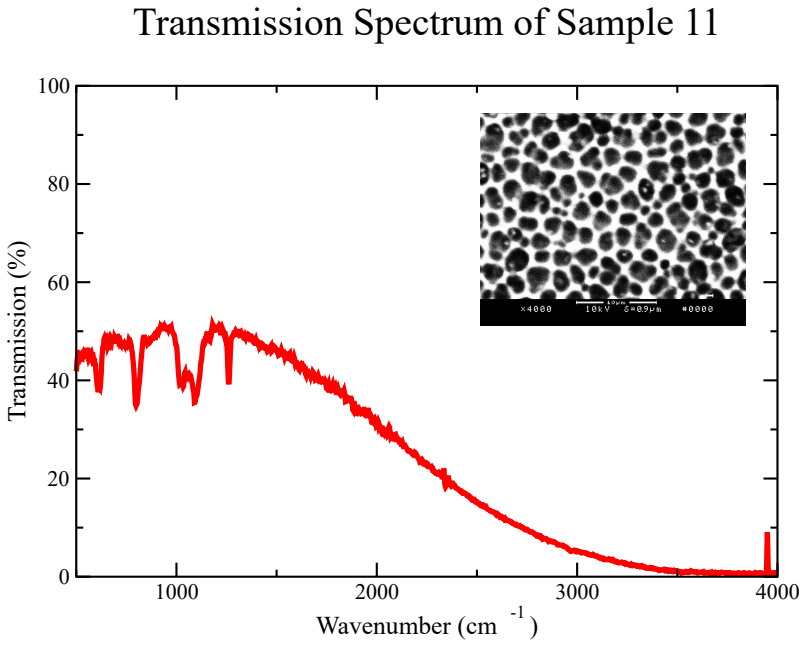

Figure A.11: Transmission Spectrum for Sample 11. Inset is the corresponding SEM image.

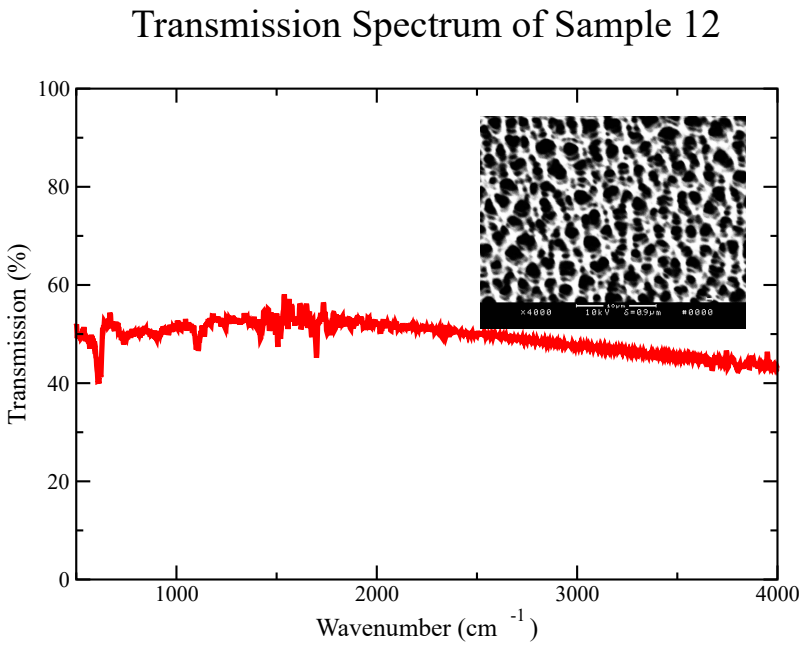

Figure A.12: Transmission Spectrum for Sample 12. Inset is the corresponding SEM image.

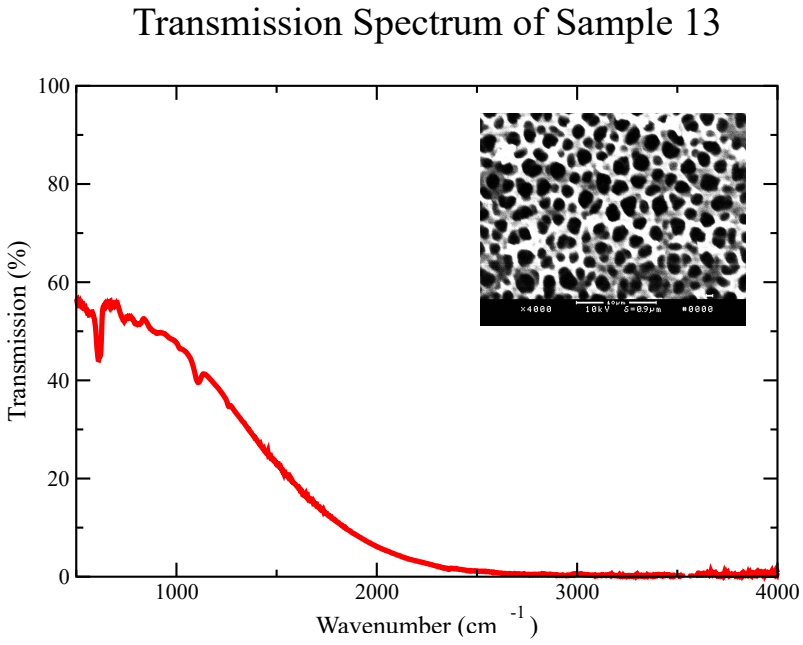

Figure A.13: Transmission Spectrum for Sample 13. Inset is the corresponding SEM image.

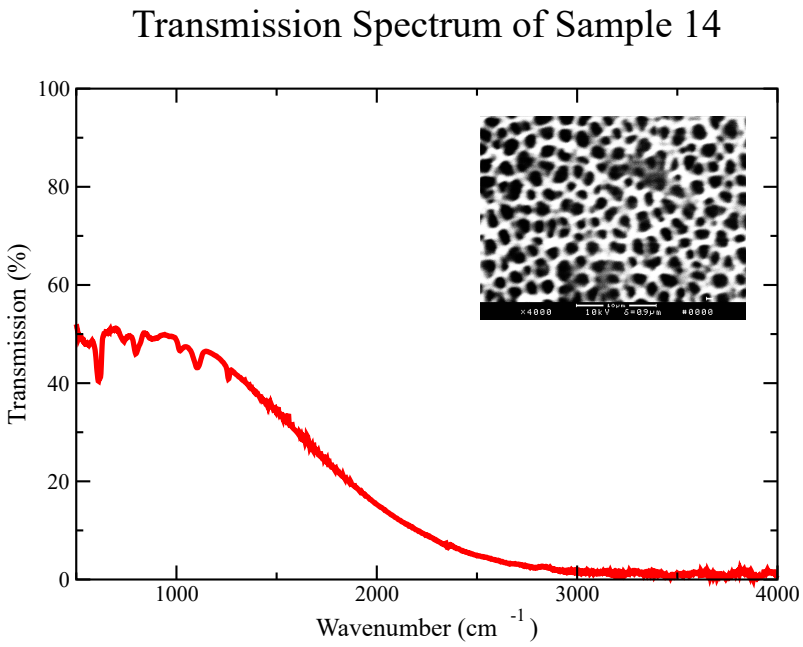

Figure A.14: Transmission Spectrum for Sample 14. Inset is the corresponding SEM image.

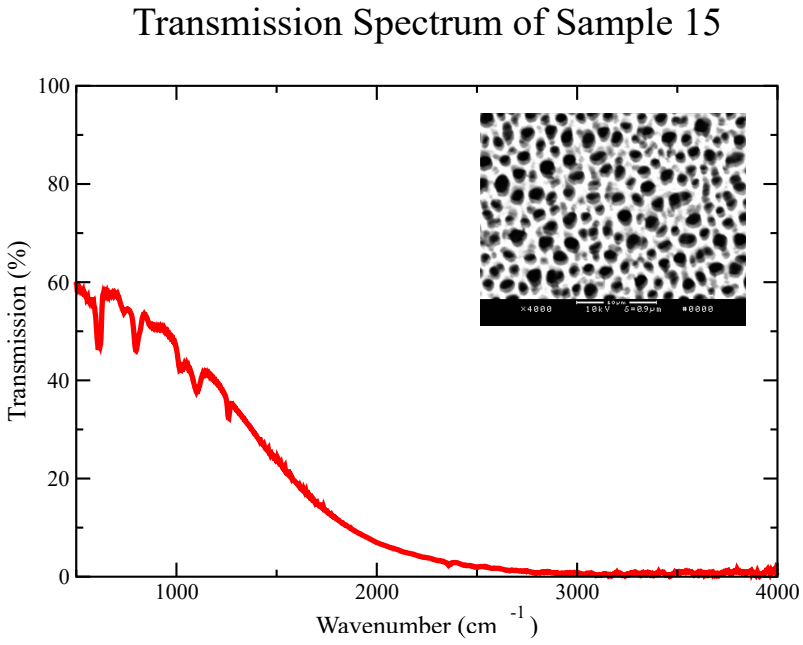

Figure A.15: Transmission Spectrum for Sample 15. Inset is the corresponding SEM image.

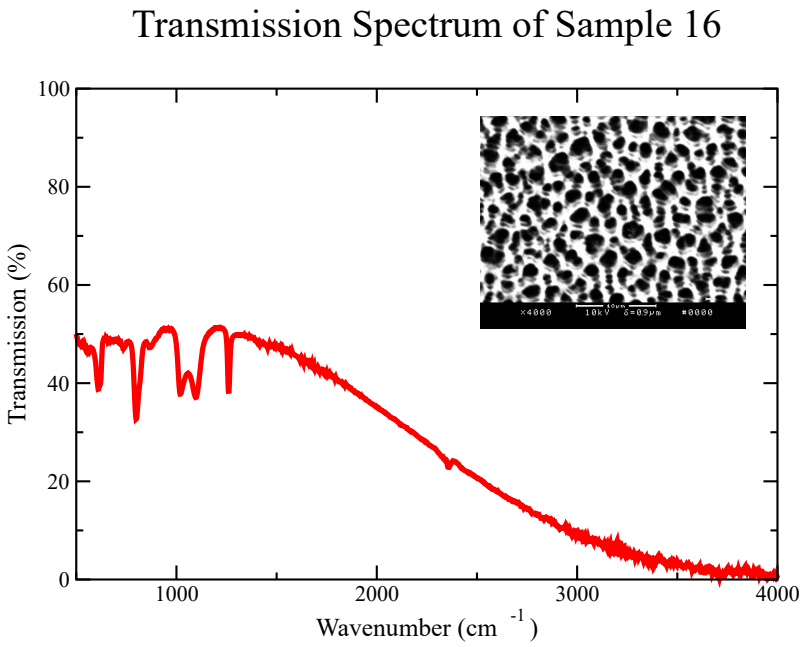

Figure A.16: Transmission Spectrum for Sample 16. Inset is the corresponding SEM image.

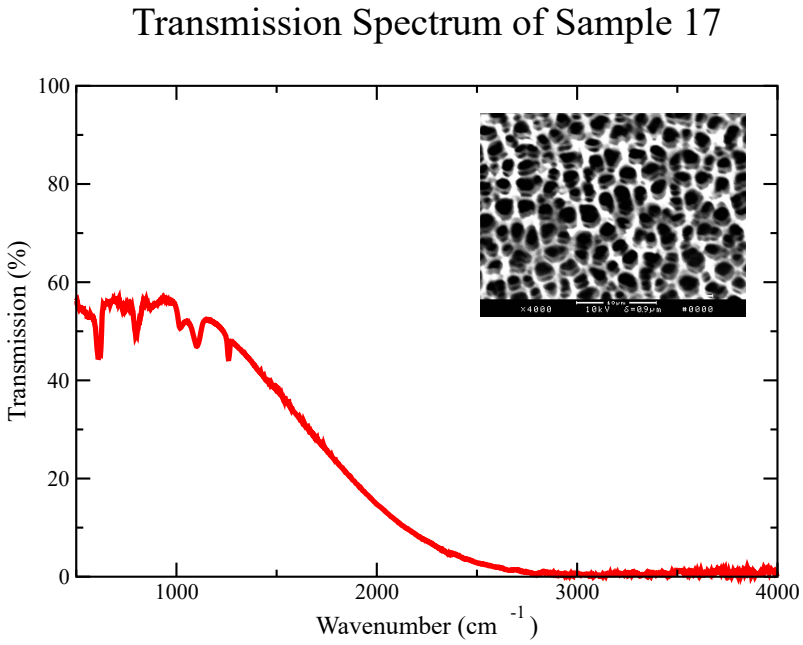

Figure A.17: Transmission Spectrum for Sample 17. Inset is the corresponding SEM image.

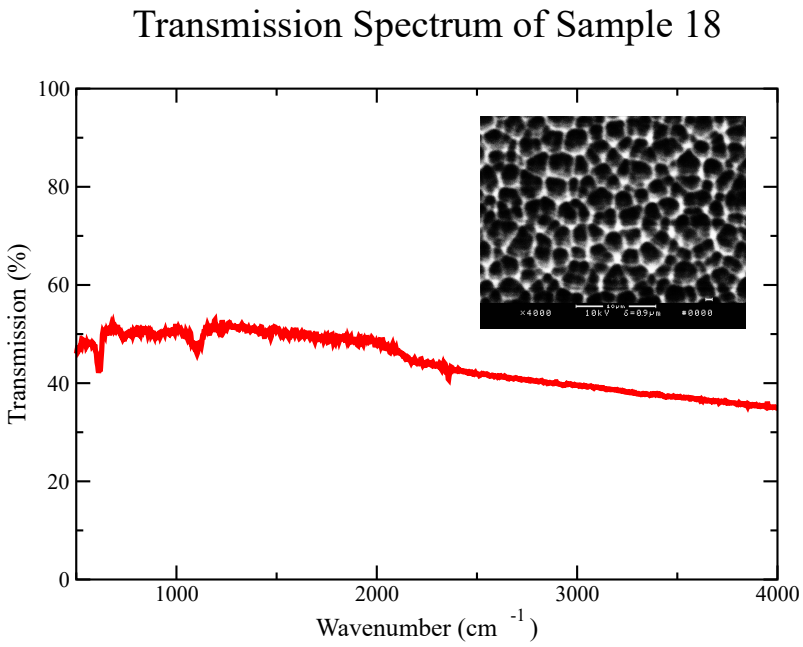

Figure A.18: Transmission Spectrum for Sample 18. Inset is the corresponding SEM image.

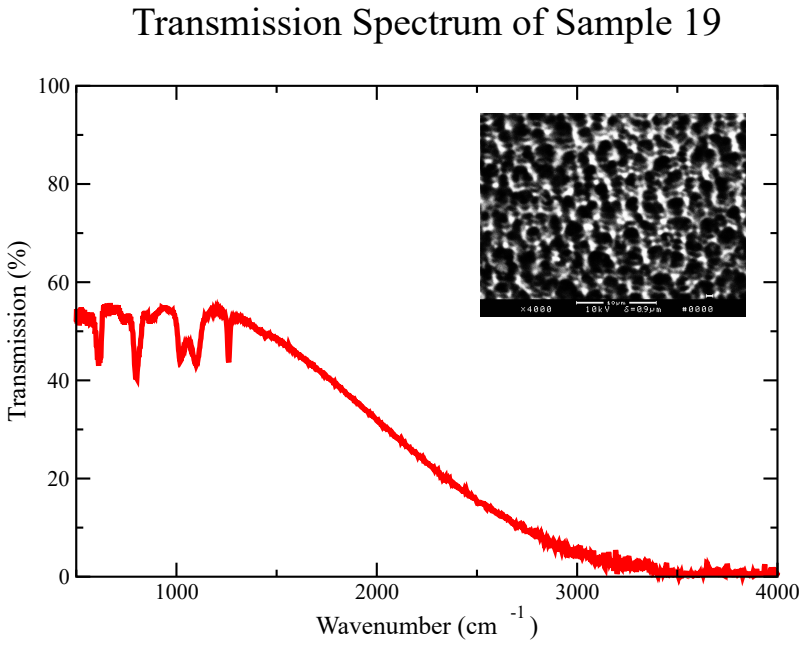

Figure A.19: Transmission Spectrum for Sample 19. Inset is the corresponding SEM image.

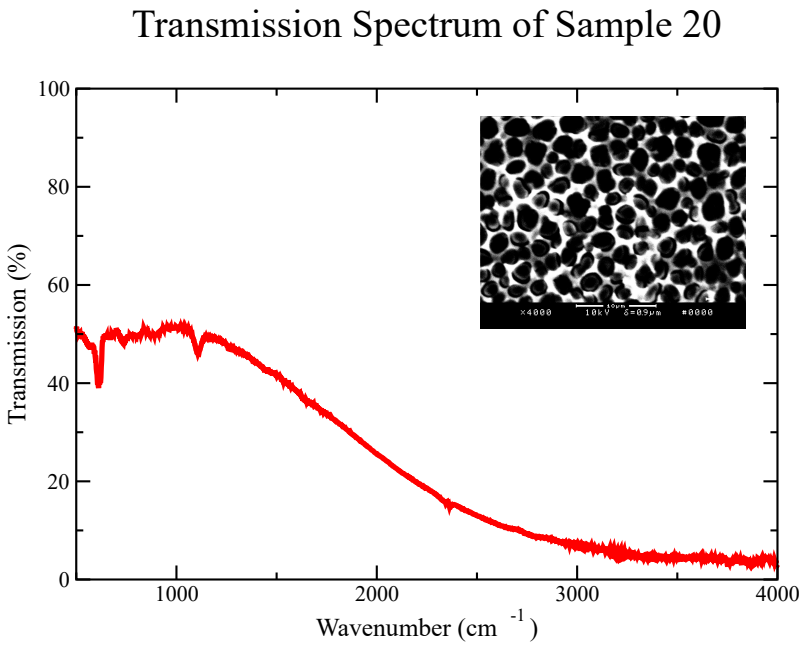

Figure A.20: Transmission Spectrum for Sample 20. Inset is the corresponding SEM image.

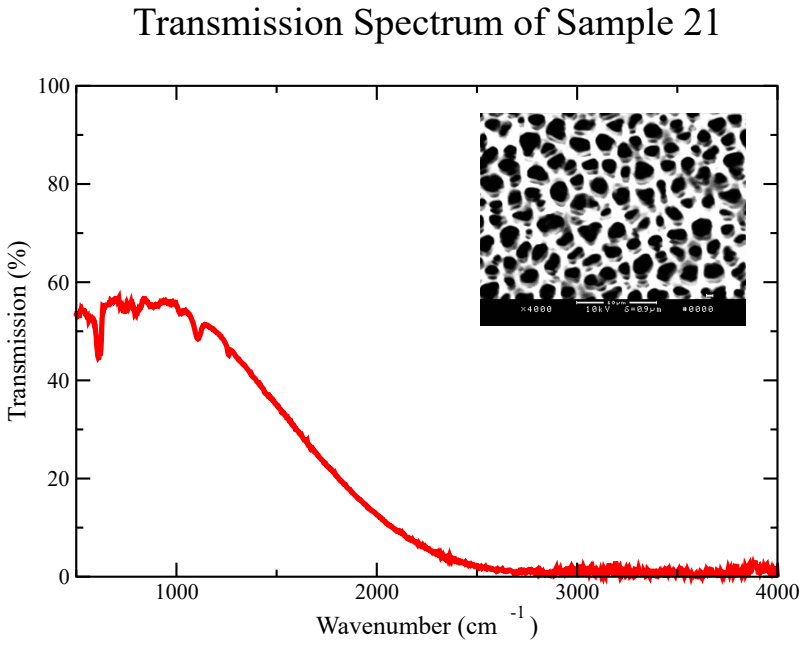

Figure A.21: Transmission Spectrum for Sample 21. Inset is the corresponding SEM image.

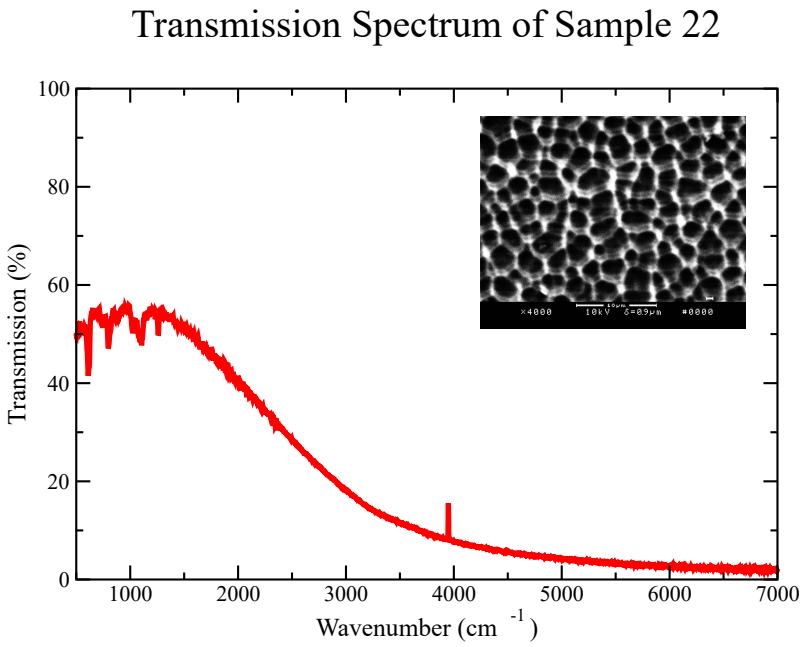

Figure A.22: Transmission Spectrum for Sample 22. Inset is the corresponding SEM image.

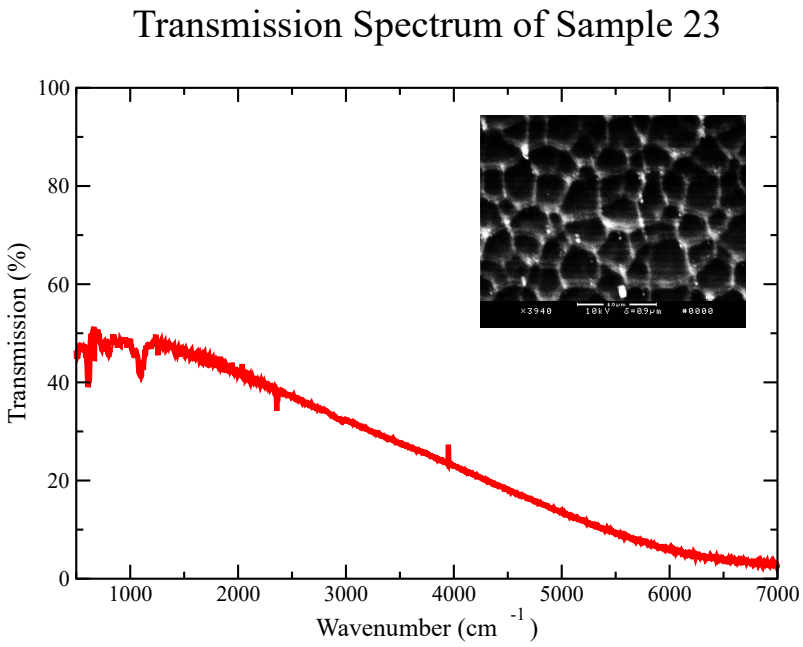

Figure A.23: Transmission Spectrum for Sample 23. Inset is the corresponding SEM image.

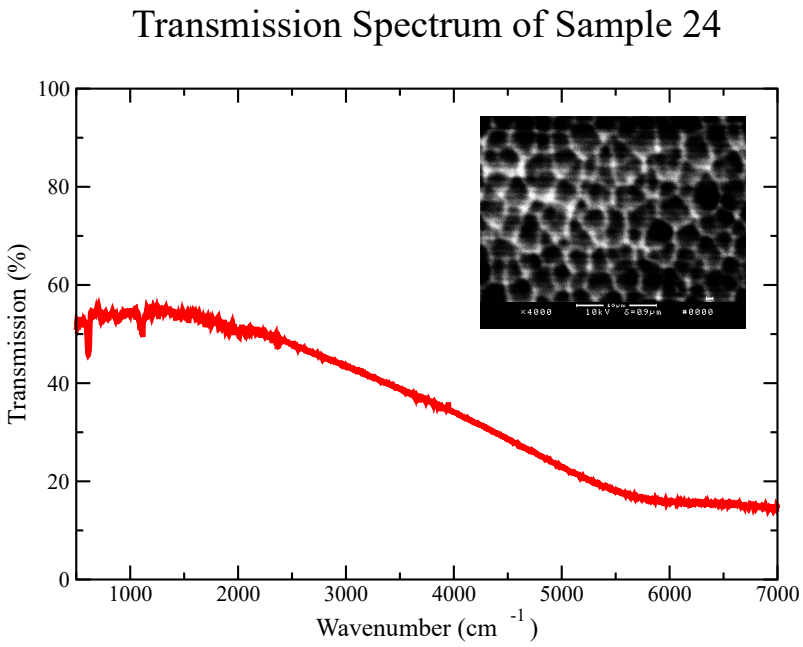

Figure A.24: Transmission Spectrum for Sample 24. Inset is the corresponding SEM image.

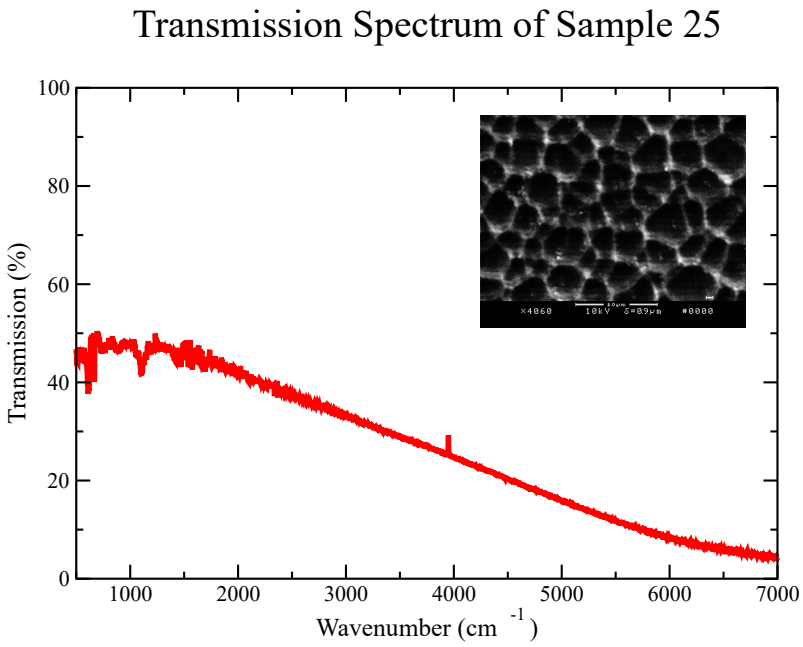

Figure A.25: Transmission Spectrum for Sample 25. Inset is the corresponding SEM image.

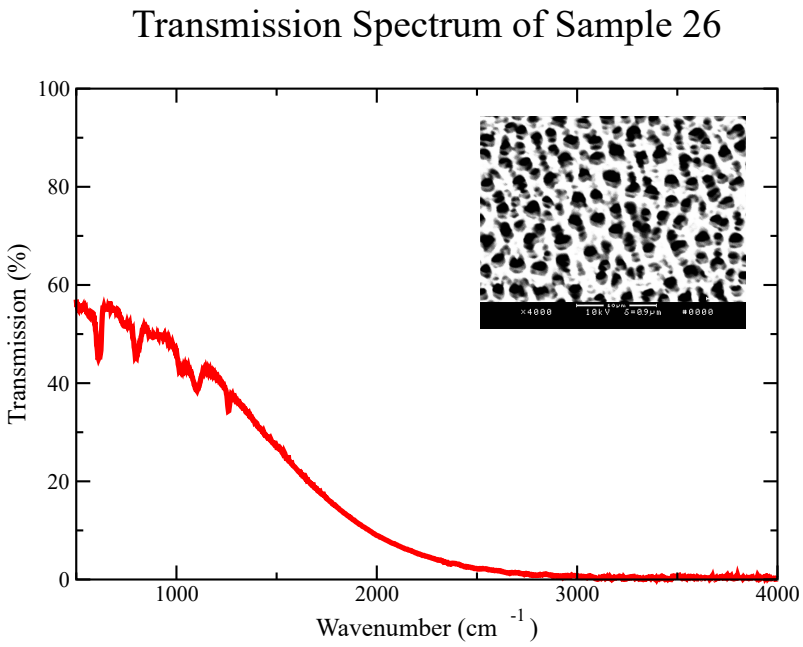

Figure A.26: Transmission Spectrum for Sample 26. Inset is the corresponding SEM image.

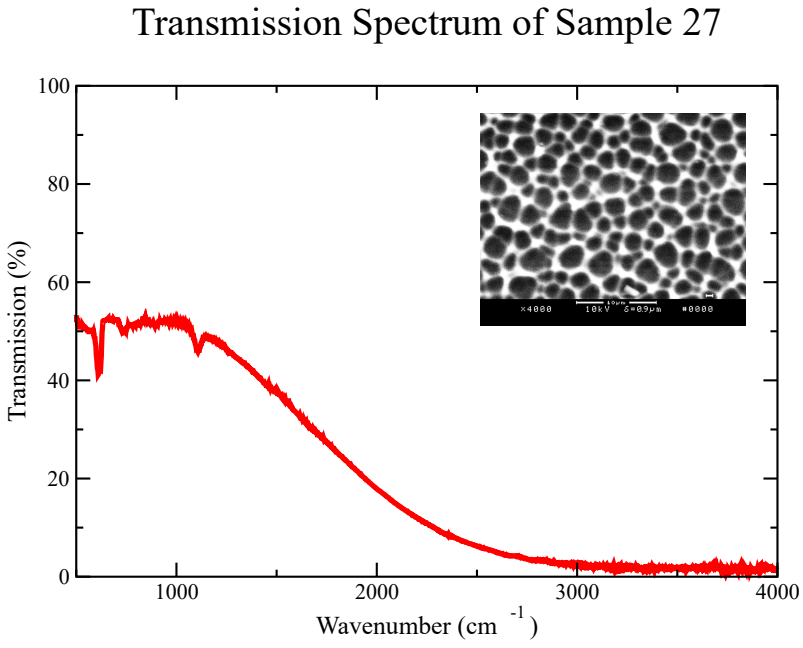

Figure A.27: Transmission Spectrum for Sample 27. Inset is the corresponding SEM image.

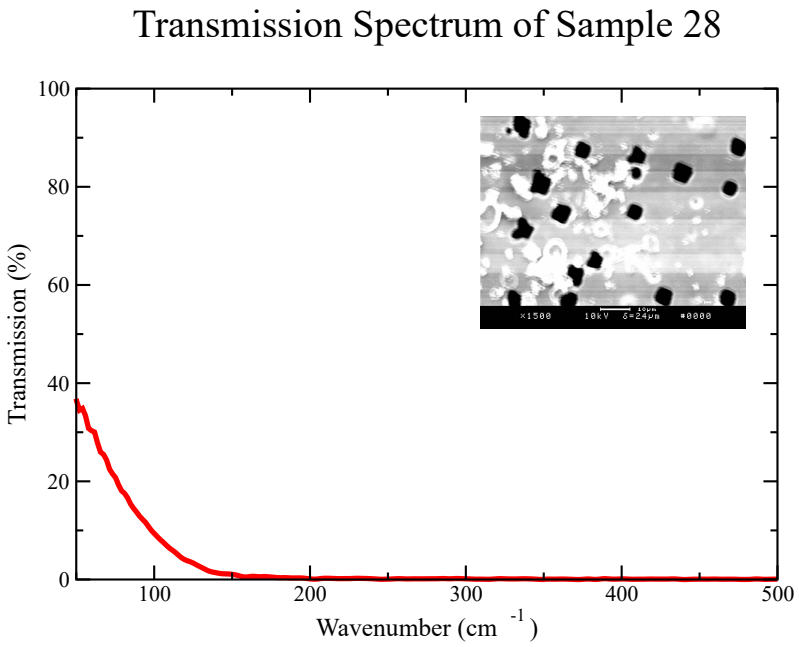

Figure A.28: Transmission Spectrum for Sample 28. Inset is the corresponding SEM image. The image has a magnification of 1500x.

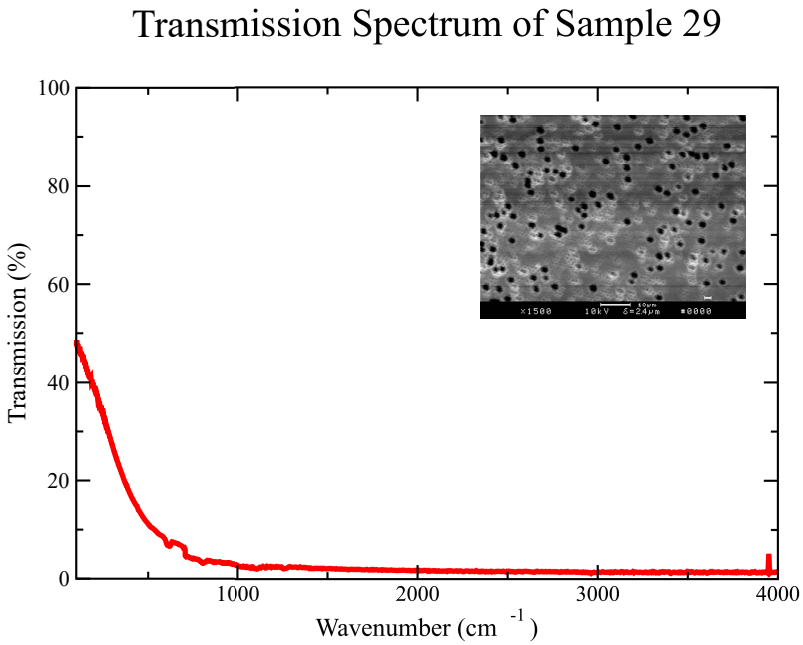

Figure A.29: Transmission Spectrum for Sample 29. Inset is the corresponding SEM image. The image has a magnification of 1500x.

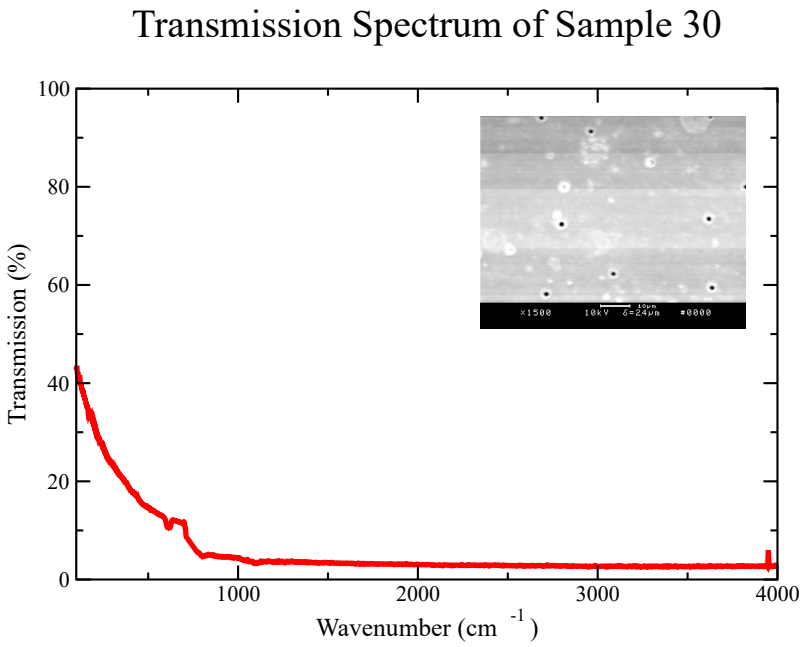

Figure A.30: Transmission Spectrum for Sample 30. Inset is the corresponding SEM image. The image has a magnification of 1500X.

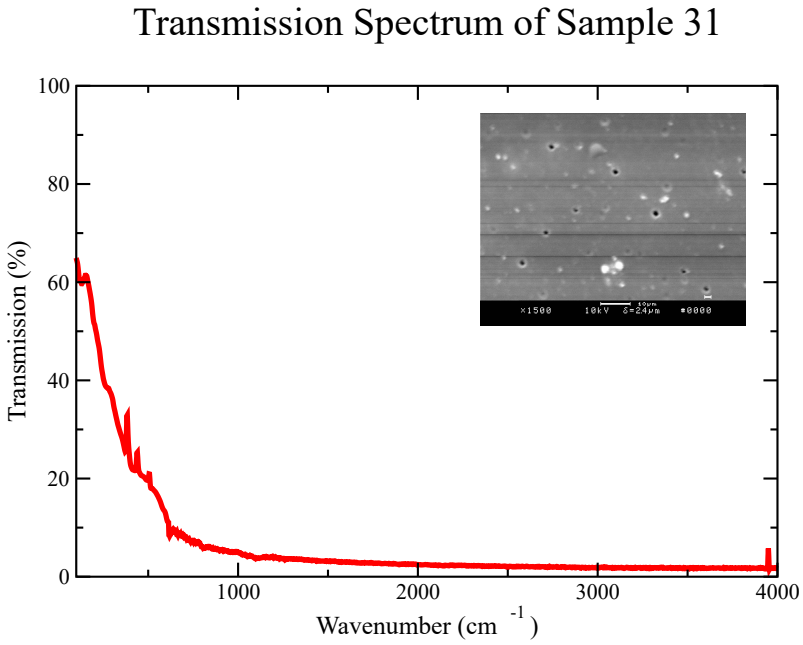

Figure A.31: Transmission Spectrum for Sample 31. Inset is the corresponding SEM image. The image has a magnification of 1500X.

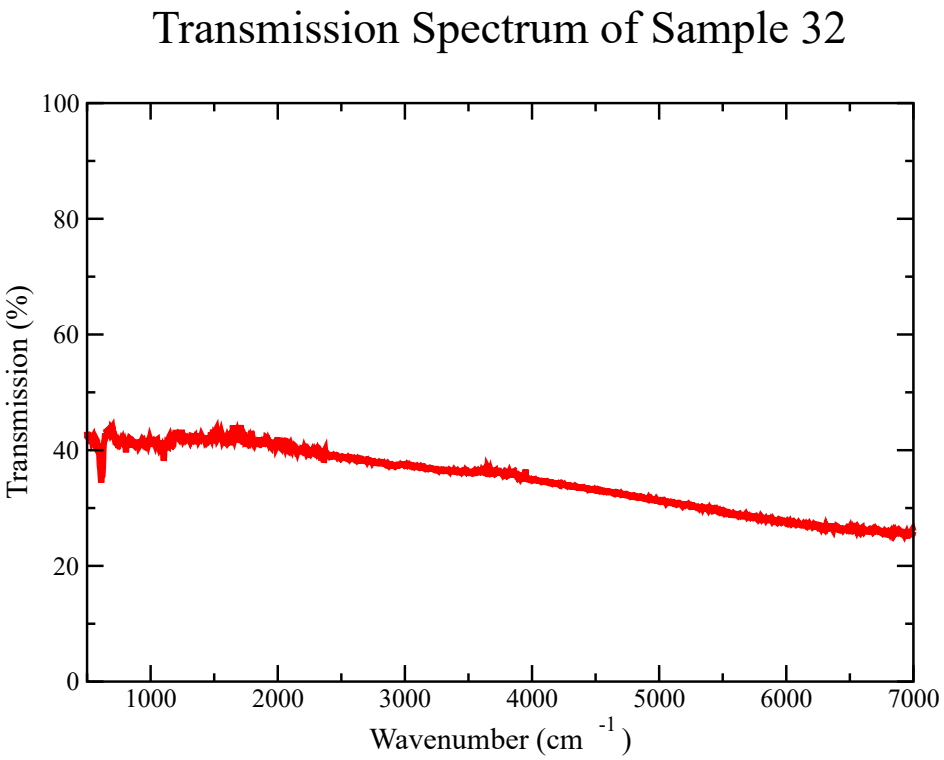

Figure A.32: Transmission Spectrum for Sample 32.

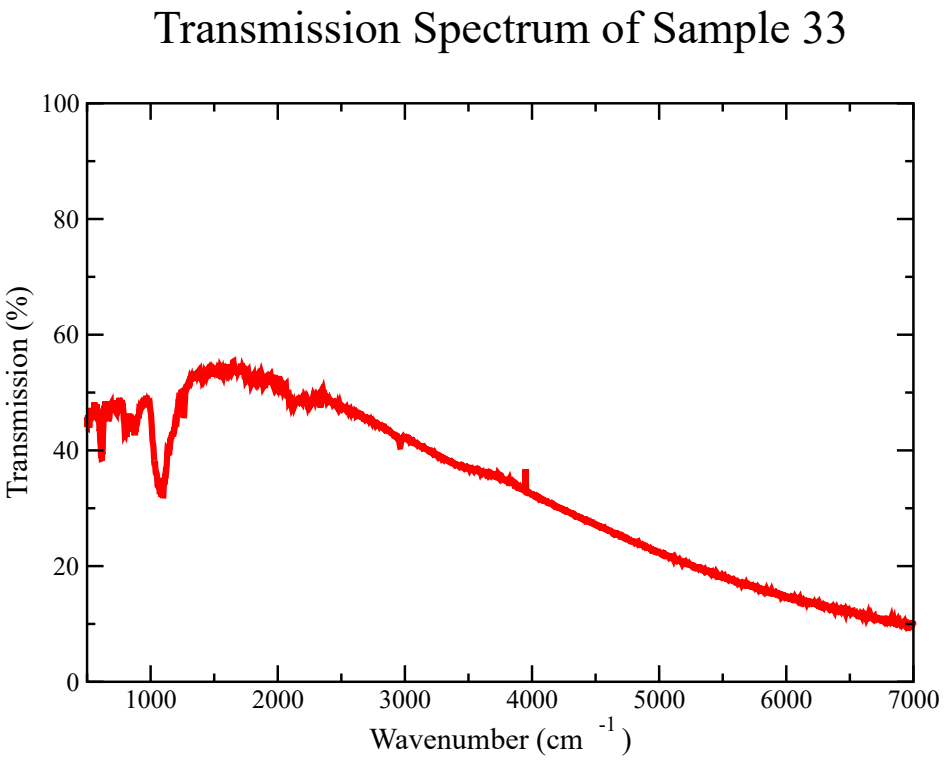

Figure A.33: Transmission Spectrum for Sample 33.

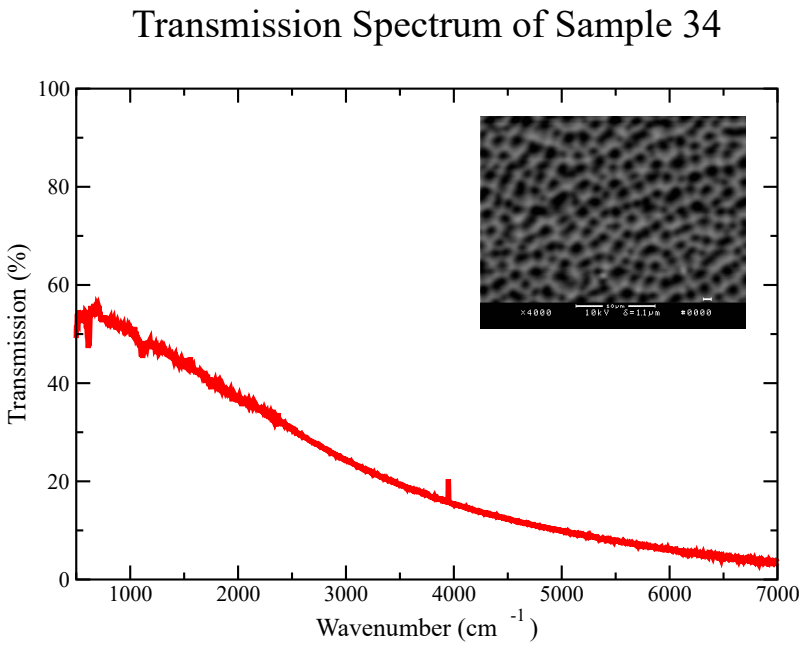

Figure A.34: Transmission Spectrum for Sample 34. Inset is the corresponding SEM image.

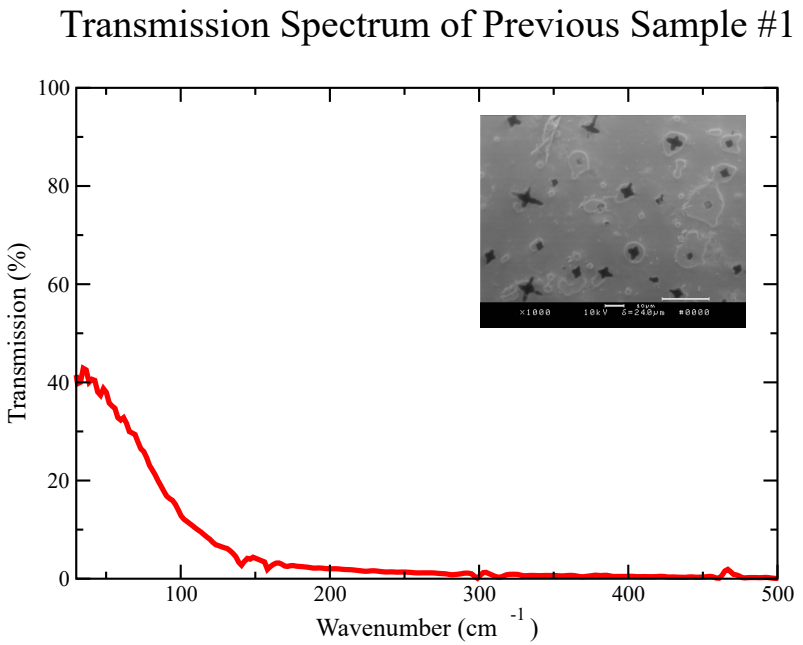

Figure A.35: Transmission Spectrum for previous Sample 1 [50]. Inset is the corresponding SEM image. The image has a magnification of 1000X.

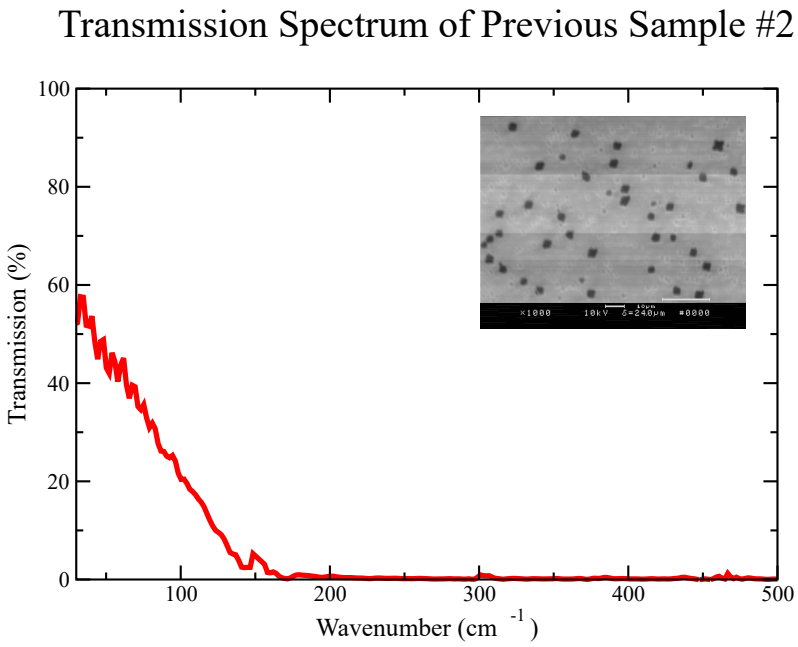

Figure A.36: Transmission Spectrum for previous Sample 2 [50]. Inset is the corresponding SEM image. The image has a magnification of 1000X.

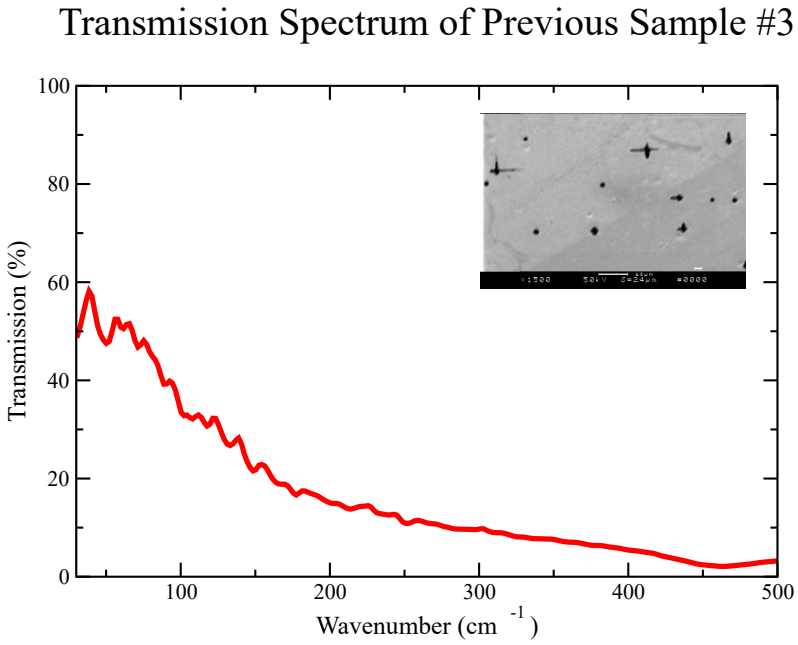

Figure A.37: Transmission Spectrum for previous Sample 3[1]. Inset is the corresponding SEM image. The image has a magnification of 1500X.

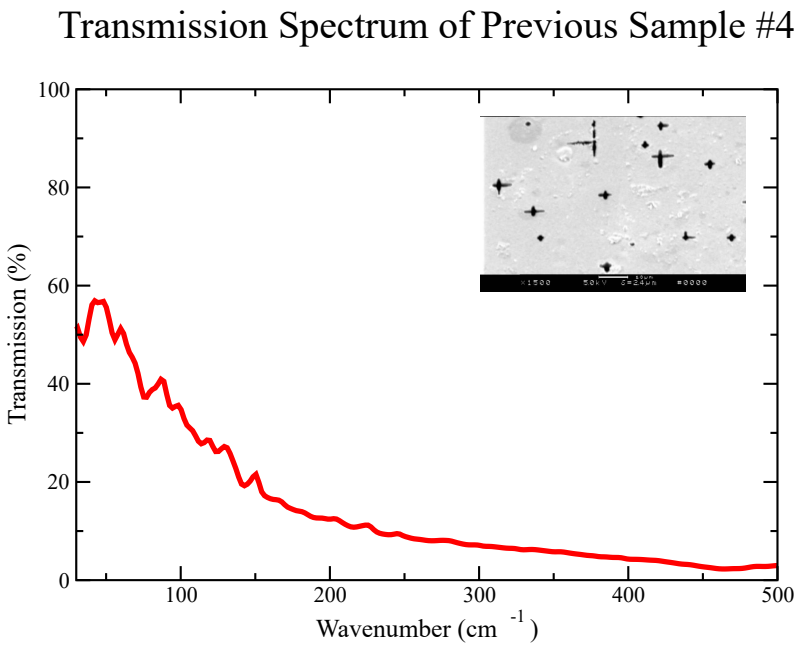

Figure A.38: Transmission Spectrum for previous Sample 4[2]. Inset is the corresponding SEM image. The image has a magnification of 1500X.

[1]Etched by N. Majtenyi
[2]Etched by N. Dwyer

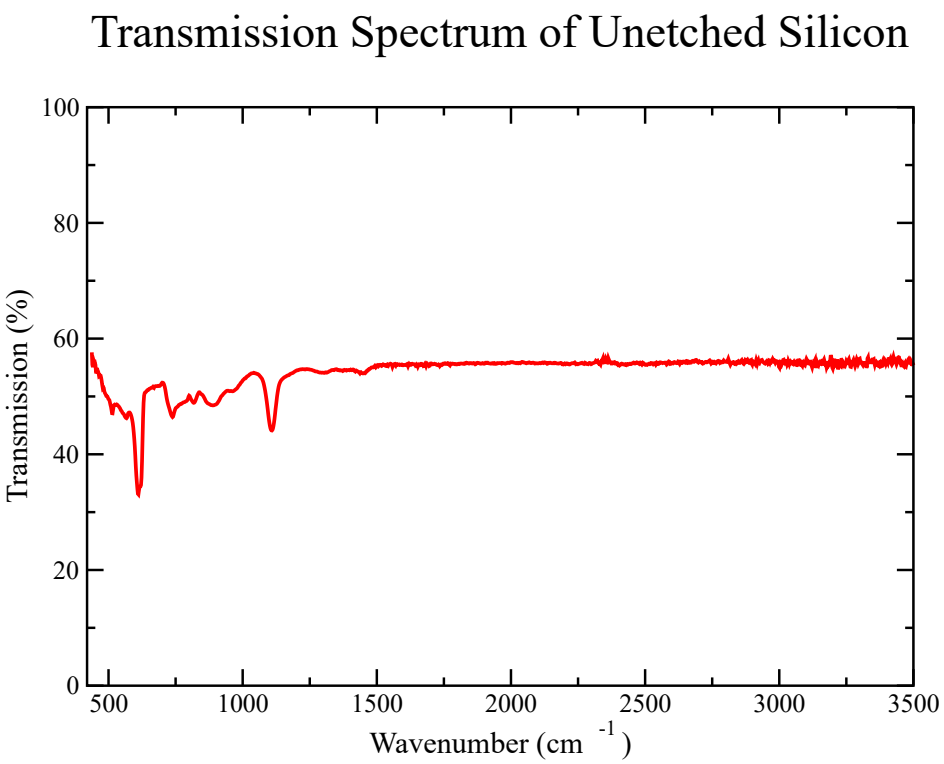

Figure A.39: Transmission Spectrum for unetched silicon.

Appendix B

Data Summary and Error Bar Analysis

This appendix provides a summary of all of the data compiled for this thesis along with the associated error bars. In addition to this, the method by which these error bars were obtained will also be outlined.

For the purposes of this appendix, the pore number density will be given as n, the pore coverage as c, the cutoff wavenumber as w, the cutoff wavelength as λ and the average pore radius as r.

For the pore coverage, pore number density, and NND values the error bars were simply taken to be the standard deviation of the series of measurements taken. These standard deviation values were then used in calculating the error bars for the pore radius values by using standard propagation of uncertainty rules. The equation used to calculate the error bar for the radius as per these rules where $\sigma(x)$ is the error bar associated with the quantity x is [56]:

$$\sigma(r) = \frac{r}{2}\sqrt{\left(\frac{\sigma(d)}{d}\right)^2 + \left(\frac{\sigma(c)}{c}\right)^2} \tag{B.1}$$

For the cutoff wavenumber, the error bars were taken to be the larger of two values: the standard deviation associated with the series of measurements taken or 1 cm^{-1}. This second value comes from the fact that, upon examination of the

data files, the difference between consecutive data points was approximately 2 cm^{-1}. As such, the error bar could be estimated to be half of this value.

The cutoff wavelength is given by $\lambda = w^{-1}$. As such, the error bar associated with this can be given by [56]:

$$\sigma(\lambda) = \frac{\sigma(w)}{w^2} \tag{B.2}$$

The data values and error bars for the topological measurements are given in Tables B.1 and B.2 respectively. The data values and error bars for the optical measurements are given in Tables B.3 and B.4 respectively.

Table B.1: Summary table of topological results.

Sample	n (pores/100 μm^2)	c (%)	r (μm)	NND (μm)
1	7.3	64.9	1.68	3.65
2	7.8	47.6	1.39	3.23
3	6.5	58.2	1.69	3.71
4	9.2	45.2	1.25	2.92
5	15.7	46.9	0.98	2.05
6	6.7	44.2	1.45	4.08
7	8.3	47.8	1.35	3.63
8	11.3	46.7	1.15	2.90
9	No Image	No Image	No Image	No Image
10	14	52.5	1.09	1.99
11	16	58	1.07	2.22
12	14.2	50.4	1.06	1.95
13	19.5	65	1.03	2.06
14	18.2	65.3	1.07	1.91
15	15.5	37.9	0.88	1.89
16	16.5	51	0.99	1.94
17	14.8	49.6	1.03	2.17
18	16.8	72.6	1.17	2.27
19	15.2	60.7	1.13	2.34
20	13.3	65.2	1.25	2.15
21	14.5	45.7	1	2.29
22	15.3	55.1	1.07	2.28
23	9.8	84.5	1.66	3.42
24	14.3	69.1	1.24	2.40
25	9.7	77.2	1.59	2.98
26	12.2	36.6	0.98	2.11
27	16	58.9	1.08	2.26
28	0.3	7.7	2.86	13.19
29	1.6	7.3	1.21	4.89
30	0.18	0.42	0.86	18.92
31	0.23	0.25	0.59	13.97
32	No Image	No Image	No Image	No Image
33	No Image	No Image	No Image	No Image
34	Unreliable	Unreliable	Unreliable	Unreliable

Table B.2: Summary table of topological error bars.

Sample	$\sigma(d)$ (pores/100 μm^2)	$\sigma(c)$ (%)	$\sigma(r)$ (μm)	σ(NND) (μm)
1	1.6	2.0	0.19	0.42
2	0.8	2.3	0.08	0.17
3	0.8	2.5	0.11	0.19
4	1.5	1.1	0.1	0.08
5	1.4	2.0	0.05	0.16
6	1.4	3.6	0.16	0.31
7	0.8	2.9	0.08	0.05
8	1.2	4.1	0.08	0.08
9	N/A	N/A	N/A	N/A
10	1.5	1.1	0.06	0.13
11	1.5	4.7	0.07	0.14
12	1.7	3.3	0.07	0.07
13	1	4.1	0.04	0.02
14	0.4	3.7	0.03	0.02
15	1	4.2	0.06	0.07
16	0.5	4.5	0.05	0.05
17	1.2	6.9	0.08	0.08
18	1.5	3.2	0.06	0.11
19	0.8	5.7	0.06	0.36
20	1	0.3	0.05	0.07
21	1.2	0.4	0.04	0.06
22	1.6	5.0	0.07	0.06
23	1	3.3	0.09	0.33
24	1.2	2.4	0.06	0.09
25	1	5.9	0.1	0.14
26	1.3	3.4	0.07	0.15
27	1.7	2.2	0.06	0.10
28	0.04	1.6	0.35	1.40
29	0.36	3.0	0.28	0.58
30	0.04	0.2	0.23	5.17
31	0.04	0.1	0.13	1.29
32	N/A	N/A	N/A	N/A
33	N/A	N/A	N/A	N/A
34	N/A	N/A	N/A	N/A

Table B.3: Summary table of optical results.

Sample	ω_1 (cm^{-1})	ω_2 (cm^{-1})	λ_1 (μm)	λ_2 (μm)
1	1406.0	777.3	7.11	12.87
2	1089.3	671.2	9.18	14.90
3	1163.3	673.5	8.60	14.85
4	1292.2	731.0	7.74	13.68
5	1868.8	785.0	5.35	12.74
6	1165.3	707.8	8.58	14.13
7	1492.7	942.0	6.70	10.62
8	1209.2	713.6	8.27	14.01
9	V. High	4734.0	V. Low	2.11
10	2399.2	1670.9	4.17	5.98
11	3017.3	2251.8	3.31	4.44
12	V. High	V. High	V. Low	V. Low
13	2067.5	1419.5	4.84	7.04
14	2487.6	1666.3	4.02	6.00
15	2138.5	1431.8	4.68	6.98
16	3230.1	2277.3	3.10	4.39
17	2347.9	1722.3	4.26	5.81
18	V. High	2890.3	V. Low	V. Low
19	2948.9	2142.7	3.39	4.67
20	3186.5	1977.6	3.14	5.06
21	2283.5	1656.7	4.38	6.04
22	4730.1	2422.4	2.11	4.13
23	6224.1	3428.4	1.61	2.92
24	V. High	4634.5	0	2.16
25	6777	3749.3	1.48	2.67
26	2223.3	1500.5	4.50	6.66
27	2598.7	1762.8	3.85	5.67
28	114.9	63.6	87.03	157.23
29	677.7	300.8	14.76	33.24
30	791.8	246.8	12.63	40.52
31	995.9	362.6	10.04	27.58
32	V. High	V. High	V. Low	V. Low
33	V. High	V. High	V. Low	V. Low
34	Irrelevant	Irrelevant	Irrelevant	Irrelevant

Table B.4: Summary table of optical error bars.

Sample	$\sigma(\omega_1)$ (cm^{-1})	$\sigma(\omega_2)$ (cm^{-1})	$\sigma(\lambda_1)$ (μm)	$\sigma(\lambda_2)$ (μm)
1	1.0	1.0	0.005	0.017
2	1.0	1.0	0.008	0.022
3	1.0	1.0	0.007	0.022
4	1.0	1.0	0.006	0.019
5	1.0	1.0	0.003	0.016
6	1.0	1.0	0.007	0.02
7	1.0	1.1	0.004	0.012
8	1.0	1.0	0.007	0.02
9	Unknown	19.2	N/A	0.009
10	1.4	6.4	0.002	0.023
11	1.0	1.0	0.001	0.002
12	Unknown	Unknown	N/A	N/A
13	1.0	1.0	0.002	0.005
14	2.5	1.0	0.004	0.004
15	1.0	1.1	0.002	0.005
16	14.8	1.0	0.014	0.002
17	3.2	1.0	0.006	0.003
18	Unknown	5.2	N/A	0.006
19	1.0	1.0	0.001	0.002
20	7.8	11.2	0.008	0.029
21	5.3	1.0	0.01	0.004
22	10.6	1.0	0.005	0.002
23	10.1	33.3	0.003	0.028
24	Unknown	3.2	N/A	0.001
25	13	6.7	0.003	0.005
26	1.0	1.0	0.002	0.004
27	1.0	1.0	0.001	0.003
28	1.1	1.0	0.833	2.472
29	3.2	1.0	0.070	0.111
30	1.7	1.0	0.027	0.164
31	7.5	1.0	0.076	0.076
32	N/A	N/A	N/A	N/A
33	N/A	N/A	N/A	N/A
34	N/A	N/A	N/A	N/A

Appendix C

Alignment Procedure for Bruker Optical Box

The alignment procedure for the Bruker's optical box is described in this appendix.

A schematic of the setup is given in Figure C.1. In order to perform measurements with this setup, it was critical to ensure that the mirrors were properly aligned such that the beam path was such that it passed through the sample and to the detector. This was done in advance of the measurements using the tungsten lamp (i.e. with a visible beam) and a transparent Mylar beamsplitter. The mirrors were then adjusted such that the beam path was correct. The correct beam path is as follows:

1. The beam should enter the box (labeled as "light source" in Figure C.1.)
2. The beam should strike mirror M1.
3. The beam should strike mirror M2.
4. The beam should pass through the adjustable aperture. This aperture allows for the control of the diameter of the beam when it passes through the sample.
5. The beam should strike mirror M3.

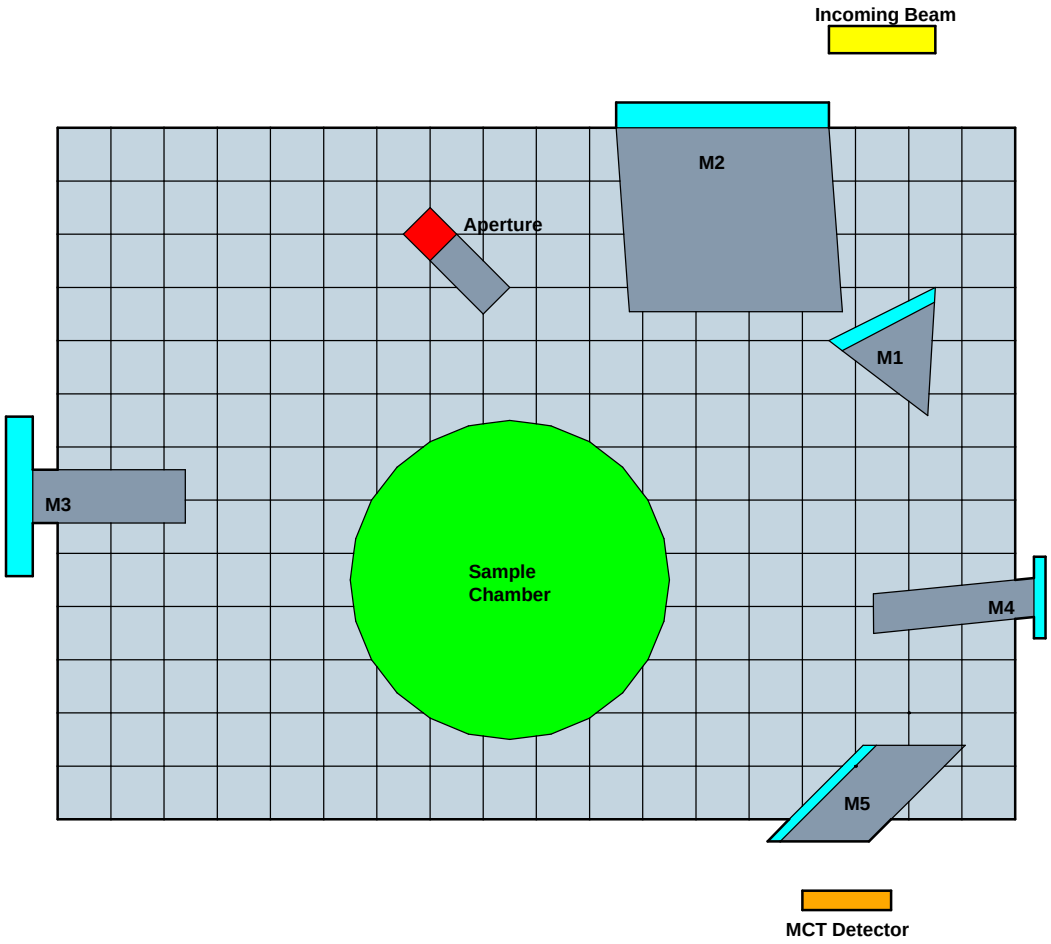

Figure C.1: Schematic of the interior of the optical box. The grid represents the optical table into which all of the optical components are secured.

6. The beam should pass through the sample.

7. The beam should strike mirror M4.

8. The beam should strike mirror M5.

9. The beam should strike the MCT detector.

Appendix D

Temperature-Dependent Optical Measurements

This appendix will present the optical cutoff data for the seven samples on which temperature-dependent measurements were performed. Tables D.1-D.7 will contain the cutoff values as a function of temperature and Figures D.1-D.7 will contain the averaged transmission spectra for each sample.

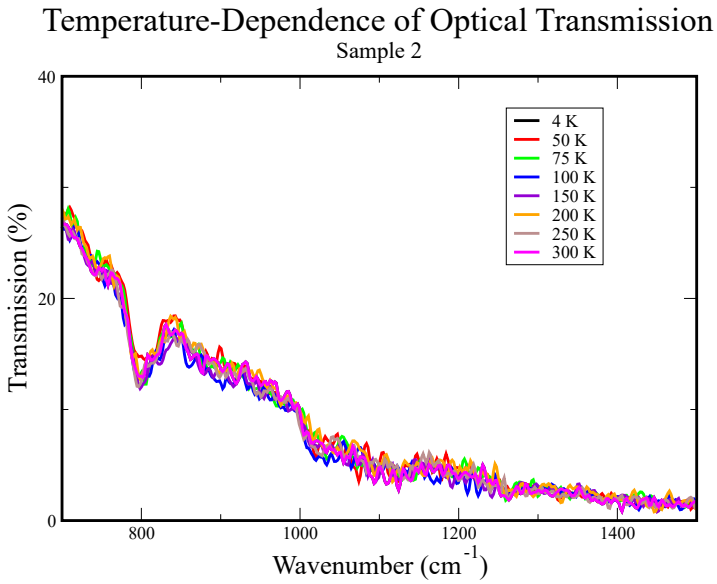

Figure D.1: Temperature-dependence of the transmission spectra for Sample 2.

Table D.1: Temperature-dependent cutoff values for Sample 2.

Temperature (K)	Cutoff (cm^{-1})
4	1076.7
50	1077.2
75	1081.1
100	1086.7
150	1078.0
200	1086.5
250	1078.8
300	1077.2

Table D.2: Temperature-dependent cutoff values for Sample 4.

Temperature (K)	Cutoff (cm^{-1})
4	1243.9
50	1237.3
75	1239.6
100	1234.2
150	1220.7
200	1199.9
250	1181.4
300	1181.0

Table D.3: Temperature-dependent cutoff values for Sample 6.

Temperature (K)	Cutoff (cm^{-1})
4	1236.6
50	1242.7
75	1242.4
100	1246.2
150	1261.2
200	1273.2
250	1285.9
300	1280.9

Table D.4: Temperature-dependent cutoff values for Sample 14.

Temperature (K)	Cutoff (cm^{-1})
4	1785.4
50	1785.4
75	1790.8
100	1791.9
150	1793.5
200	1801.2
250	1824.8
300	1837.1

Table D.5: Temperature-dependent cutoff values for Sample 19.

Temperature (K)	Cutoff (cm^{-1})
4	3162.3
50	3185.8
75	3151.1
100	3163.1
150	3148.4
200	3162.2
250	3160.3
300	3144.6

Table D.6: Temperature-dependent cutoff values for Sample 20.

Temperature (K)	Cutoff (cm^{-1})
4	2268.6
50	2265.9
75	2259.8
100	2260.5
150	2255.1
200	2226.2
250	2217.0
300	2188.3

Table D.7: Temperature-dependent cutoff values for Sample 21.

Temperature (K)	Cutoff (cm^{-1})
4	1687.8
50	1686.6
75	1685.1
100	1680.5
150	1677.0
200	1669.7
250	1670.1
300	1677.4

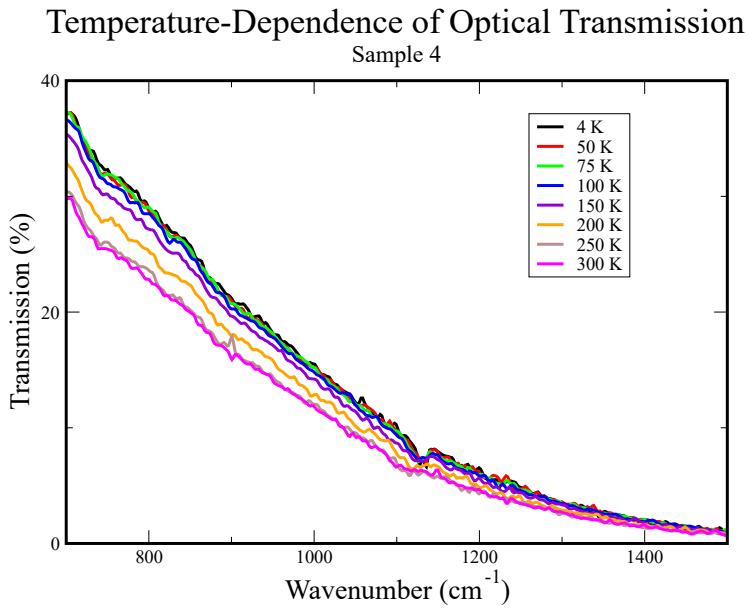

Figure D.2: Temperature-dependence of the transmission spectra for Sample 4.

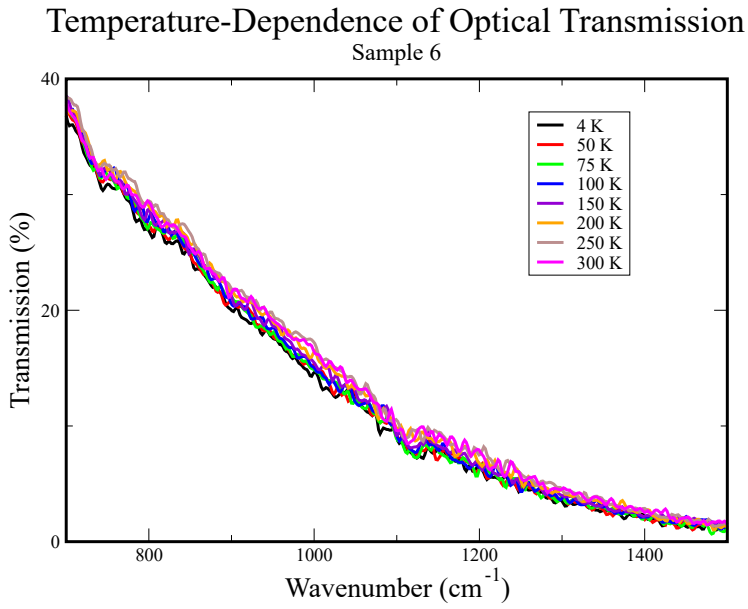

Figure D.3: Temperature-dependence of the transmission spectra for Sample 6.

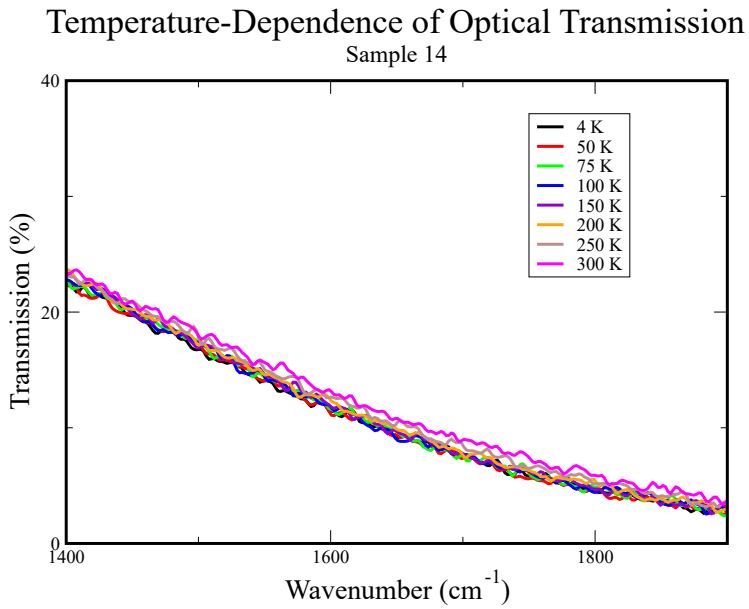

Figure D.4: Temperature-dependence of the transmission spectra for Sample 14.

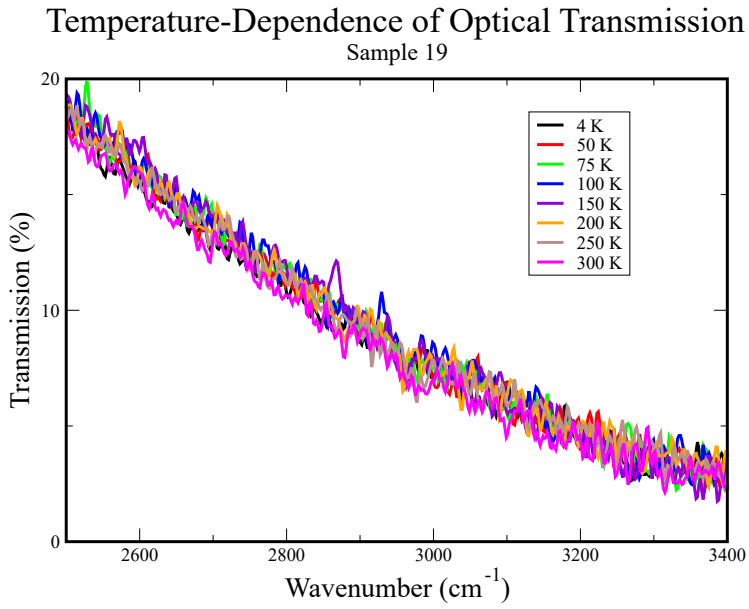

Figure D.5: Temperature-dependence of the transmission spectra for Sample 19.

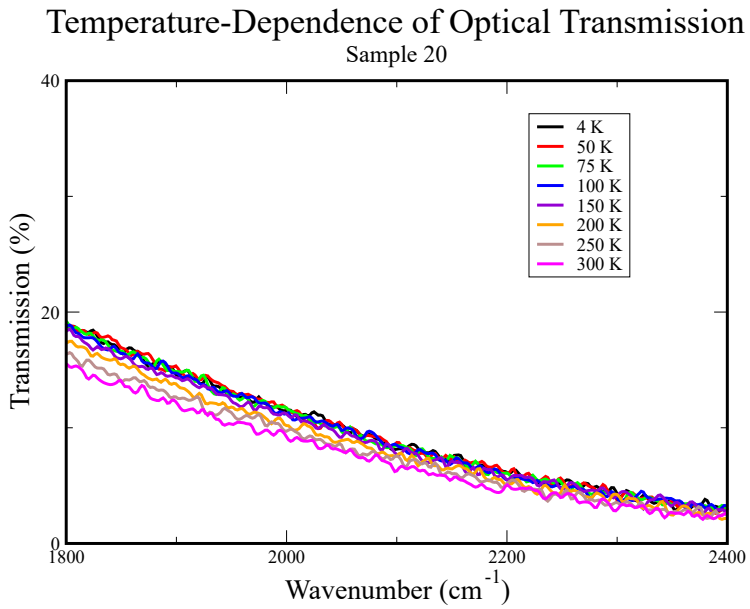

Figure D.6: Temperature-dependence of the transmission spectra for Sample 20.

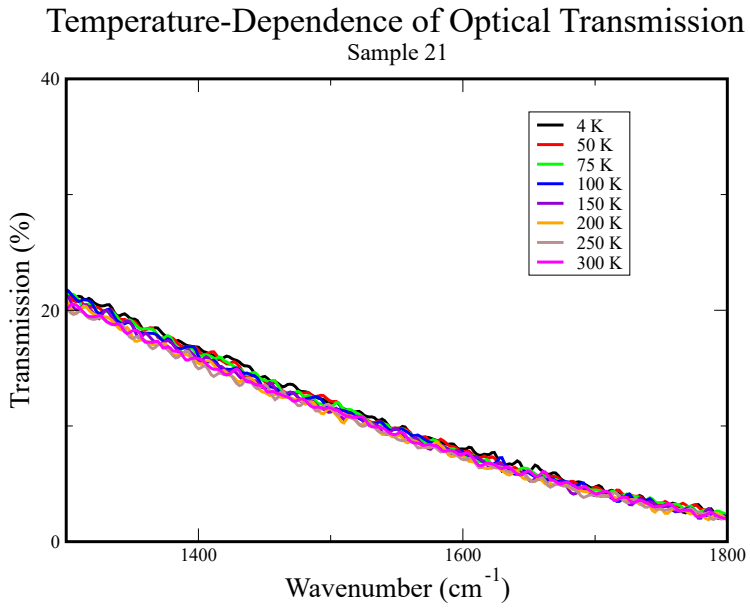

Figure D.7: Temperature-dependence of the transmission spectra for Sample 21.

Bibliography

[1] A. Uhlir. "Electrolytic Shaping of Germanium and Silicon." *Bell Labs Technical Journal*, **35**, 333-347, 1956.

[2] M. Sailor. *Porous Silicon in Practice: Preparation, Characterization and Applications*, Wiley-VCH, Weinheim, 2011.

[3] L. Canham. "Silicon Quantum Wire Array Fabrication by Electrochemical and Chemical Dissolution of Wafers." *Applied Physics Letters*, **57**, 1046-1048, 1990.

[4] V. Kochergin and H. Foell. "Novel Optical Elements Made from Porous Si." *Materials Science and Engineering Review*, **52**, 93-140, 2006.

[5] V. Lehmann, R. Stengl, et al. "Optical Shortpass Filters Based on Macroporous Silicon." *Applied Physics Letters*, **78**, 589-591, 2001.

[6] A. Loni. "Porous Silicon Formation by Anodization." In L. Canham (Ed.). *Handbook of Porous Silicon*, Springer, Zug, 2014.

[7] H. Foell, M. Christophersen, et al. "Formation and Application of Porous Silicon." *Materials Science and Engineering Review*, **280**, 1-49, 2002.

[8] V. Lehmann and U. Goesele. "Porous Silicon Formation: A Quantum Wire Effect." *Applied Physics Letters*, **58**, 856-858, 1991.

[9] R. Smith and S. Collins. "Porous Silicon Formation Mechanisms." *Journal of Applied Physics*, **71**, 1-22, 1992.

[10] R. Memming. *Semiconductor Electrochemistry*, Wiley-VCH, Weinheim, 2001.

[11] U. Goesele and V. Lehmann. "Porous Silicon Quantum Sponge Structures: Formation Mechanism, Preparation Methods and Some Properties." In Z. Feng and R. Tsu (Ed.). *Porous Silicon*, World Scientific, Singapore, 1994.

[12] E. Perez. *Design, Fabrication, and Characterization of Porous Silicon Multilayer Optical Devices*, Universitat Rovira i Vergili, Tarragona, 2007.

[13] O. Bisi, S. Ossicini and L. Pavesi. "Porous Silicon: A Quantum Sponge Structure for Silicon Based Optoelectronics." *Surface Science Reports*, **38**, 1-126, 2000.

[14] L. Pavesi and V. Mulloni. "All Porous Silicon Microcavities: Growth and Physics." *Journal of Luminescence*, **80**, 43-52, 1999.

[15] C. Vinegoni, M. Cazzanelli and L. Pavesi. "Porous Silicon Microcavities." In H. Nalwa (Ed.). *Silicon-Based Materials and Devices, Volume 2*, Academic Press, San Diego, 2001.

[16] N. Burham et al. "Effect of Hydrofluoric Acid (HF) Concentration to Pores Size Diameter of Silicon Membrane." *Bio-Medical Materials and Engineering*, **24**, 2203-2209, 2014.

[17] P. Kumar et al. "Effect of HF Concentration on Physical and Electronic Properties of Electrochemically Formed Nanoporous Silicon." *Journal of Nanomaterials*, **2009**, 1-7, 2009.

[18] A. Ramizy, I. Ibrahim and M. Hammadi. "The Effect of Etching Current Density on Porous Silicon Fabricated by Electrochemical Etching Process." *International Journal of Scientific and Engineering Research*, **7**, 717-721, 2016.

[19] M. Christophersen, J. Carstensen, et al. "Crystal Orientation Dependence and Anisotropic Properties of Macropore Formation of p- and n-Type Silicon." *Journal of the Electrochemical Society*, **148**, E267-E275, 2001.

[20] G. Zhang. "Porous Silicon: Morphology and Formation Mechanisms." In C. Vayenas et al. (Ed.). *Modern Aspects of Electrochemistry, Number 39*, Springer, New York, 2005.

[21] G. Zhang. "Mechanism of Pore Formation on n-Type Silicon." *Journal of the Electrochemical Society*, **138**, 3750-3756, 1991.

[22] P. Dunn. *Gateway Into Electronics*, Wiley, New York, 2000.

[23] U. Hansen and P. Vogl. "Hydrogen Passivation of Silicon Surfaces: A Classical Molecular-Dynamics Study." *Physical Review B*, **57**, 13295-13304, 1998.

[24] J. Carstensen, M. Christophersen et al. "Parameter Dependence of Pore Formation in Silicon within a Model of Local Current Bursts." *Physica Status Solidi (a)*, **182**, 63-69, 2000.

[25] H. Foell, J. Carstensen et al. "A New View of Silicon Electrochemistry." *Physica Status Solidi (a)*, **182**, 7-16, 2000.

[26] V. Kochergin and H. Foell. "Commercial Applications of Porous Si: Optical Filters and Components." *Physica Status Solidi (c)*, **4**, 1933-1940, 2007.

[27] V. Kochergin, M. Sanghavi and P. Swinehart. "Porous Silicon Filters for Low-Temperature far IR Applications". *Proceedings of SPIE*, **5883**, 184-191, 2005.

[28] K. Armstrong and F. Low. "Far-Infrared Filters Utilizing Small Particle Anti-Reflection Coatings." *Applied Optics*, **13**, 425-430, 1974.

[29] M. Morita et al. "Growth of Native Oxide on a Silicon Surface." *Journal of Applied Physics*, **68**, 1272-1281, 1990.

[30] V. Kochergin and H. Foell. *Porous Semiconductors: Optical Properties and Applications*, Springer, London, 2009.

[31] D. Graef et al. "Oxidation of HF-Treated Si Wafer Surfaces in Air." *Journal of Applied Physics*, **68**, 5155-5161, 1990.

[32] B. El-Kareh. *Fundamentals of Semiconductor Processing Technologies*, Springer, New York, 1995.

[33] Y. Ogata. "Characterization of Porous Silicon by Infrared Spectroscopy" In L. Canham (Ed.). *Handbook of Porous Silicon*, Springer, Zug, 2014.

[34] M. Christophersen, V. Kochergin and P. Swinehart. "Porous Silicon Filters for Mid-to-Far IR Range". *Proceedings of SPIE*, **5524**, 158-168, 2004.

[35] Keithley Instruments Inc. Keithley Model 220 Programmable Current Source: Instruction Manual. Cleveland, Author, 1982.

[36] L. Van Der Pauw. "A Method of Measuring Specific Resistivity and Hall Effect of Discs of Arbitrary Shape". *Phillips Research Reports*, **13**, 1-9, 1958.

[37] J. Thomas. *Silicon*, Marshall-Cavendish, Tarrytown, 2002.

[38] P. Goodhew, J. Humphreys, and R. Beanland. *Electron Microscopy and Analysis: Third Edition*, Taylor and Francis, London, 2001.

[39] J. Goldstein, D. Newbury et al. *Scanning Electron Microscopy and X-ray Microanalysis*, Springer, New York, 2003.

[40] L. Reimer. *Scanning Electron Microscopy: Physics of Image Formation and Image Analysis*, Springer-Verlag, Berlin, 1998.

[41] Bio-Rad Laboratories, Inc. Operation and Installation Manual for SC500 Sputter Coater. Berkeley, Author, n.d.

[42] P. Echlin. *Handbook of Sample Preparation for Scanning Electron Microscopy and X-Ray Microanalysis*, Springer, New York, 2009.

[43] P. Griffiths and J. de Haseth. *Fourier Transform Infrared Spectroscopy*, Wiley, Hoboken, 2007.

[44] B. Smith. *Fundamentals of Fourier Transform Infrared Spectroscopy*, CRC Press, Boca Raton, 1996.

[45] R. Bell. *Introductory Fourier Transform Spectroscopy*, Academic Press, New York, 1972.

[46] National Institutes of Health. *ImageJ: Image Processing and Analysis in Java*. URL: https://imagej.nih.gov/ij/. Accessed 10 May 2017.

[47] D. Barrick and W. Peake. "A Review of Scattering From Surfaces With Different Roughness Scales." *Radio Science*, **8**, 865-868, 1968.

[48] J. Casquilho and P. Cortez. *Introduction to Statistical Physics*, Cambridge University Press, London, 2015.

[49] Y. Mao. *Nearest Neighbor Distances Calculation with ImageJ.* https://icme.hpc.msstate.edu/mediawiki/index.php/. Accessed 29 May 2017.

[50] T. Beniac. "Porous Silicon as an Optical Filter in the Infrared Range." Thesis, Brock University, 2015.

[51] F. Kroeger and C. Swenson. "Absolute Linear Thermal-Expansion Measurements on Copper and Aluminum from 5 to 300 K." *Journal of Applied Physics*, **43**, 835-864, 1977.

[52] C. Choy and K. Cheah. "Laser-Induced Etching of Silicon." *Applied Physics A*, **61**, 45-50, 1995.

[53] J. Burgoyne and M. Cuthbert. "Rising to the Challenges of Constrained Helium Supply in Cryogenic Systems for the Research Market." In W. Nuttall, R. Clarke and B. Glowacki (Ed.). *The Future of Helium as a Natural Resource*, Routledge, New York, 2012.

[54] C. Swenson. "Recommended Values for the Thermal Expansivity of Silicon from 0 to 1000 K." *Journal of Physical and Chemical Reference Data*, **12**, 179-182, 1983.

[55] V. Lehmann. *Electrochemistry of Silicon: Instrumentation, Science, Materials and Applications*, Wiley-VCH, Weinheim, 2002.

[56] W. Sharpe. *Handbook of Experimental Solid Mechanics*, Springer, New York, 2008.